

EUSKAL HERRIKO UNIBERTSITATEA - UNIVERSIDAD DEL PAÍS VASCO
MATERIALEN FISIKA SAILA - DEPARTAMENTO DE FÍSICA DE MATERIALES



Infrared Nanophotonics based on Metal Antennas and Transmission Lines

Martin Schnell

– PhD Thesis –

Thesis supervisor
Rainer Hillenbrand

2012

Contents

| | |
|---|-----------|
| Summary | 1 |
| 1. Introduction to Nano-optics based on Surface Plasmons Polaritons | 5 |
| 1.1. Optical properties of noble metals | 7 |
| 1.2. Surface plasmon polaritons at flat metal surfaces | 10 |
| 1.3. Localized surface plasmons in small metal nanoparticles..... | 14 |
| 1.4. Characteristics of near field and far field regions | 17 |
| 1.5. LSP resonances in metal nanorods | 20 |
| 1.5.1. Numerical methods for calculating the optical response of complex geometries..... | 22 |
| 1.5.2. Optical response of metal nanorods..... | 23 |
| 1.5.3. Nanorods supported by a dielectric substrate..... | 27 |
| 1.5.4. Optical response of coupled metal nanorods | 30 |
| 2. Introduction to Antenna Theory | 33 |
| 2.1. Transmission lines | 34 |
| 2.2. Linear dipole antenna | 38 |
| 2.3. Transfer of antenna theory concepts to optical frequencies | 44 |
| 2.3.1. Scaling law for optical antennas..... | 44 |
| 2.3.2. Antenna loading for tuning optical antennas..... | 46 |
| 2.3.3. Applying impedance matching to optical nanocircuit..... | 48 |
| 3. Transmission-mode s-SNOM..... | 51 |
| 3.1. Introduction | 52 |
| 3.2. Description of the Transmission-mode s-SNOM setup | 56 |
| 3.2.1. Near-field probing and interferometric detection | 56 |
| 3.2.2. Signal detection..... | 59 |
| 3.3. Near-field mapping of metal IR nano-antennas and analysis of the image contrast | 63 |
| 3.3.1. Procedure for the removal of residual background in near-field images | 66 |
| 3.3.2. Near-field mapping of extended 2D antenna structures | 68 |

| | | |
|-----------|---|------------|
| 3.3.3. | Improved s-SNOM mapping with complete suppression of residual background | 71 |
| 3.4. | Conclusions | 72 |
| 4. | <i>Phase-Resolved Mapping of the Near-Field Vector and Polarization State in Nanoscale Antenna Gaps.....</i> | 73 |
| 4.1. | 3D Polarization state of near fields | 74 |
| 4.2. | Polarization- and phase-resolved s-SNOM mapping..... | 77 |
| 4.3. | Reconstruction of the vectorial near-field distribution and polarization state | 80 |
| 4.4. | Conclusions | 85 |
| 5. | <i>Bridging the Gap: Controlling the Near-field Oscillations of Loaded Plasmonic Nanoantennas.....</i> | 87 |
| 5.1. | Introduction | 88 |
| 5.2. | Experimental near-field maps of loaded gap antennas..... | 89 |
| 5.3. | Numerical study of gap antennas with different bridge sizes | 93 |
| 5.4. | Modeling the antenna loading with circuit theory | 96 |
| 5.5. | Conclusions | 99 |
| 6. | <i>Nanofocusing of Mid-Infrared Energy with Tapered Transmission Lines</i> | 101 |
| 6.1. | Introduction | 102 |
| 6.2. | Verification of energy transport in two-wire transmission lines | 104 |
| 6.3. | Numerical study of the surface mode properties | 106 |
| 6.4. | Nanofocusing of mid-infrared energy with tapered two-wire transmission lines. | 108 |
| 6.5. | Conclusions | 112 |
| 7. | <i>List of publications</i> | 113 |
| 8. | <i>Acknowledgements.....</i> | 115 |
| 9. | <i>Bibliography.....</i> | 119 |

Summary

Optical and infrared antennas based on metal nanostructures allow for efficient conversion of propagating light into nanoscale confined and strongly enhanced optical fields, and vice versa. They are therefore highly interesting for the development of compact and integrated nanophotonic devices for telecommunication, near-field microscopy, ultrafast photodetectors and biosensing, which is a highly active research field.

Recently, the transfer of radiofrequency (RF) concepts to optical and infrared antennas has been introduced. This is because optical and infrared antennas share many properties with their larger radiofrequency counterparts. However, there also exist important differences that limit the applicability of RF concepts to optical frequencies. For example, while metals can be well described as a perfect conductor at radiofrequencies, at optical frequencies metals do not behave as a perfect conductor anymore and show particular resonance effects (surface plasmons). Nevertheless, the progress made by current research indicates that RF concepts can be transferred to optical and infrared frequencies. Prominent examples are the scaling law for optical antennas and the introduction of antenna loading with nanocircuit elements for the tuning of optical antennas. Furthermore, the transport of optical and infrared energy on the nanoscale has been demonstrated by adapting RF concepts, for example by miniaturizing RF transmission lines. However, a full understanding of the characteristics of optical antennas and transmission lines as well as their integration in nanoscale optical circuits is still an emerging topic of nanophotonics.

This thesis presents a near-field microscope that allows to verify the merging of radiofrequency and plasmonic concepts at infrared frequencies. This near-field microscope is applied to study infrared antennas and transmission lines for the

nanofocusing of light and the control of near fields on the nanoscale. Thus, both a valuable tool and new design ideas are provided for the development of novel near-field probes and spectroscopic lab-on-a-chip applications for (bio)medical and chemical sensing

After an introduction of basic concepts of nano-optics and antenna theory in chapters 1 and 2, the first infrared transmission-mode scattering-type near-field microscope (s-SNOM) for mapping the near-field distribution of metal nanostructures is introduced in chapter 3. This s-SNOM is based on an atomic force microscope where a sharp tip locally scatters the near fields on a sample surface. By illuminating the sample from below through a transparent substrate (transmission mode), a homogeneous sample illumination is provided. This allows for undistorted near-field mapping with nanoscale resolution of even two-dimensional extended structures such as transmission lines. The power of this s-SNOM lies in the combination of ultra-high spatial resolution on the 10 nm scale, the applicability in the spectral range from visible to THz frequencies and the access to all the three near field components.

Chapter 4 demonstrates the capability of transmission-mode s-SNOM to characterize the polarization state of nanoscale confined light fields on planar antenna structures and nanoscale antenna gaps. This is achieved by a separate acquisition of the amplitude and phase of each near-field component and a subsequent reconstruction of the polarization state, assuming that the tip-scattering tensor is known. Experiments with an inverse bowtie antenna show that the fields inside the antenna gap are confined to an extreme subwavelength-scale spot size of only 50 nm width ($\approx \lambda/200$) and are furthermore linearly polarized.

Chapter 5 provides direct experimental evidence that antenna loading can be applied to infrared antennas, allowing for the control of local infrared fields on the nanometer scale. To this end, the transmission-mode s-SNOM is applied to monitor the near-field response of infrared antennas, which central gap has been progressively loaded with small metal bridges of varying size. By modeling the antenna and the antenna load as impedances, the load-induced changes of the near-field and far-field response of the antennas can be described within the framework of circuit theory.

Chapter 6 predicts and experimentally verifies for the first time that mid-infrared energy can be compressed to deep subwavelength dimensions in tapered two-wire transmission lines, yielding a strongly concentrated infrared spot (nanofocus) at the taper apex. The energy compression is achieved by propagating a mid-infrared surface wave along the transmission-line taper, rather than by locally converting free-space infrared radiation into a nanoscale hot spot, as it is the case with antenna focusing. Nanofocusing with tapered transmission lines thus opens the door to novel near-field probes with an improved signal-to-background ratio and to the development of subwavelength-scale integrated infrared circuits where the energy transport is mediated by surface waves.

1. Introduction to Nano-optics based on Surface Plasmons Polaritons

The interaction of light with matter is the basis for a large number of applications including spectroscopy, optical detectors, lithography and microscopy. These applications are usually realized in form of an optical setup where light is reflected, guided and focused in order to achieve the particular purpose of the application. When classical optical elements such as lenses and mirrors are used, the resolution of the optical setup is limited by diffraction because of the wave nature of light¹⁵. In classical optical microscopy, for example, individual nanostructures cannot be resolved if they are closer than half the wavelength of the illuminating light. Another example is vibrational spectroscopy where the diffraction limit challenges the observation of IR finger prints from a small number of molecules¹⁶. In optical detector applications, the diffraction limit stands for a penalty for power dissipation, area, latency and noise¹⁷. A promising way to overcome these limitations is implementing optics with surface plasmons polaritons¹⁸.

Surface plasmons polaritons (SPPs) are based on the collective oscillations of the free electrons at a metal surface. These oscillations can give rise to strongly enhanced light fields that are spatially confined near the metal surface. The most attractive aspect of SPPs is that they allow for a concentration and a channeling of light on the subwavelength scale¹⁸. By structuring the metal surface on the nanometer scale, the properties of the SPPs can be tailored, offering the potential for the development of new miniaturized photonic circuits¹⁸. A special type of SPPs is found with confined geometries such as metal nanoparticles which support localized SPP resonances. These metal nanoparticles are able to capture propagating light and efficiently convert it into nanoscale confined and strongly enhanced optical fields, and vice versa. When a molecule or a semiconductor is brought into the vicinity of these fields, their interaction

with the free-space light is significantly enhanced. One prominent example is found with surface-enhanced Raman spectroscopy (SERS) where the Raman signal can be enhanced by the order of 10^{14} to 10^{15} , thus enabling the detection of a single molecule^{19,20}. SPP-based nano-optics with metal nanoparticles has also been introduced to highly sensitive spectroscopy^{16,19-21}, ultrafast optical detectors¹⁷, highly efficient solar cells, high-resolution lithography^{22,23} and microscopy applications²⁴⁻²⁸. This chapter will give an overview on the optical response of metal nanoparticles, with a special emphasis being laid on the metal nanorod.

1.1. Optical properties of noble metals

The interaction of metals with electromagnetic radiation is largely governed by the free electrons in the metal¹⁵. The electric field \mathbf{E} of the incident electromagnetic radiation leads to a displacement of the free electrons. On the macroscopic scale, the sum over all free electrons yields a polarization \mathbf{P} of the metal in response to the incident electromagnetic radiation. This optical response of the metal can be described by the dielectric function ε which relates the polarization \mathbf{P} of the metal with the electric field \mathbf{E} according to $\varepsilon = 1 + |\mathbf{P}|/(\varepsilon_0|\mathbf{E}|)$ (ref. ¹⁵). Experimental measurements of the dielectric function of metals have been published in literature^{4,10,29,30}. A simple description of the dielectric function can be found by applying the Drude-Sommerfeld model for the free-electron gas, which assumes that the conduction electrons are allowed to move freely within the bulk of the metal. Applying an oscillating electric field \mathbf{E} of frequency ω , to which the electrons respond with an oscillatory motion, the following expression for the dielectric function ε is found¹⁵ :

$$\varepsilon_{\text{Drude}}(\omega) = \varepsilon_{\text{inf}} - \frac{\omega_p^2}{\omega^2 + i\Gamma\omega}, \quad (1)$$

where ω_p is the plasma frequency and Γ a damping term because of electron-electron and electron-phonon scattering¹⁵. The term ε_{inf} summarizes the effect of the interband transitions¹⁵. In Figure 1a, we plot the Drude-Sommerfeld model (line) and check if it is a good description of the dielectric function of the noble metal gold by comparing it to the literature values from Johnson & Christy⁴ (circle). We insert the following constants for gold taken from ref. ⁷ in eq. (1):

$$\varepsilon_{\text{inf}} = 11, \omega_p = 8.95 \text{ eV and } \Gamma = 65.8 \text{ meV}. \quad (2)$$

Note that we express the frequencies ω_p and Γ in units of energy (eV). We find that eq. (1) is a valid description of the dielectric function of gold for wavelengths $\lambda \geq 600$ nm. We observe that the real part ε' of the dielectric function is always negative. This is a consequence of the fast response of the free electrons to the electric field \mathbf{E} , which allows the electrons to screen the external fields and to prevent a considerable penetration of

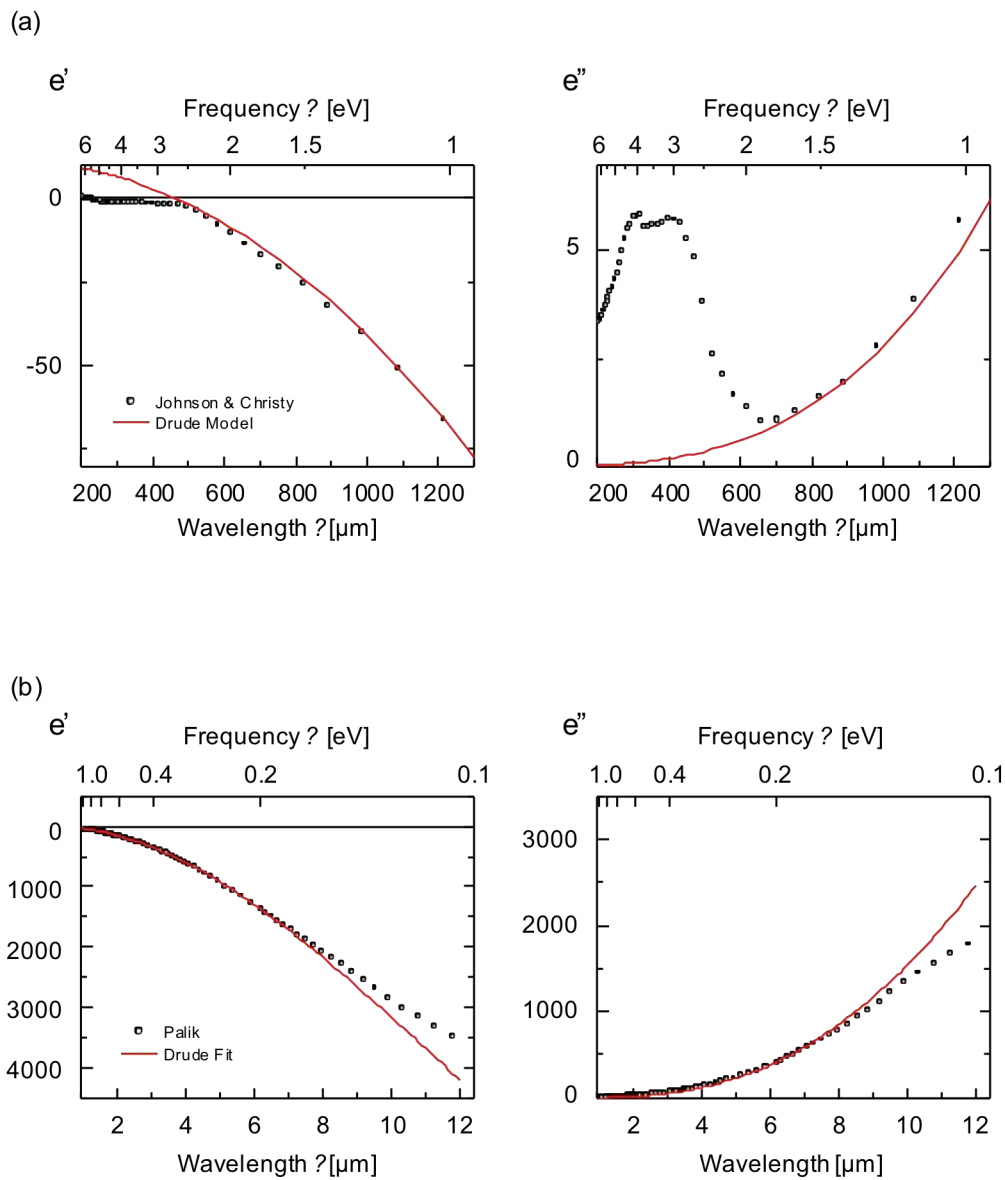


Figure 1: Plot of the dielectric constant $\epsilon = \epsilon' + i\epsilon''$ for the noble metal Gold as a function of wavelength (lower x-axis) and energy (upper x-axis). (a) Drude model (line) and experimental values (circles) from Johnson & Christy⁴ for the visible and near-infrared spectral range. (b) Experimental values from Palik¹⁰ (circles) and Drude model fitted to the experimental values (line), plotted for the mid-infrared spectral range.

1.1 Optical properties of noble metals

light into the metal^{15,31}. Therefore, most noble metals appear opaque and highly reflective at optical frequencies. At shorter wavelengths $\lambda < 600$ nm, the photons exceed the band gap energy of gold and interband transitions take place, leading to absorption losses in the metal. This can be seen with the strong increase of the imaginary part ε'' in the tabulated values (circles). However, the Drude model does not reproduce these absorption effects at short wavelengths because it does not directly take into account the interband transitions.

In order to show the dielectric function of gold in the mid-infrared spectral range, we plot the tabulated data from Palik¹⁰ in the wavelength range from 1 μm to 12 μm in Figure 1b. From the plot (circles) we observe that the real part ε' of the dielectric function reaches very large negative values in the range of several -1000s. This behavior leads to a very strong reflectivity of the metal at infrared wavelengths, reminiscent of a perfect metal. In order to describe the tabulated data from Palik, we fit the Drude model to the experimental data for the wavelength range from 1.5 μm to 7.1 μm , yielding the new values:

$$\varepsilon_{\text{inf}} = 11, \omega_p = 7.77 \text{ eV and } \Gamma = 60.2 \text{ meV (for mid-IR),} \quad (3)$$

where ε_{inf} was held constant during the fitting. From the plot we see that the optical properties of gold in the mid-infrared range are in principle well described by the Drude model over a wide frequency range. Only for wavelengths longer than 7.1 μm is the experimental data not very well reproduced by the Drude model. This is related to a decreasing slope at these wavelengths, not observed with other experimental data (e.g. Ordal et al.²⁹).

1.2. Surface plasmon polaritons at flat metal surfaces

Surface plasmon polaritons (SPPs) are electromagnetic surface modes at the interface between a dielectric and a metal^{15,18,32}. They are based on the excitation of collective oscillations of the free electrons in the metal. The electromagnetic field of the SPPs decays exponentially from the interface, which makes the SPPs to be a bound mode propagating along the interface (Figure 2a)³². The dispersion of SPPs can be found by solving Maxwell equations assuming surface waves and the appropriate boundary conditions.

For a planar interface between a dielectric ϵ_d with $\epsilon'_d > 0$ and a metal ϵ_m with $\epsilon'_m < 0$, the dispersion relation is given by^{7,31}

$$k_x(\omega) = k_0 \sqrt{\frac{\epsilon_m \epsilon_d}{\epsilon_m + \epsilon_d}}, \quad (4)$$

where the wave vector k_x in propagation direction (here arbitrarily assumed to be the x-axis) is expressed as a function of the dielectric constant of the metal and the dielectric, and $k_0 = 2\pi/c$ is the light wave vector in vacuum. To illustrate the SPP dispersion relation, we assume a dielectric medium of $\epsilon_d = 1$ and apply the Drude model from eq. (1) with the values from eq. (2) to describe the dielectric value ϵ_m of gold. The result is shown in Figure 2b. For the frequency range of visible light ($\omega > 2$ eV), we find that the real part of the SPP wave vector k'_x (red line) is significantly larger than the light line $k_0(\omega)$ (black line). The reason of this observation is the strong coupling between the light and the surface charges^{15,18}. The bending of the dispersion relation to the right shows that this coupling becomes increasingly stronger towards the surface plasmon resonance frequency $\omega_{\text{SP}} \approx 2.58$ eV (dashed line) where $\epsilon'_m = -1$. A different behavior is observed for the frequency range of infrared light (0.05 eV $< \omega < 1$ eV). Here, the SPP wave vector is only marginally larger than the light line k_0 . This means that at visible frequencies the SPP wavelength $\lambda_{\text{SPP}} = 2\pi/k'_x$ is significantly shorter than the

1.2 Surface plasmon polaritons at flat metal surfaces

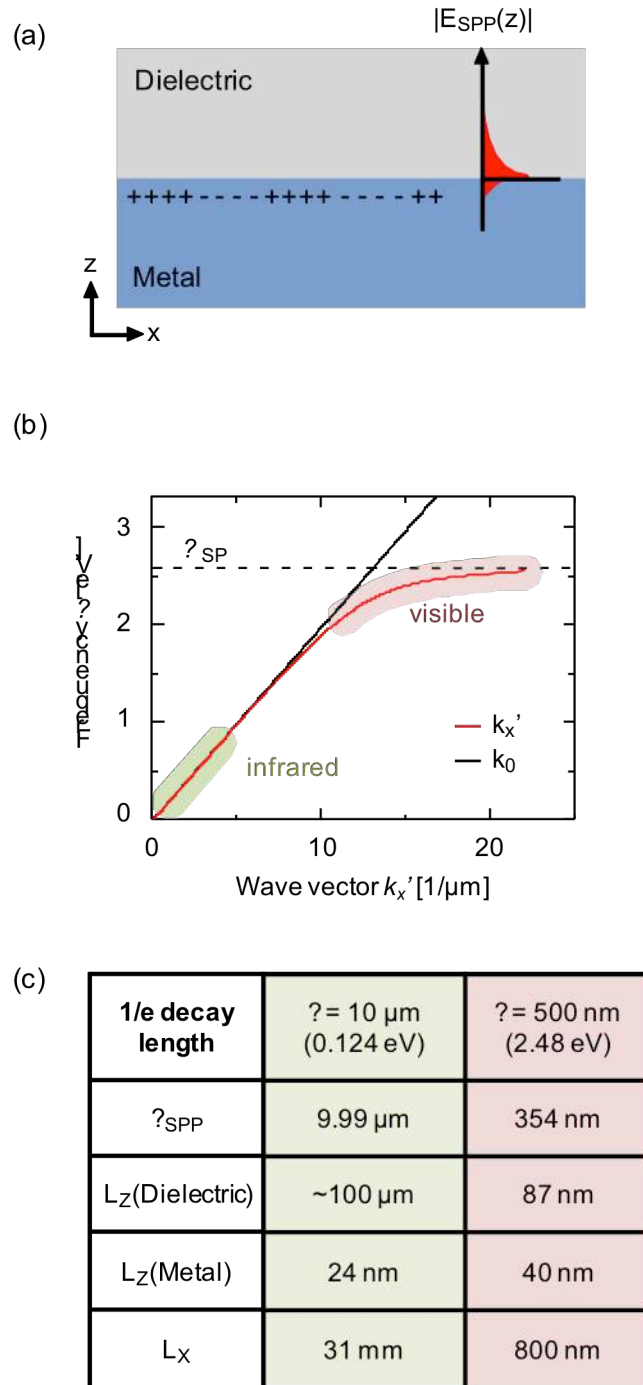


Figure 2: (a) SPP propagating in x-direction along a flat interface between a dielectric ($\epsilon'_d > 0$) and metal ($\epsilon'_m < 0$). (b) Dispersion curve of a gold-air interface, showing the real part k'_x (red line) of the SPP wave vector as a function of frequency ω . The black line is the light line in vacuum k_0 . (c) The plasmon wavelength $\lambda_{\text{SPP}} = 2\pi/k'_x$, decay length of the SPP electric field $|E_{\text{SPP}}(z)|$ in z-direction into the dielectric and the metal for the two selected wavelength of 10 μm and 500 nm, representing the infrared and visible spectral range, respectively.

free-space wavelength λ while at infrared frequencies it is approximately of the same value as the free space wavelength λ (see table in Figure 2c).

The field confinement perpendicular to the surface can be obtained by considering the wave vector component in z-direction in each medium, which for a SPP at a flat interface is given by ¹⁵

$$\begin{aligned}
 k_{z,d}(\omega) &= k_0 \sqrt{\frac{\epsilon_d^2}{\epsilon_m + \epsilon_d}} \text{ in the dielectric ,} \\
 k_{z,m}(\omega) &= k_0 \sqrt{\frac{\epsilon_m^2}{\epsilon_m + \epsilon_d}} \text{ in the metal.}
 \end{aligned}
 \tag{5}$$

The field confinement is given as the $1/e$ decay length of the SPP electric field in z-direction and can be obtained by evaluating $L_z = 1/k_z''$. As shown in Figure 2c, at visible frequencies the decay length L_z into the dielectric is much shorter than the free-space wavelength λ . Thus, at visible wavelength we can employ SPPs for confining fields to the surface. This finds applications in magneto-optic data storage, chemical sensing and spectroscopy^{33,34}, biomedical application and miniaturized photonic circuits^{18,35}. In contrast, at infrared and THz frequencies the decay is very long and can amount to several free-space wavelengths³⁶. The confinement of the electric fields at flat metal surfaces is very weak, which makes these modes unattractive for the use in above named applications. The confinement can be greatly improved by patterning the metal surfaces with the aim of mimicking the properties of SPPs at infrared and THz frequencies (spoof-SPPs)³⁷.

The SPP field also penetrates the metal for a few 10s of nanometers for both visible and infrared spectral regions (Figure 2c). Because the metal is lossy, energy of the SPP wave is dissipated in the metal. This leads to a damping of the SPP wave in propagation direction, which is described by the propagation length L_x . The propagation length $L_x = 1/k_x''$ is defined as the length scale over which the field amplitude of the SPP has decayed to $1/e$. Here, an important difference can be recognized between visible and infrared wavelengths. Because of the strong damping of the coherent oscillations at visible wavelengths, the SPP propagation length L_x is limited to the order of the micrometer^{38,39}. In contrast, at infrared wavelengths the damping is weaker, resulting in a

much larger propagation length in the millimeter range³⁸. This indicates that the surface wave propagates over long distances, however, the confinement is poor with the SPP field extending several wavelengths into the dielectric. As we show in chapter 6, a much stronger confinement can be obtained with transmission lines consisting of two closely spaced metal wires. While the confinement is improved by more than 3 orders of magnitude, this comes along with a significantly reduced propagation length.

The excitation of SPPs on a metal-air interface requires the conservation of energy and momentum. Since the SPP wave vector k'_x is larger than the light line k_0 , a direct excitation of SPPs with light is not possible. The wave-vector mismatch can be overcome by using the increased wave vector nk_0 in an additional dielectric medium ($n > 1$). This approach is realized in the Otto configuration or the Kretschmann-Raether geometry¹⁵.

1.3. Localized surface plasmons in small metal nanoparticles

When a metal nanoparticle is illuminated externally with light, the electric field of the light can drive the conduction electrons to coherent oscillations (Figure 3). At certain frequencies, the conduction electrons oscillate resonantly with the incident light. This effect is termed localized surface plasmon (LSP) resonances and gives rise to a variety of interesting effects. One of the most important effects of LSP resonances is the conversion of the energy carried by the incident light into subwavelength-scale localized fields. These fields are strongly enhanced in comparison to the incident light and also strongly confined to the surface of the metal nanoparticle. Therefore, the LSP resonances provide a subwavelength focusing of light without being limited by the diffraction limit inherent to classic optical elements. A second aspect of LSP resonances is the conversion of energy from localized fields into propagating waves. This can be achieved when the LSP resonances couple to the electromagnetic fields emitted by molecules, atoms or quantum dots placed close to the nanoparticle. In this way, the emission of these objects can be significantly enhanced with the nanoparticle and even directed by special geometries⁴⁰.

When light illuminates a metal nanoparticle, the electric field of the incident field induces a displacement of the electron cloud relative to the nuclei (Figure 3a), yielding a polarization of the nanoparticle. For very small nanoparticles that can be treated in the quasi-static limit, the polarizability α_P of the particle is given by

$$\alpha_P(\omega) = 4\pi R^3 \frac{\epsilon_m(\omega) - \epsilon_d}{\epsilon_m(\omega) + 2\epsilon_d} \quad (6)$$

where R is the radius of the metal nanoparticle with $R \ll \lambda$, $\epsilon_m(\omega)$ is the frequency-dependent dielectric function of the metal and ϵ_d is the dielectric constant of the surrounding medium³⁹. The occurrence of LSP resonances can be recognized in the polarizability α_P , which diverges when the following condition is met:

1.3 Localized surface plasmons in small metal nanoparticles

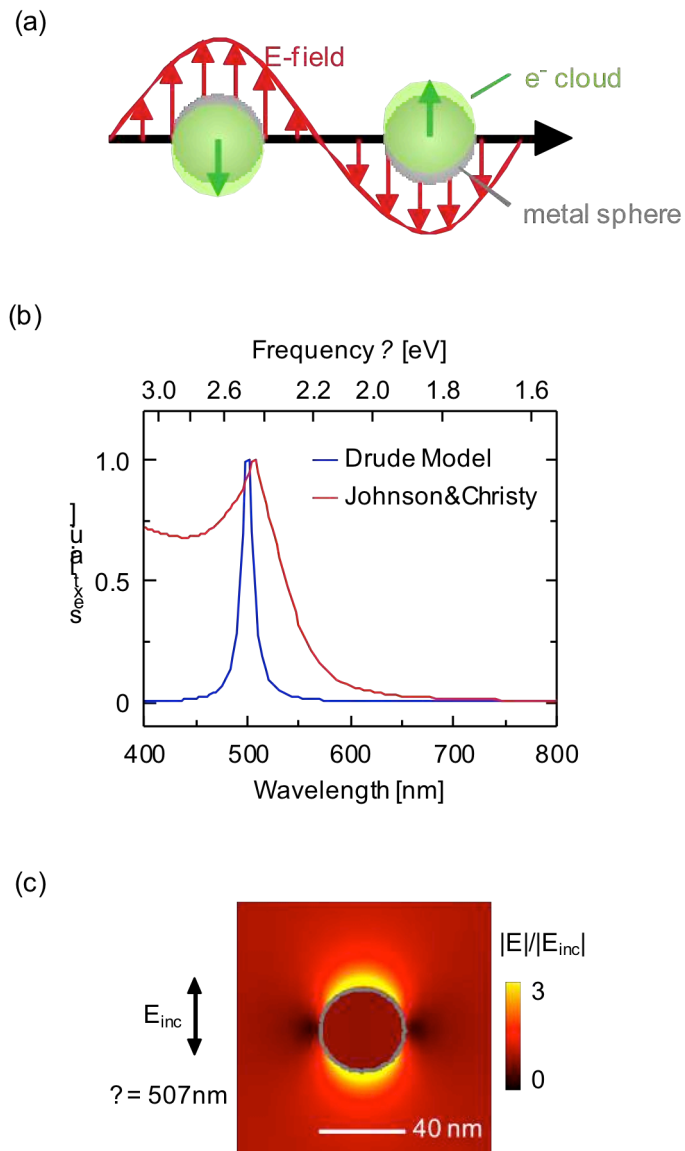


Figure 3: (a) Schematic of plasmon oscillation for a sphere, showing the displacement of the conduction electron charge cloud relative to the nuclei [after Kelly et al. ³]. (b) Extinction cross section for a 20 nm radius gold sphere in vacuum, calculated with eq. (8) using the Drude Model with the literature values from eq. (2) (blue curve) and the tabulated data from Johnson & Christy (c) Numerically calculated field profile of the nanoparticle considered in (b) at the wavelength of $\lambda = 507 \text{ nm}$. Note: saturated color scale.

$$\varepsilon_m(\omega) = -2\varepsilon_d, \quad (7)$$

which is satisfied for a specific frequency ω of the incident light. Note that in contrast to SPPs on flat metal surface, the momentum conservation is provided by the finite geometry of the nanoparticle.

The excitation of the LSP resonance in a metal particle removes energy from the incident light in form of absorption (dissipation inside the particle) and scattering of light. The extinction cross section is defined as the sum of absorbed and scattered energy, divided by the power density of the incident light. In case of very small spherical nanoparticle, it can be shown that the extinction cross section is proportional to the imaginary part of the polarizability α_p ³¹

$$\sigma_{\text{ext}} = \sqrt{\varepsilon_d} k_0 \text{Im}(\alpha_p), \quad (8)$$

where ε_d is the dielectric value of the surrounding medium and k_0 the wave vector of the incident light. To illustrate eq. (8), we plot the extinction cross section σ_{ext} for a 20 nm radius gold nanoparticle in vacuum ($\varepsilon_d = 1$) in Figure 3b using the Drude model from eq. (1) and the tabulated values from Johnson & Christy⁴ to describe the dielectric constant of gold. We observe a sharp peak in the extinction cross section which can be attributed to the LSP resonance. Because of the deviation of the Drude model from the tabulated data for wavelengths smaller than 550 nm (see Figure 1), the blue line is not a good description of the LSP resonance which are typically observed in experiments, yielding a peak that is blue shifted, too narrow and too high³¹. In contrast, when using the tabulated data from Johnson & Christy (red line), the correct peak can be obtained³¹, that is observed at a wavelength of $\lambda_{\text{sph}} = 507$ nm.

To identify the nature of the LSP resonance, in Figure 3c we show the local field amplitude of the nanoparticle calculated in a plane perpendicular to the incident wave using a commercial FDTD package (see chapter 1.5.1). This field plot shows that the electric field amplitude near the surface of the nanoparticle is enhanced by about a factor of 5 in comparison to the incident field and confined to surface to about 10 nm.

1.4. Characteristics of near field and far field regions

The scattered fields of metal nanoparticles are commonly separated into two regions: the near-field and the far-field region. In the following, they will be defined with the example of an oscillating electric dipole, whose fields can be described analytically⁴¹. The analytical solution of the electric field E of an oscillating electric point dipole is given by

$$E = \frac{1}{4\pi\epsilon_0} \left\{ k^2 (\mathbf{n} \times \mathbf{p}) \times \mathbf{n} \frac{e^{ikr}}{r} + [3\mathbf{n}(\mathbf{n} \cdot \mathbf{p}) - \mathbf{p}] \left(\frac{1}{r^3} - \frac{ik}{r^2} \right) e^{ikr} \right\} e^{-i\omega t}, \quad (9)$$

where k is the wave vector, ω the frequency of the oscillation, r is the position vector with $r = |\mathbf{r}|$ and $\mathbf{n} = \mathbf{r}/r$ and \mathbf{p} the dipole moment⁴¹. This solution takes simple forms in the limit of being either very close or very far from the point dipole. In the far-field region ($r \gg \lambda$), the electric field takes on the limiting form

$$E = \frac{1}{4\pi\epsilon_0} k^2 (\mathbf{n} \times \mathbf{p}) \times \mathbf{n} \frac{e^{ikr}}{r} e^{-i\omega t} = Z_0 \mathbf{H} \times \mathbf{n}, \quad (10)$$

where $Z_0 = \sqrt{\mu/\epsilon}$ is the wave impedance of free space. This equation describes spherical waves where the electric field E and the magnetic field H are perpendicular to each other. These waves are propagating waves because of the term $e^{ikr-i\omega t}$.

In the near-field region ($r \ll \lambda$), the fields of an oscillating electric dipole can be approximated by⁴¹

$$E = \frac{1}{4\pi\epsilon_0} [3\mathbf{n}(\mathbf{n} \cdot \mathbf{p}) - \mathbf{p}] \frac{1}{r^3} e^{-i\omega t}. \quad (11)$$

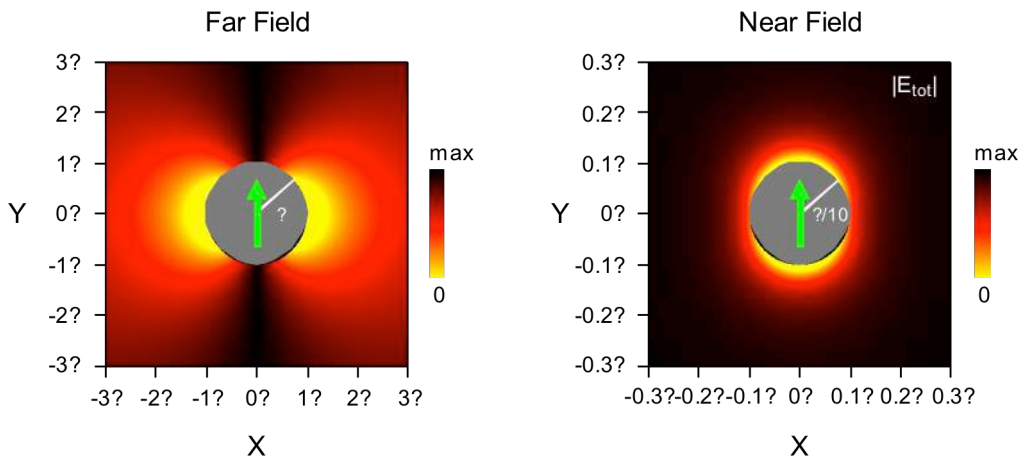


Figure 4: Electric field amplitude of an electric dipole. The left panel shows the far-field approximation ($r \gg \lambda$), the right panel shows the near-field approximation ($r \ll \lambda$). The green arrow indicates the orientation of the dipole. Please note the different scales XY in both panels. The grey disc of given radius masks the fields around the electric dipole which would saturate with the used color scale.

This equation describes quasi-static, strongly decaying fields – also called near fields. These fields are quasistatic in space because the fields only oscillate in time with $e^{-i\omega t}$. They decay with a rate of $1/r^3$ and do not transport energy from the dipole.

Figure 4 shows the electric field distribution for the far-field and the near-field region for an electric dipole aligned in y-direction as indicated by the green arrow. The difference in the field distribution and the different field decay can be observed. Note that the electric field distribution in the near-field zone is identical to the near-field mode of a very small metal nanoparticle at the LSP resonance, which was shown in Figure 3c, if the incident field is taken into account.

Far fields are propagating waves in the sense of Maxwell's equations and thus can propagate forever, e.g. even in the case that the source is switched off. Likewise, extracting power from the radiated fields has no effect on the source. This is a fundamental property of radiating fields and is in contrast to the near fields. The latter are reactive fields or storage fields, meaning that they store the energy that drives the dipole oscillation in e.g. nanoparticles or antennas. Therefore, the near fields extinguishes when the source is turned off. Likewise, the source is sensitive to any object

1.4 Characteristics of near field and far field regions

| | Near (reactive) field | Far (radiated) field |
|------------------|---|---|
| Carrier of Force | Virtual Photon | Photon |
| Energy | Stores energy: Can transfer energy via inductive or capacitive coupling. | Propagates (radiates) energy |
| Longevity | Extinguishes when source power is turned off. | Propagates until absorbed |
| Interaction | Act of measuring fields or receiving power from field causes changes in voltage/currents of source circuit. | Act of measuring field or receiving power from field has no effect on source |
| Shape of Field | Completely dependent on source circuit. | Spherical waves. At very long distances, field takes shape of plane waves |
| Wave impedance | Depends on source circuit and medium. | Depends solely on propagation medium ($\eta = 120\pi = 377\Omega$ in free space) |
| Guiding | Energy can be transported and guided using a <u>transmission line</u> . | Energy can be transported and guided using a <u>wave guide</u> . |

Table 1: The characteristics of near fields and far fields summarized, taken from a textbook for radiofrequency antenna theory, taken from ref. ⁸.

that is placed in its near field, e.g. any absorption of the near-field energy will affect the source. For this reason, the measurement of near fields is difficult because the near-field probe potentially interacts with the object via the near field and thus potentially disturbs the measurement. Table 1 summarizes the general properties of near fields and far fields.

1.5. LSP resonances in metal nanorods

In comparison to spherical nanoparticles, elongated nanoparticles offer an additional degree of freedom for the tailoring of the optical properties in metallic structures^{31,42,43}. Because of their anisotropic shape, elongated nanoparticles support LSP resonances at different frequencies that correspond to the charge oscillations along the different symmetry axis^{44,45}. A particular interesting shape is the metal nanorod that exhibits a strong longitudinal LSP resonance that can be excited with incident light polarized along the nanorod long-axis. By simply changing its length, this longitudinal plasmon resonance can be tuned over a wide frequency range from visible to mid-IR frequencies^{2,6,7,43,46-48}. Metal nanorods also exhibit a transverse LSP resonance that can be excited with the incident light being polarized perpendicular to the long axis. This resonance is determined by the diameter of the nanorod and can be expected to be independent of the nanorod length^{6,49}, and thus its tuning is limited.

In a simple picture, the longitudinal plasmon resonances in metal nanorods can be interpreted as standing plasmon polariton waves^{50,51} or Fabry-Pérot resonances⁵². They can be easily found by

$$L = i \cdot (\lambda_{\text{eff}}/2) \quad (12)$$

where L is the nanorod length, i the order of the resonance and λ_{eff} the effective wavelength of the plasmon mode on the nanorod. To obtain an intuitive understanding of the optical response, we show the surface charge distributions of the standing wave modes for an isolated gold nanorod in the electrostatic limit⁶. These are found by formulating the boundary conditions for a system of a gold nanorod in vacuum with the material inside and outside being homogeneous

$$\Lambda_i \sigma_i(s) = - \int_S ds' \frac{n_s \cdot (s-s')}{|s-s'|^3} \sigma_i(s'), \quad (13)$$

where $\sigma_i(s')$ is the surface-charge density, s and s' are space vectors for points on the surface S of the rod, the integral is a surface integral over points s' on S , and n_s is the normal vector to the surface at points s . By solving the eigenvalue problem, a series of

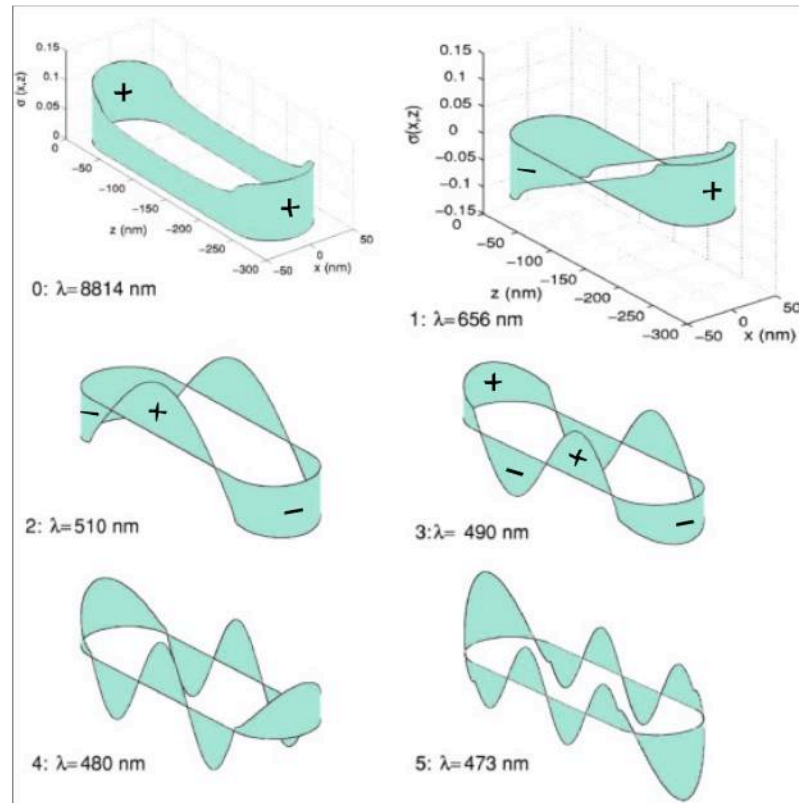


Figure 5: Eigenmodes of a gold nanorod (200 nm long, 40 nm radius) in the electrostatic limit. Shown is a cross section of the surface-charges density of the eigenmodes $i = 0..5$ together with the corresponding energy, expressed here in terms of wavelength. Taken from ref. ⁶.

eigenvalues Λ_i and the corresponding surface-charge density $\sigma_i(s')$ are obtained (Figure 5). The zero-order mode $i = 0$ is unphysical because it means that the nanorod carries a non-zero charge. The first-order mode $i = 1$ is the first physical meaningful mode and describes the fundamental dipolar mode. The third and higher-order odd modes $i = 3,5,7 \dots$ have a net-dipolar moment along the long axis and can therefore be excited by external plane-wave illumination. In contrast, the even-order modes $i = 2,4,6, \dots$ show symmetric charge distributions without a net dipole mode. Therefore, these modes cannot be excited with plane waves under normal incidence, although an excitation is possible under inclined incidence because of retardation effects⁵⁰.

1.5.1. Numerical methods for calculating the optical response of complex geometries

The optical response of metal nanorods can be calculated using numerical methods such as the Boundary Element Method (BEM)¹³ or the Finite-difference time-domain (FDTD)⁵³ technique. These numerical techniques are necessary because analytical solutions to Maxwell's equation can only be found for special geometries such as spheres or spheroids. In this thesis – if not stated otherwise – a commercial FDTD package from Lumerical (www.lumerical.com) was employed. The FDTD method solves Maxwell's equation in complex, three-dimensional geometries. Because this technique is discrete in both space and time, the electromagnetic fields and structural materials are described on a discrete mesh which is made up of Yee cells. The FDTD method yields the exact solution of Maxwell's equations when the size of the mesh cells goes to zero. To simulate the interaction of light with materials, light sources inject electromagnetic fields into the simulation regions, where the fields interact with the material in form of e.g. scattering or absorption. After the interaction, the remaining energy of the injected fields is absorbed by the walls of the simulation volume which consist of a special material called perfectly matched layer (PML). The FDTD method is a time domain technique which means that the electromagnetic fields are solved as a function of time. In order to calculate the electromagnetic fields as a function of frequency, Fourier transforms are performed during the simulation, allowing for the extraction of local field maps but also for the calculation of the Poynting vector, normalized transmission and far field projection, all as a function of frequency.

The near-field response of a metal nanorod can be directly extracted from the simulation by placing a field monitor in the simulation volume. Because the FDTD sources usually inject a broadband pulse into the simulation volume, the near fields can be recorded over a certain spectral range. The extraction of the far-field extinction can be accomplished by using a total-field-scattered-field source which is an advanced version of a plane wave source. In contrast to the latter, it is a 3D box where the fields are injected at one side of the box and removed (subtracted) at the opposite side. By this way, the simulation volume is divided in two regions, where the inner region contains the sum of the incident

plus the scattered fields whereas the outer region contains only the scattered field. The far-field extinction is obtained by placing two 3D monitor boxes in the simulation volume, where one monitor box is located in the inner volume and the other box is located outside the source. By calculating the transmitted power through each box, the absorption (inner box) and scattering (outer box) from the object is obtained, respectively. The far-field extinction is calculated as the sum of both.

1.5.2. Optical response of metal nanorods

Optical resonances of noble metal nanorods have been observed in the far field experimentally and numerically^{6,9,43,45,50,54,55}. In these studies, the nanorod length typically measured a few hundreds of nanometers which resulted in a far-field resonance at wavelengths in the visible and near-infrared spectral region. A resonance at mid-IR frequencies can be achieved if the nanorod length is increased to a few micrometers. Crozier et al.² observed with far-field spectroscopy that 1.5 μm long gold nanorods on a Si substrate showed a resonance at around 10 μm wavelength. Similar experimental studies with metal nanowires of lengths between 1 μm to 5 μm also showed resonances in the mid-infrared spectral range^{47,48}. By coupling a small electrical detector such as microbolometers, thermocouples or nonlinear junctions to the metal nanorods, the infrared response of metal nanowires has been measured⁵⁶⁻⁵⁹. Therein, the electric current through the detector allowed for determining the radiation reception of the nanorod as a function of its length and the nanorod radiation pattern.

Metal nanorods also have the capability to generate highly enhanced and localized near fields^{6,7,31,45,60}, like the spherical metal nanoparticles discussed in chapter 1.3. This local field enhancement is produced by the LSP resonance in the metal nanorod and is typically highest at the nanorod ends. Typical values of the electric field amplitude enhancement in comparison the incident field range between 70 and 100 for nanorods with resonances in the visible/near-infrared range^{6,31,60}. For mid-infrared resonant nanorods, numerically studies showed that also micrometer-long metal nanorods have the capability to generate near fields that are strongly enhanced and moreover highly

confined to only 10 to 20 nm². In comparison to the short nanorods, similar values for the field enhancement have been observed for these long nanorods^{2,16}.

In the following, we perform a numerical study with metal nanorods of different lengths in order to compare their response in the visible/near-infrared and in the infrared spectral range. To this end, we assume cylindrical Au nanorods situated in vacuum and illuminated with a plane wave that is polarized along the long axis of the nanorod. The nanorod is of a fixed diameter of 80 nm, a typical value found in experiments. The ends of the nanorods are covered by half spheres of the same diameter as the rod. Here, the rod length L is defined as the distance from both end points including the half spheres. The rod length is varied from 100 nm to 400 nm and from 1.0 μm to 3.0 μm . By monitoring the far-field extinction and the near-field enhancement of the metal nanorods, a comparison between the two spectral regions is obtained. For the visible/near-infrared spectral range, the Drude model from eq. (1) with the literature values from eq. (2) is used. For the mid-infrared spectral range, the Drude fit to the dielectric data from Palik from eq. (3) was used.

Figure 6a shows the far-field extinction spectra for metal nanorods of lengths L from 100 nm to 400 nm, which all show a single peak in the visible/near-infrared spectral range between 0.5 μm and 1.5 μm wavelengths. This peak can be assigned to the fundamental dipolar resonance consistent with the mode charge distribution shown in Figure 5 for the case $i = 1$ (ref. ⁶). For the smallest length $L = 100$ nm, this resonance occurs close to the resonance of a spherical metal nanoparticle located at $\lambda_{\text{sph}} = 507$ nm (compare with Figure 3). For increasing length L , the fundamental dipolar resonance shifts monotonously to longer wavelengths together with an growing extinction because of an increasing polarization along the nanorod⁶. Figure 6c shows the far-field extinction spectra for nanorods of lengths L from 1.0 μm to 3.0 μm , showing a single peak in the mid-infrared spectral range between 2 μm to 12 μm wavelength. As with the shorter nanorods, this peak can be assigned to the fundamental dipolar resonance with a charge distribution shown in Figure 5 for $i = 1$. In case of the longest rod $L = 3$ μm (blue line), a second peak is observed at 2.50 μm wavelength. This peak can be assigned to a higher-order mode consistent with a mode charge distribution shown in Figure 5 for $i = 3$ (ref. ⁶). The peak of this mode is less intense than the peak of the fundamental mode,

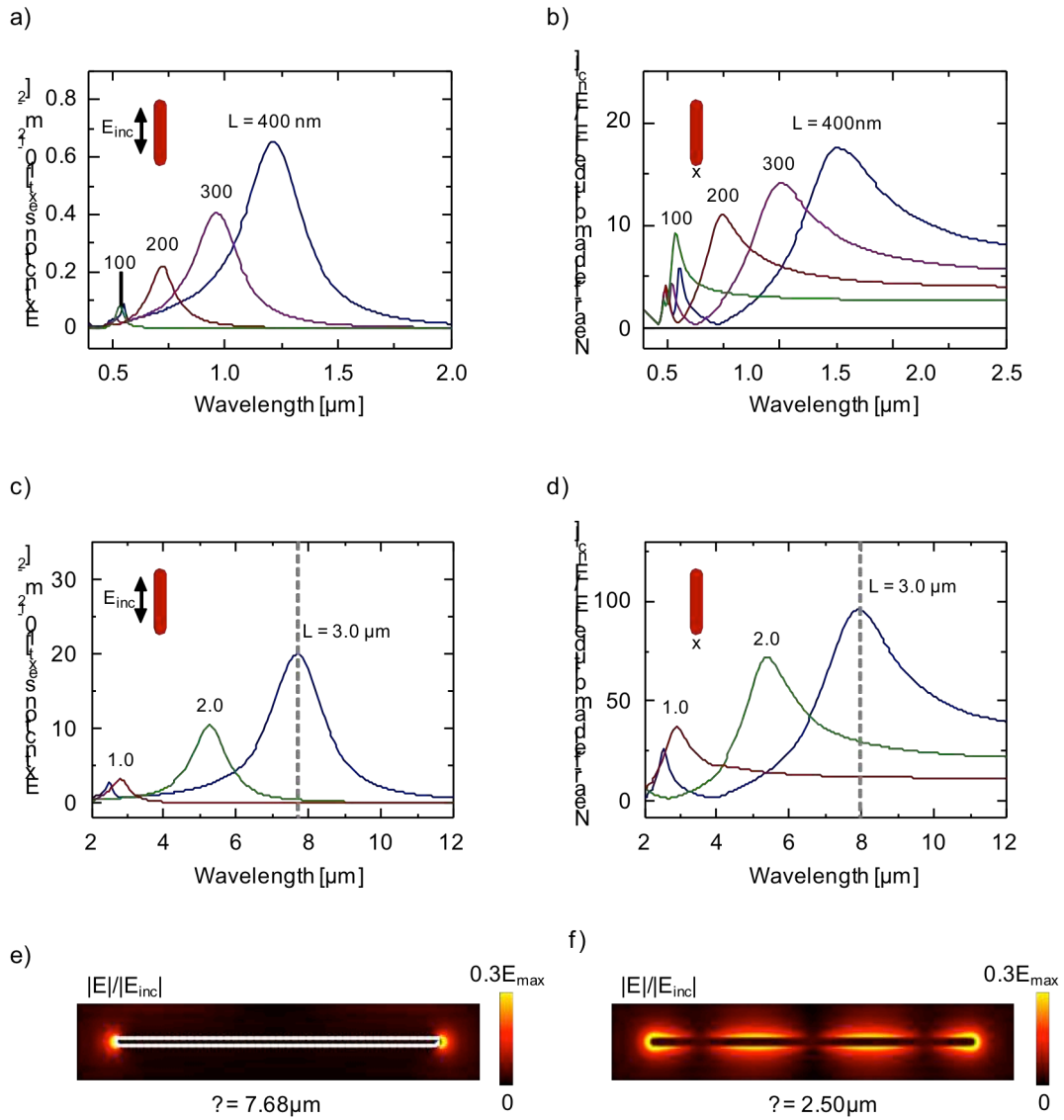


Figure 6: Numerically calculated far-field extinction and near-field amplitude spectra of cylindrical gold nanorods of different lengths L . A plane wave illumination perpendicular to the nanorod long axis is assumed with the polarization being parallel to the long axis. **(a)** Far-field extinction spectra for nanorods resonant at visible/near-infrared wavelengths. **(b)** Near-field amplitude evaluated at a distance of 5 nm from the nanorod cap for the nanorods in (a). **(c)** Far-field extinction spectra for nanorods resonant at mid-infrared wavelengths. **(d)** Near-field amplitude evaluated at a distance of 5 nm from the nanorod cap for the nanorods in (d). The mesh size is 1nm in case of (a),(b) and 2.5nm in case of (c),(d). **(e),(f)** Numerically calculated field profile of the nanorod of length $L = 3 \text{ } \mu\text{m}$ at the far-field extinction peaks occurring at $\lambda = 7.68 \text{ } \mu\text{m}$ and $\lambda = 2.50 \text{ } \mu\text{m}$ in (c). Note: saturated color scales.

indicating that the higher-order mode has a smaller dipole moment than the fundamental mode.

Figure 6b and Figure 6d show the near-field spectra for the short and long nanorods. The near-field amplitude is calculated at a distance of 5 nm from the right end of the nanorod and are normalized to the incident field E_{inc} . The shape of the near-field spectrum is similar to the far-field extinction spectra, with the fundamental dipolar mode and higher-order modes being clearly recognizable. An important difference to the far-field extinction spectra is found for wavelengths larger than the fundamental dipolar resonance. Here, the near-field spectrum still shows significant amplitude values while the far-field extinction quickly falls to zero. For example, in the case of the rod $L = 3 \mu\text{m}$, the maximum near field enhancement amounts to $|E|/|E_{\text{inc}}| = 95$ at its fundamental dipolar resonance near $7.93 \mu\text{m}$ wavelengths. At the longest calculated wavelength of $12 \mu\text{m}$, the near-field enhancement still amounts to $|E|/|E_{\text{inc}}| = 39$. This phenomena is called the lightning rod effect and describes a local field enhancement near a highly curved surface in the absence of any resonances⁶¹. In Figure 6b and Figure 6d, it is equally observed with nanorods with resonances in the visible/near-infrared and mid-infrared range. The lightning rod effect is relevant for chapter 5 where infrared antennas are mapped at wavelengths far longer than their resonance wavelength, but still a considerable near-field signal is observed in experiments and calculations.

A further difference between far-field and near-field spectra is a slight shift of the maximum of the fundamental dipolar mode. In case of the metal nanorod of length $L = 3 \mu\text{m}$, the near-field maximum occurs at $\lambda_{\text{nf}}^{\text{max}} = 7.93 \mu\text{m}$ wavelength (see grey dashed line in Figure 6d) and is slightly red-shifted to the far-field extinction maximum which occurs at $\lambda_{\text{ff}}^{\text{max}} = 7.68 \mu\text{m}$ wavelength. The shift between the near-field and far-field spectra is a fundamental property of LSP-resonant metal nanoparticles. It is related to the material intrinsic plasmon damping and to radiation losses⁶²⁻⁶⁴.

To support the claim that the peaks in the far-field extinction in Figure 6c correspond to the fundamental dipolar resonance, we calculate exemplarily for the longest nanorod $L = 3 \mu\text{m}$ the local fields at the extinction peak at $\lambda_{\text{ff}}^{\text{max}} = 7.68 \mu\text{m}$. In Figure 6e, we plot the fields in a cross section along the long axis of the nanorod. We observe two regions of strong field confinement at the rod ends and decaying fields towards the rod center.

This shape is in agreement with the eigenmode $i = 1$ calculated in the electrostatic limit in Figure 5, which shows that this mode is indeed the fundamental dipolar mode. In Figure 6f, we also calculate and plot the fields at the second extinction peak of the longest nanorod $L = 3 \mu\text{m}$ occurring at $\lambda_{\text{ff}}^{\text{max}} = 2.50 \mu\text{m}$. Here, we observe four regions of field enhancements, which allows us to assign this mode to the eigenmode $i = 3$ in Figure 5. The second extinction peak is thus generated by the third-order dipolar mode of the nanorod.

1.5.3. Nanorods supported by a dielectric substrate

The LSP resonances in metal nanoparticles are dependent not only on the shape of the nanoparticle, but also on the dielectric surrounding^{65,66}. For small metal particles treated in the electrostatic limit⁶⁷, this dependence can be recognized in the LSP resonance condition $\varepsilon_m = -2\varepsilon_d$ given in eq. (7), where ε_m is the dielectric function of the metal and ε_d is the dielectric value of the surrounding medium. In practice, nanoparticles are usually placed on top of a dielectric substrate. In this case, the surrounding medium is inhomogeneous. The surface charges of the nanoparticle induce image charges in the substrate. The induced image charges interact with the LSP mode and cause a red-shift or a blue-shift of the nanoparticle plasmon mode^{65,68}. The strength of the image charges is reduced by the screening factor $(\varepsilon_d - 1)/(\varepsilon_d + 1)$ (refs. ^{15,65,68}), which lets the frequency shift of the plasmon mode be dependent on the dielectric constant of the substrate ε_d .

To illustrate the red-shift of the nanorod resonance due to the presence of a dielectric substrate, we calculate numerically the far-field extinction spectrum of a $1 \mu\text{m}$ long nanorod situated on top of a flat Si substrate (Figure 7a). Here, we assume a rectangular cross section for the nanorod (40 nm height x 125 nm width) rather than a round cross section, which is a better description of lithography fabricated nanorods. The far-field extinction spectrum is plotted in Figure 7b (red line) and we find that the fundamental resonance occurs at a wavelength of $\lambda_{\text{Si}} = 7.12 \mu\text{m}$. For comparison, we also show the spectrum of the same rod situated in vacuum (black line), revealing a resonance at a

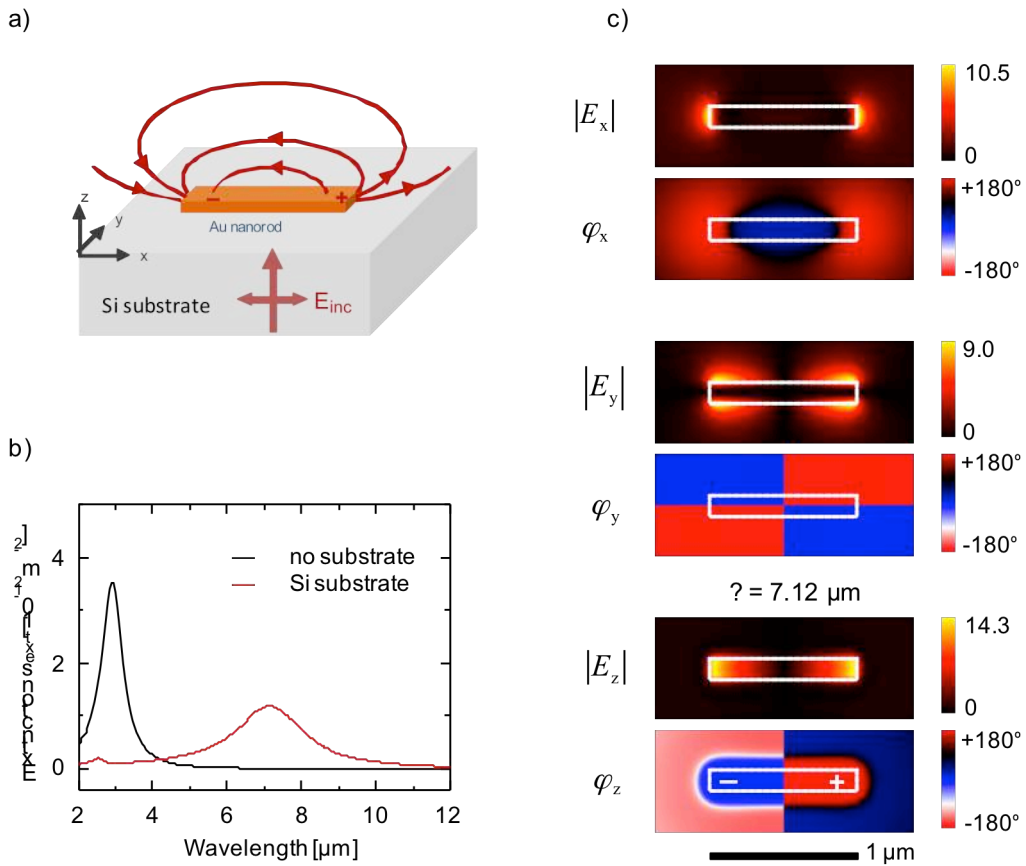


Figure 7: (a) Scheme of a metal nanorod situated on top of a dielectric substrate. The gold nanorod (1000 nm x 125 nm x 40 nm) is illuminated by a plane wave from below through the substrate. (b) Far-field extinction spectrum (c) Electric field amplitude E_i and phase φ_i of the three components $i = x, y, z$ in a plane 30 nm above the surface of the nanorod in (a), evaluated at a wavelength of 7.12 μm and expressed relatively to the incident field E_{inc} . The near-field phase has been shifted for all three components by the same value found by setting φ_z at the left rod end to zero.

wavelength of $\lambda_{vac} = 2.90 \mu\text{m}$. According to the numerical calculations, the red-shift caused by the presence of the Si substrate is thus of a factor of 2.46. This reduces the length of the nanorod to $L \approx \lambda_0/7$ in order to achieve resonance at the free-space wavelength λ_0 . This observation is important for chapters 3 and 5, where $L = 1.5 \mu\text{m}$ long gold nanorods situated on top of a Si substrate show a far-field extinction resonance near 10 μm wavelength.

For comparison with the experimental near-field maps presented in the chapters 3 and 5, we calculate the near-field distribution of the nanorod of Figure 7a, evaluated at its resonance $\lambda_{\text{Si}} = 7.12 \mu\text{m}$ and in 30 nm above the nanorod surface. In Figure 7c, we display the amplitude and phase of the three components of the calculated electric field E . For the z-component, we observe strong amplitude values on top of the nanorod at the nanorod ends. The corresponding phase image shows the typical dipolar mode with a phase jump at the nanorod center. The x-component reveals strong fields at the nanorod ends, which are of the same phase at both rod ends (red color in the phase image). The y-component shows a quadrupolar pattern in the phase image. The amplitude maxima are located close to the rod ends and are of similar strength as the maxima found with the z- and x-component.

Interestingly, in case of mid-infrared resonant nanorods on top of a dielectric substrate, it has been shown that the resonances can be described by assuming that the nanorod is embedded in a homogeneous effective medium^{47,48}. The refractive index n_{eff} of the effective medium is calculated as the average of the refractive index of the substrate $n_d = \sqrt{\epsilon_d}$ and of air ($n \approx 1$):

$$n_{\text{eff}} = \sqrt{\frac{1 + n_d^2}{2}}. \quad (14)$$

The nanorod resonances are then obtained according to

$$L = i(\lambda_{\text{eff}}/2n_{\text{eff}}), \quad (15)$$

where L is the nanorod length, i the order of the resonance, λ_{eff} the effective wavelength of the plasmon mode on the nanorod in vacuum and n_{eff} is the refractive index of the effective medium^{47,48}. For the configuration shown in Figure 7a, we the refractive index of the effective medium is $n_{\text{eff}} = 2.52$ when assuming a refractive index $n_d = 3.42$ (Palik¹⁰) for the Si substrate. This value is very close to the ratio 2.48 found between both peaks in Figure 7b. This agreement confirms that the effective medium approach is a good approximation for our system of a mid-IR resonant nanorod on top of a Si substrate, which supports our effective medium approach for modeling the antennas presented in chapters 3 and 5.

1.5.4. Optical response of coupled metal nanorods

An efficient nanoantenna is usually characterized by the generation of a large field enhancement and an efficient transfer of most of the captured energy into small volumes³¹. The metal nanorods presented in chapter 1.5.2 and 1.5.3 produce localized fields at the rod ends that are enhanced in comparison to the incident field. The field enhancement and localization can be improved by introducing small gaps in the nanorod. This can be realized, for instance, by cutting a gap into the nanorod center. Equivalently, the same configuration is obtained when two individual nanorods are put very close together so that they are separated by a nanoscale gap. The near-field coupling of the LSP modes on each nanorod segments generates a charge localization at the gap⁶. As a function of the gap width, this coupling dramatically increases the near-field enhancement at the gap when compared to an isolated nanorod segment^{6,55,60,69}. The extreme near-field enhancement in nanoscale antenna gaps is also observed with coupled disks²¹ and two coupled triangles (bowtie antenna)⁶⁹⁻⁷¹. This property of coupled nanoparticles in general is the basis for several applications. For example in surface-enhanced Raman scattering (SERS)^{19,20} the near-field enhancement in the gap boosts the Raman signal by the order of 10^{14} to 10^{15} in comparison to the Raman signal without any nanoparticles, and thus enables the detection of Raman spectra from single molecules. Further examples at visible frequencies are optical (bio)sensors¹⁸ and optical nanolithography²³. Coupled nanorods with resonances in the mid-infrared spectral region enhance applications such as cascade laser emission⁷², infrared detectors¹⁷, surface-enhanced infrared spectroscopy (SEIRA)¹⁶.

In the following, we demonstrate numerically that extremely high near fields are generated at mid-infrared wavelengths when two micrometer-long metal nanorods couple across a very small gap. We assume two nanorods of $2\ \mu\text{m}$ length each that are aligned on the same axis and separated by a small gap of width g . Here, the same configuration as in chapter 1.5.2 is assumed, i.e. both rods are situated in vacuum and are illuminated with a plane wave perpendicular to the rod's long axis. While changing the gap width g , we monitor the position of the far-field extinction peak λ_{ff} of the dipolar response of the coupled nanorods (Figure 8a). We observe a red shift of the fundamental

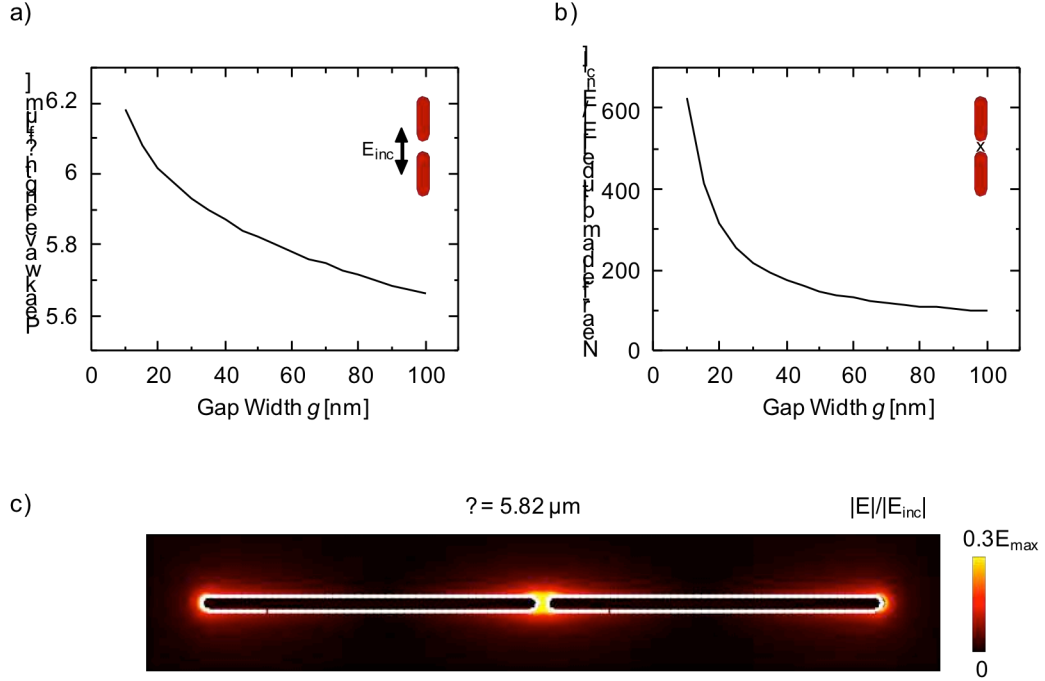


Figure 8: Dependence of the optical response of a pair of coupled identical Au nanorods (2000 nm long, 40 nm radius) separated by a gap of width g . (a) Position of the far-field extinction peak as function of the gap width g . (b) Near-field amplitude taken at a distance of 5 nm from the inner end of the upper nanorod, as a function of the gap width g . (c) Numerically calculated field profile for a gap width $g = 50$ nm and at the far-field extinction peak occurring at $\lambda = 5.82$ μm .

dipolar mode from about $\lambda_{ff} = 5.66$ μm to about $\lambda_{ff} = 6.18$ μm wavelength when the two rods approach from $g = 100$ nm to $g = 10$ nm. This red shift can be assigned to an increasingly stronger coupling across the gap which induces a depolarization of the charge oscillation on the individual rods⁶. In comparison to the individual rod with a resonance at $\lambda_{ff} = 5.26$ μm (Figure 6c), the red shift is quite considerable, amounting to about 17% for the case of the narrowest gap $g = 10$ nm. In Figure 8b, we monitor the near field enhancement $|E|/|E_{inc}|$ generated inside the gap when the gap width g is decreased. The near fields are measured at a distance of 5 nm from the inner cap of the upper nanorod. We observe that the near-field amplitude $|E|$ is enhanced up to 600 fold the incident field $|E_{inc}|$ for the narrowest gap $g = 10$ nm. For larger gap widths, the near-field enhancement approaches that of the individual nanorod⁶, which amounts to

$|E|/|E_{\text{inc}}| \approx 100$ (compare with Figure 6d). To show where the hot spots are generated in the system of two coupled nanorods, we show in Figure 8c the near-field distribution of the rods for the case $g = 50$ nm. There, we take a cross section of the rods along the long axis of the rod. We observe that the highest fields are generated at the gap, with fields of less strength also being generated at the outer ends of the rods.

The hot spots in nanoscale antenna gaps are an active topic in the research field of plasmonics and are an important part of this thesis. In chapter 4, we demonstrate that these hot spots can be mapped with our transmission mode s-SNOM. In chapter 5, we show that by filling the gap with metal bridges, the antenna mode is decisively changed. In chapter 6, we connect two metal wires (transmission line) to the antenna gap and show that the fields in the hot spots can propagate along the transmission line in form of a tightly confined surface wave.

2. Introduction to Antenna Theory

An antenna describes a device that is able to connect a source or receiver to free space¹. In communication applications such as radio and television broadcasting, they convert the electromagnetic waves travelling in free space into electric currents at the antenna gap, where they can be processed in a receiver circuit (e.g. a radio). In these applications, the antennas are usually operated at frequencies from 3 kHz up to several hundred GHz, which is termed the radio frequency (RF) range. A complete theoretical framework termed antenna theory has been developed that can be applied to the analysis, design and characterization of RF antennas¹. The visible and infrared light is also part of the electromagnetic spectrum and is located at frequencies in the range of a few to several hundred THz. This implies that in principle it should be possible to extend antenna theory towards these optical frequencies, offering the potential for a technology breakthrough in terms of better bandwidth, higher data rate and miniaturization when compared to their RF counterparts^{9,73}. The transfer of RF antenna methodology to optical frequencies may also provide new ideas for the design of optical antennas. This is an interesting and promising topic of ongoing research. One example is the loading concept which has been demonstrated theoretically to enable the tuning of the optical response of gap nanoantennas by loading them with dielectric or metallic particles⁹.

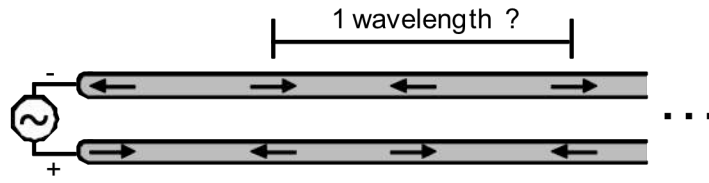
This chapter gives a short introduction on basic antenna theory concepts. These include RF transmission lines, RF dipole antennas, impedance concept and coupling of antennas to transmission lines. Finally, three examples will be presented where antenna theory concepts have been successfully transferred to optical frequencies.

2.1. Transmission lines

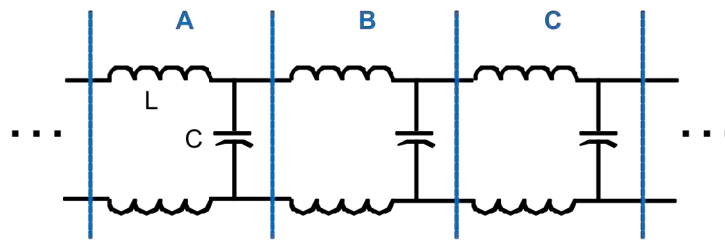
A transmission line is a cable that connects a source of alternating current (generator) to another device where this alternating current is processed (receiver). The sole purpose of transmission lines is to carry power from the generator to the receiver in an efficient way⁷⁴. The simplest realization is found with a single metal wire which transfers power via non-radiating surface waves. To limit the radial extension of the fields, the surface of the metal wire can be modified (e.g. by being threaded) or a thin dielectric coating can be applied (Goubau lines)⁷⁵. However, single wires are not practical because they tend to radiate the RF signals when bent or when foreign objects are placed on the line. Radiation losses can be prevented by choosing other types of transmission lines such as the two-wire lines (Figure 9a) or coaxial lines⁷⁴. With these lines, the electromagnetic field from each wire is balanced by the field of the other, resulting in an ideally zero field everywhere in space. In the following, we will describe the characteristics of the two-wire transmission line because this geometry has great potential to be adapted to optical and infrared frequencies due to its easy fabrication on the nanoscale.

The two-wire transmission line consists of two parallel aligned and closely spaced conductors (Figure 9a)^{1,74}. When an RF generator is connected to one end of the transmission line, an electromagnetic wave can be launched along the wire. The electromagnetic wave does not propagate at infinite speed, but at a speed of nearly the velocity of light c . Therefore, the momentary currents related to the electromagnetic wave are of different phase for different positions along each wire. This is illustrated in Figure 9a, where black arrows mark the direction of the momentary currents on each wire. The distance between two points of the same phase defines one wavelength λ . This is the distance the electromagnetic wave travels for each oscillation cycle of the generator signal. In Figure 9a, the wavelength λ can be determined by the distance between two neighboring arrows pointing in the same direction. A particular property of two-wire transmission lines is that they belong to the group of balanced lines and thus need to be driven by a balanced source, i.e. a positive signal is applied to the first wire and a negative signal of the same amplitude to the second wire. This operation mode is

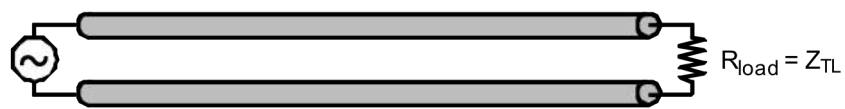
2.1 Transmission lines



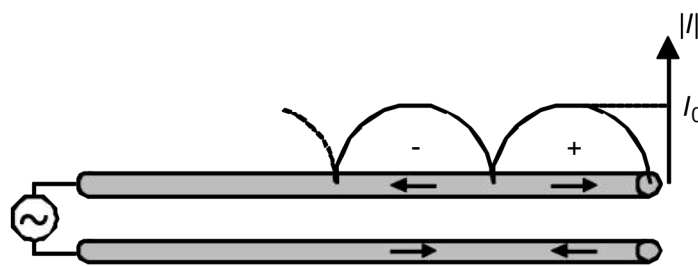
(a) Momentary currents on an infinite two-wire transmission line



(b) Equivalent of an ideal transmission line of impedance Z_{TL}



(c) Two-wire transmission line, terminated in a resistive load



(d) Two-wire transmission line, open circuited

Figure 9: Transmission lines [adapted from ARRL antenna handbook¹].

well suited for preventing radiation losses from the transmission line. Because the current flow in both wires is opposite at any point along the transmission line, the related electromagnetic fields of each wire are 180° out of phase. When the distance between the wires is kept sufficiently small (less than 1% of the free-space wavelength), the resultant field is almost zero at every point in space and a nearly complete cancellation of the electromagnetic fields can be achieved⁷⁴.

When a generator applies a certain voltage to the transmission line, the related current flow in the transmission line is not infinite, but rather depends on the applied voltage. From the point of view of the generator, the transmission line thus looks like an impedance. The impedance of a transmission line can be described by a series of inductors L and capacitors C . As indicated by the blue vertical bars, each pair of L and C corresponds to a short section of the transmission line (Figure 9b). In this picture, an electromagnetic wave propagating along the transmission line is represented by a power transfer from one section to its adjacent section (i.e. from A to B, from B to C and so on). For an ideal transmission line, the characteristic impedance Z_0 is given by⁷⁴

$$Z_{\text{TL}} = \sqrt{L/C}, \quad (16)$$

where L and C are the inductance and capacitance, respectively, per unit length of line⁷⁴. The impedance of a transmission line relates the current flow in the transmission line to the applied voltage. Note that the impedance of a lossless transmission line is purely real valued⁷⁴. The impedance of a transmission line can be measured, e.g. via the voltage to current ratio at the generator or by the standing wave ratio when a load is connect to the transmission line. Typical values for the characteristic impedance range from 200Ω to 800Ω for two-wire transmission lines, and from 30Ω to 100Ω for coaxial lines⁷⁴. In general, for two-wire transmission lines, the inductance L decreases with increasing conductor diameter, yielding lower impedance values. Likewise, the capacitance C decreases with increasing spacing between the two conductors, yielding higher impedances for the transmission line.

The current travels in transmission lines at (almost) the speed of light. Therefore, a signal requires a certain amount of time to travel along the transmission line. In case of an infinite lossless transmission line, the signal would travel forever. Real world

2.1 Transmission lines

transmission lines are, however, usually terminated in a load to which the power is delivered. If the load is purely resistive and matches the characteristic impedance of the transmission line ($R_{\text{load}} = Z_{\text{TL}}$), the current travelling along the transmission line finds that the load looks like an infinitely long transmission line of the same characteristic impedance⁷⁴ (Figure 9c). Then, all of the power is dissipated in the load and the transmission line is said to be matched. In case the load is not equal to Z_{TL} , the transmission line is said to be mismatched. The power reaching the load is only partially absorbed while the other part is reflected back into the transmission line. This is because the voltage to current ratio is different for the load. An extreme case of a mismatched transmission line is shown in Figure 9d, where the right end is open-circuited. In this configuration, the travelling-wave current is completely reflected from the open end with a 180° phase shift in order to satisfy the zero-current condition at the end. This reflection is expressed in modulations of the current amplitude which are called standing waves because of their stationary and wave-like character⁷⁴. In case of non-resistive loads such as a pure reactance, the load will consume no power and all of the energy arriving at the load will be reflected back into the transmission line. Reactive termination are used for phasing and special matching applications⁷⁴.

2.2. Linear dipole antenna

A linear dipole antenna can be constructed by bending apart the open-circuited transmission line from Figure 9d until the configuration depicted in Figure 10a is obtained. After the bending, it can be assumed that the standing wave pattern of the open-circuited transmission line has been essentially maintained¹. However, because of this new geometry, the fields radiated by each wire are not cancelled by those of the other wire. Therefore, there is a net radiation from the bended part of the transmission line¹. The power that is radiated by the dipole antenna is delivered via the transmission line from a distant source or generator. The point where the transmission line connects with the antenna is called the feed point.

The radiation from the dipole antenna is dependent on the antenna length l (in this thesis measured from antenna end to antenna end). For antenna lengths l smaller than the wavelength λ , the currents on both antenna arms point in the same direction (Figure 10b-c). Thus the fields radiated from each segment reinforce each other in most directions¹. For antennas with lengths l larger than the wavelength λ (Figure 10d), the current distribution on the antenna yields 180° phase jumps for every half of the wavelength λ , yielding parts of the antenna with currents pointing in the opposite direction. Therefore, the fields radiated from some parts may interfere destructively with the fields radiated from other parts of the antenna, leading to a field cancellation in certain directions¹.

One of the most important characteristics which define an antenna is its self impedance Z_A . The definition of the impedance for an antenna is motivated by the fact that the current flow into the antenna's feed point in Figure 10b-d must be supplied at a finite voltage. The self impedance is measured at the feed point of the antenna and is defined as the voltage applied to the feed point divided by the current flowing into the feed point^{1,74}. The self impedance describes the antenna in a state when it is located completely away from the influence of any other conductors.

2.2 Linear dipole antenna

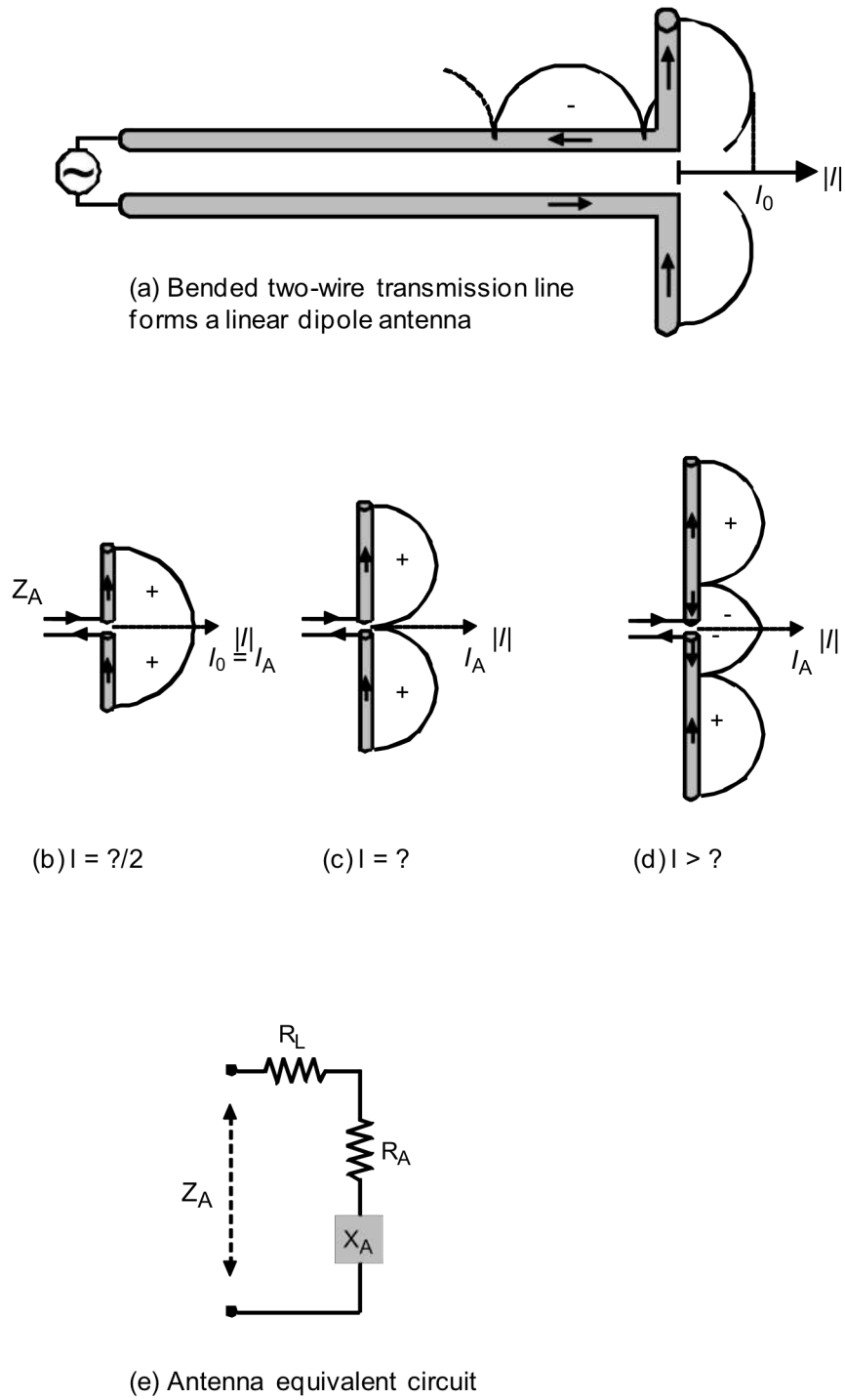


Figure 10: Linear dipole antenna [adapted from Balanis¹].

The antenna self impedance antenna Z_A is assembled by three impedance components (Figure 10e):

$$Z_A = R_A + R_L + iX_A . \quad (17)$$

The antenna resistance R_A describes the energy dissipation due to the radiation of electromagnetic waves. The loss resistance R_L describes the energy dissipation in form of heating the antenna wire and nearby dielectrics. The antenna reactance X_A describes a possible inductive or capacitive behavior of the antenna and is related to the presence of resonances in the antenna. If the antenna reactance X_A is zero, the antenna is termed resonant and it appears as a pure resistance to the transmission line. On the other hand, certain types of antennas do not have any resonances and consequently also have zero antenna reactance X_A (ref. ⁷⁴).

The antenna impedance Z_A of a linear dipole antenna changes strongly with the operation frequency. To study this dependence, we describe in the following the equations for the antenna impedance Z_A of a linear dipole antenna. These equations are the result of an analytical treatment of the linear dipole antenna applying the Induced EMF Method. In this method, it is assumed that the antenna is center-fed and that the currents vanish at the antenna end points. Moreover, a sinusoidal current distribution is assumed, as depicted in Figure 10b-d. The electric and magnetic fields of the dipole antenna are calculated assuming a zero radius. Then, the Poynting vector is integrated over a cylindrical surface that coincides with the actual antenna radius a . However, the Induced EMF Method yields good results only for small radii (usually limited to $a < \lambda/100$). For details on this method, please refer to chapter 8.5.2 in ref. 1. The result of the Induced EMF Method is the self impedance of the antenna $Z_A = R_A + iX_A$ related to the current at the feed point of the antenna:

$$\begin{aligned}
 R_A(k, l, \eta) = & \frac{\eta}{2\pi \sin\left(\frac{kl}{2}\right)^2} \left\{ C + \ln(kl) - C_i(kl) \right. \\
 & + \frac{1}{2} \sin(kl) [S_i(2kl) - 2S_i(kl)] \\
 & \left. + \frac{1}{2} \cos(kl) [C + \ln(kl/2) + C_i(2kl) - 2C_i(kl)] \right\}
 \end{aligned} \tag{18}$$

$$\begin{aligned}
 X_A(k, l, a, \eta) = & \frac{\eta}{4\pi \sin\left(\frac{kl}{2}\right)^2} \left\{ 2S_i(kl) + \cos(kl) [2S_i(kl) - S_i(2kl)] \right. \\
 & \left. - \sin(kl) \left[2C_i(kl) - C_i(2kl) - C_i\left(\frac{2(ka)^2}{kl}\right) \right] \right\}
 \end{aligned} \tag{19}$$

where $C = 0.5772$ is Eulers constant, $C_i(x)$ and $S_i(x)$ are the cosine and sine integrals, k is the wave vector of the electromagnetic wave, l is the antenna length, a is the antenna radius and η the impedance of the surrounding medium (for free-space $\eta = 377 \Omega$). Note that here we assumed a lossless antenna ($R_L = 0$).

We plot the antenna impedance $Z_A = R_A + iX_A$ of a linear dipole antenna as a function of the antenna length l and for different antenna radius a in Figure 11a. Here, we express the antenna length l and radius a in units of the wavelength λ . This is motivated by the fact that in the equations (18),(19), the length l and radius a only appear as the product kl and ka , respectively. Please note that only one curve is shown for R_A because it is independent of the antenna radius a . The plots of the antenna resistance R_A and antenna reactance X_A reveal the antenna resonances. We observe zero crossings of the antenna reactance X_A at approximately $l = \lambda/2, 1\lambda$ and $3/2\lambda$ that correspond to the half-wave, full-wave and 3/2-wave resonances of the linear dipole antenna. These resonances are accompanied by low values for the antenna resistance R_A in case of the half-wave and 3/2-wave resonances. In contrast, the full-wave resonance yields an infinite antenna resistance R_A because of the denominator in eq.(18) becomes zero. In practice, this is not the case, but the antenna resistance R_A can still reach very high values¹. In general, the antenna resonances can be classified in odd resonances with a low antenna resistance R_A appearing near $l = (2n + 1)\lambda/2$ and in even resonances with a high antenna resistance R_A , appearing near $l = n\lambda$, where n is an integer number. Usually, it is difficult to

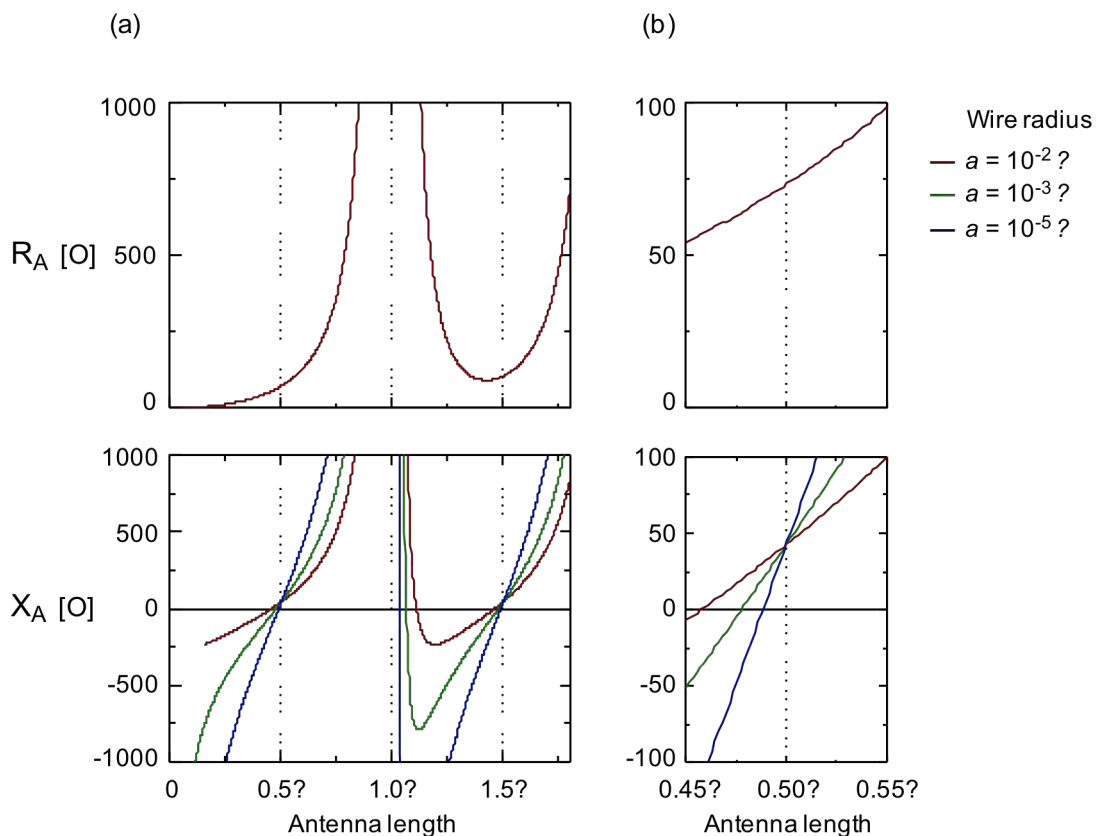


Figure 11: Antenna resistance R_A and antenna reactance X_A of a linear dipole antenna evaluated with antenna theory. (a) R_A and X_A is plotted as a function of antenna length l (in units of the wavelength λ) in the range $0 \leq l \leq 1.8\lambda$. (b) same as (a), but the antenna length is varied only around the first half-wave resonance at $\lambda/2$. There antenna resistance R_A and reactance X_A is plotted for three different antenna radii a . Note that all three curves coincide for R_A because it is not dependent on the radius a .

2.2 Linear dipole antenna

operate antennas at resonances with high resistance R_A because high voltages are necessary in order to transmit with sufficient power⁷⁴. Therefore, the dipole antenna is generally operated at odd resonances, and most often near its half-wave resonance $l = \lambda/2$ due to size considerations at RF.

To study the influence of the antenna radius, in Figure 11b we show the antenna resistance R_A and reactance X_A near the half-wave resonance length for the three antenna radii $a = 10^{-2}\lambda$, $10^{-3}\lambda$ and $10^{-5}\lambda$. The plot shows a slowly changing antenna resistance R_A and three straight lines of different slopes for the antenna reactance X_A . Here, the thin antenna (blue curve) shows a higher slope than the thick antenna (red curve). This indicates that thin (thick) antennas have a high (low) Q factor and thus a sharp (broad) antenna resonance. The three lines coincide at $X_A = 42.5 \Omega$ at $l = \lambda/2$ for all three antenna radii. It is surprising that the antenna reactance is of non-zero value at exactly $l = \lambda/2$. In fact, as it is clearly revealed in Figure 11b, the antenna resonance ($X_A = 0$) occurs for antenna lengths slightly smaller than $\lambda/2$ and in the range of 0.45λ to 0.5λ . The general trend is that the thinner the antenna is, the closer is the antenna resonance located to $\lambda/2$. Only in the limit of an infinitely small antenna occurs the antenna resonances at exactly $l = \lambda/2$ (ref. ⁷⁴). For antenna lengths smaller than the resonant antenna length, the antenna reactance becomes negative and the antenna shows a capacitive reactance. Conversely, the antenna reactance becomes positive and thus inductive for larger antenna lengths.

2.3. Transfer of antenna theory concepts to optical frequencies

In the following, we will present three examples of the transfer of antenna theory to optical frequencies.

2.3.1. Scaling law for optical antennas

At radiofrequencies, the antenna parameters such as the antenna self-impedance are directly related to the frequency of the incident radiation⁷. Therefore, any antenna design can be scaled in size in order to use it at a different frequency. This frequency scaling is described by⁷⁴

$$d' = \frac{\omega}{\omega'} \cdot d, \quad (20)$$

where d and ω are the dimension and the operating frequency of the original design and d' and ω' are the dimension and operating frequency of the scaled design. This frequency scaling can be applied to a wide range of radiofrequencies because metals behave in good approximation like perfect electric conductors at these frequencies. However, the frequency scaling fails at optical frequencies because at these frequencies the metal no longer behaves as a perfect metal. Instead, the metal is penetrated significantly by the electromagnetic fields and its response is mainly dictated by the collective electron oscillations^{7,38} (chapter 1.1). This yields a strong dispersion of the surface charge waves which is described by an effective wavelength λ_{eff} (chapter 1.2). Consequently, antennas at optical frequencies do not respond to the external wavelength $\lambda = c/\omega$, but to the shorter effective wavelength $\lambda_{\text{eff}} < \lambda$ (ref.⁷ and chapter 1.5). Therefore, λ_{eff} instead of λ must be used in the related antenna equations. However, the effective wavelength λ_{eff} depends on the material properties and does not necessarily scale linearly with the frequency, thus preventing the application of the frequency scaling

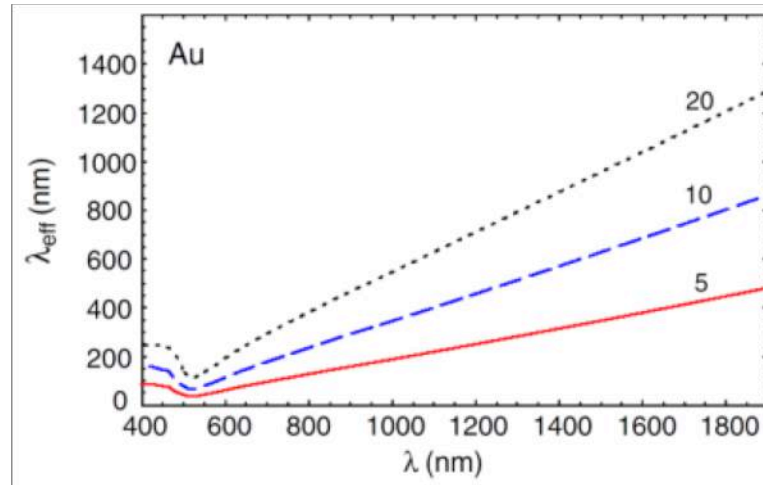


Figure 12: Effective wavelength scaling for metal rods made of gold. The curves show the effective wavelength λ_{eff} as a function of the free-space wavelength λ for the three different rod radii $a = 5$ nm, 10 nm and 20 nm. The curves were obtained by numerical calculations and show that a linear scaling law (see text) is a good description for wavelengths $\lambda > 500$ nm as long as the rod radius a is small in comparison to the wavelength λ . [taken from ref. ⁷]

law at optical frequencies. One approach to remedy for this situation is the introduction of a linear scaling law for λ_{eff} (Figure 12). This scaling law expresses the effective wavelength λ_{eff} as a linear dependence on the free-space wavelength λ according to $\lambda_{\text{eff}} = n_1 + n_2[\lambda/\lambda_p]$ where n_1 , n_2 are coefficients related with the antenna geometry and static dielectric properties and λ_p is the plasma wavelength of the metal⁷. This scaling law is valid if the radius a of the antenna is much smaller than the wavelength λ and if the Drude model can be applied to describe the electron gas in the metal⁷. By inserting this scaling law in the relevant equations, antenna theory can be applied to optical frequencies. This enables the design of optical antennas, i.e. calculating their resonance frequencies, by evaluating equations from antenna theory without the need to perform time-consuming numerical calculations of the electromagnetic response of the optical antennas.

2.3.2. Antenna loading for tuning optical antennas

The second example is antenna loading which allows for operating an antenna at frequencies different than its natural resonance frequencies. Typical RF antennas are purely resistive only when operated at its natural resonant frequencies (see chapter 2.2). If the antenna is operated non-resonantly, the antenna exhibits a non-zero reactance X_A . In transmitting mode, this non-zero reactance X_A causes that part of the energy that is fed into the antenna is reflected back to the generator, which decreases the transmitting efficiency^{1,74} (chapter 2.1). To explain the antenna load concept, in the following we assume an antenna with a capacitive antenna reactance $X_A < 0$, corresponding to the case where an antenna is too short for the desired operating frequency. In this case, we evaluate the antenna impedance Z_A at the desired frequency and described it by an equivalent circuit consisting of a resistance R and a capacitance C (dashed box in Figure 13a). To operate efficiently this antenna at the desired frequency, an inductive load X_{load} (represented by inductor L) can be connected in parallel to the feed point^{1,74} (Figure 13a,b). The combination of the antenna impedance Z_A with the load X_{load} then forms the input impedance Z_{in} that is now seen at the feed gap of the antenna according to

$$\frac{1}{Z_{in}} = \frac{1}{Z_A} + \frac{1}{iX_{load}}. \quad (21)$$

By properly choosing L , the inductive load X_{load} (inductor L) resonates with the capacitive reactance X_A (capacitor C) at the desired frequency, thus canceling X_A . As a result, the antenna thus appears as a pure resistance as if it was operated at its intrinsic resonant frequency, thus allowing for an efficient antenna operation at the desired frequency. At optical frequencies, Alu et al.^{9,73} proposed that the frequency response of optical antennas can be tuned by loading the antennas with optical nanocircuits (Figure 13c). Being the optical equivalent to inductors and capacitors at radiofrequencies, these nanocircuits are small nanoparticles of metallic ($\epsilon' < 0$) or dielectric ($\epsilon' > 0$) character that act as

2.3 Transfer of antenna theory concepts to optical frequencies

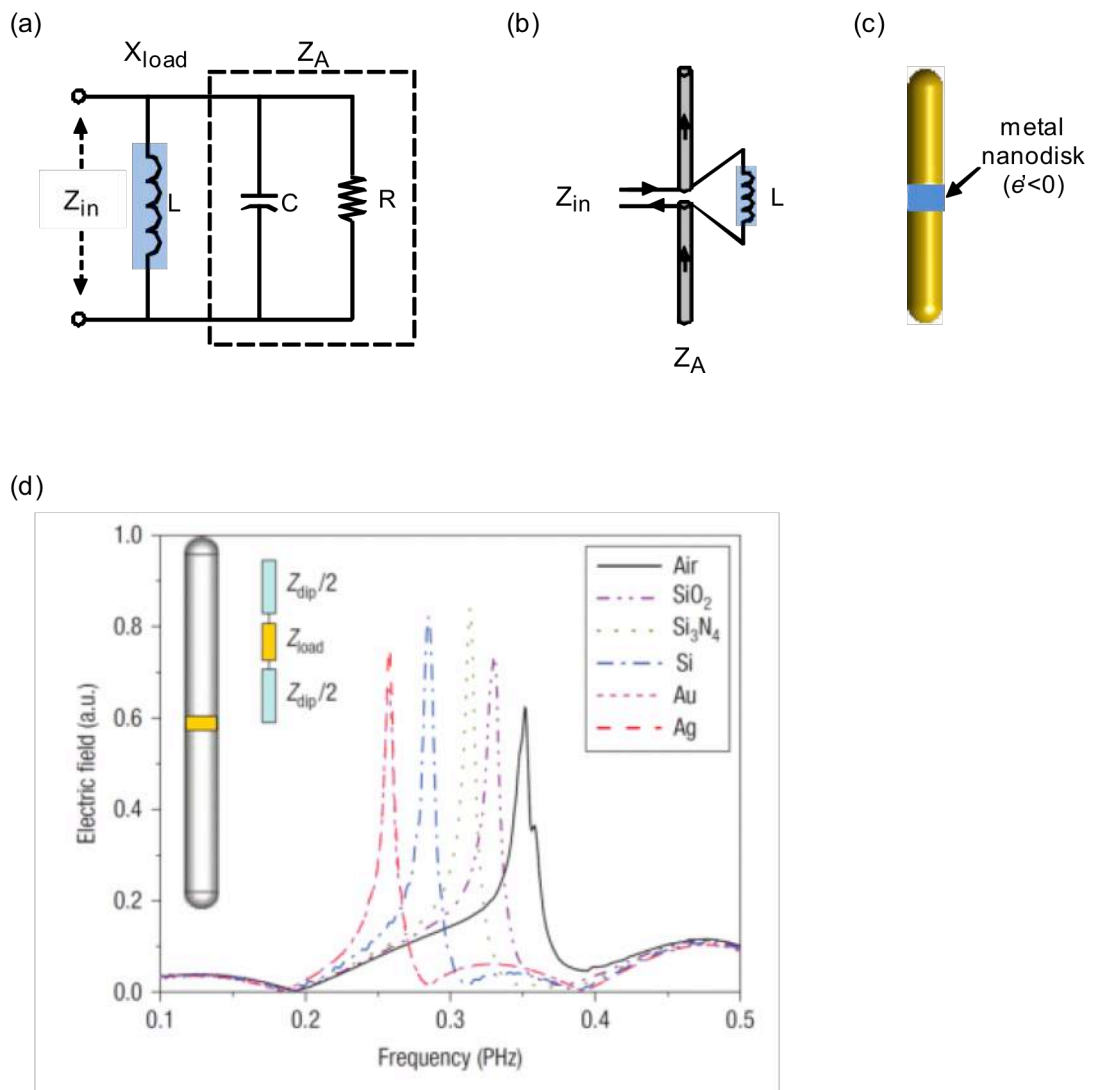


Figure 13: Tuning antennas with antenna loading. (a) Equivalent circuit for an antenna (dashed box) where the antenna impedance Z_A is represented by R and C . This antenna is loaded with the inductor L , yielding an impedance Z_{in} at the antenna feed point. (b) RF dipole antenna loaded with an inductor (c) Optical antenna loaded with a metal disk that acts as nanoinductor. (d) Numerically calculated far-field scattered field of a silver nanorod with a gap that is filled with different materials. Nanodisks made of dielectrics such as SiO_2 , Si_3N_4 and Si act as nanocapacitors, nanodisks made of metals such as Au and Ag act as nanoinductors. Panel (d) is taken from ref. ⁹.

nanoinductors and nanocapacitors at optical frequencies, respectively^{76,77}. Alu et al. observed in a numerical study that the resonance of the optical antenna can be shifted by filling the gap of the antenna with such nanocircuits. This is illustrated in Figure 13d which shows that the far-field spectra of a silver nanorod are shifted by filling its gap with different materials. Particularly, these shifts could be predicted with circuit theory. To this end, they calculated the impedance of a nanocircuit in the form of a small disk according to^{9,73}

$$R_{\text{load}} - iX_{\text{load}} = \frac{i \cdot t}{\omega \epsilon \epsilon_0 \pi a^2}, \quad (22)$$

where t and a are the height and the radius of the nanodisk, ϵ the dielectric constant of the material constituting the disk, ω the operation frequency and ϵ_0 the vacuum permittivity. Please note the minus sign in front of X_{disk} in conformity with ref. ⁹. Evaluating the input impedance according to eq. (21), the resonance condition $Z_{\text{in}} = 0$ predicted the actual resonance found in the numerical calculations. Therefore, loading the gap of plasmonic antennas provides a versatile means to tune the response of optical antennas. Moreover, it could facilitate a better matching to other nanocircuit elements such as to optical transmission lines (ref. ⁷⁸ and chapter below). The description of the load by an impedance has strong potential to be combined by describing the optical antenna with antenna theory and the scaling law (chapter 2.3.1), offering a more sophisticated optical antenna design. In chapter 5, we will apply this loading concept in order to explain the resonance shifts of infrared antennas when their central gap is loaded with metal bridges.

2.3.3. Applying impedance matching to optical nanocircuit

The third example is the concept of an optical nanocircuit consisting of a receiving and an emitting antenna that are connected by a two-wire transmission line (Figure 14). Huang et al. ⁵ demonstrated numerically, that when illuminating the receiving antenna with an external field, the antenna launches a surface wave in the transmission line. The

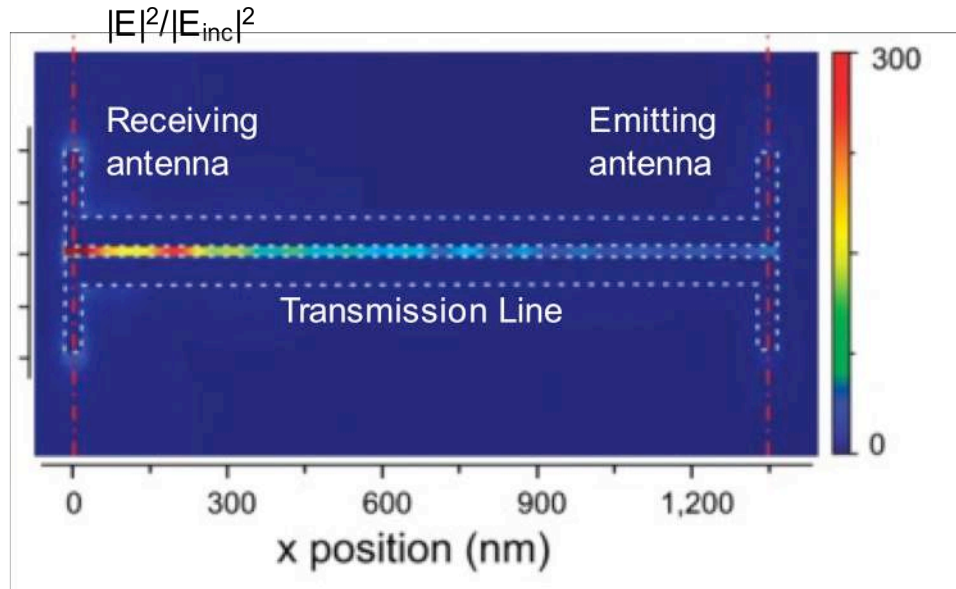


Figure 14: Optical nanocircuit consisting of a receiving antenna, a two-wire transmission line and an emitting antenna. Shown is the electric field intensity in a parallel plane at middle height of the structure. Taken from ref. ⁵.

transmission line transports the energy to the emitting antenna that in turn converts the surface wave back into a propagating electromagnetic wave. Because the emitting antenna is a priori not impedance matched with the transmission line, a partial reflection of the surface wave from the emitting antenna occurs, giving rise to a standing wave pattern on the transmission line (chapter 2.1). This standing wave pattern can be recognized in Figure 14 as the modulation of the fields inside the transmission line. Taking chance of the fact that the impedance Z_A of the emitting antenna can be tuned by changing its lengths and width (see chapter 2.2), they showed that it is possible to obtain a nearly perfect match with the transmission line impedance Z_{TL} , which is given by

$$Z_A = Z_{TL} . \quad (23)$$

The introduction of the impedance concept for optical nanocircuits and the proposed method for determining the impedance has great importance for an efficient design and optimization of nanocircuits operating at optical frequencies.

3. Transmission-mode s-SNOM

The characterization of plasmonic nanostructures requires the resolving of subwavelength-scale features in local optical field distributions. Different techniques exist that beat the diffraction limit of conventional optical techniques and provide access to the nanoscale confined fields in e.g. plasmonic antennas and waveguides. One particularly versatile method is scattering-type scanning near-field optical microscopy (s-SNOM) where a sharp tip scatters the optical fields close to the sample surface. This technique achieves nanoscale resolution in the wide spectral range from visible to THz frequencies. Here, we present the development of a transmission-mode interferometer setup for s-SNOM with the aim to provide a homogeneous illumination of the sample. We demonstrate our technique by mapping metallic nanorods, disks, and triangles, designed for antenna resonance at mid-infrared frequencies, in good agreement with numerical calculations of the modal field distribution. We also provide a detailed analysis of the image contrast in s-SNOM mapping of the antennas. Our results establish a basis for future near-field characterization of complex antenna structures for molecular sensing and spectroscopy.

3.1. Introduction

Experimental techniques are important for the characterization of plasmon resonances in metal nanostructures. This is motivated from a fundamental point of view in order to learn about the plasmonic response of real structures. Also, there is a great need for evaluating the performance of applications where plasmon-resonant structures are the key element. The characterization of plasmon resonances is usually done with spectroscopy methods, yielding the far-field scattering and absorption of metal nanostructures. The complete characterization, however, requires the access to the near field of plasmonic resonances because the near field contains valuable information such as the intensity of the local field enhancement or the mode structure of the plasmon resonance (chapter 1.3). This is difficult to obtain because microscopy techniques are required to spatially resolve the relevant structure sizes⁷⁹, which are much smaller than the diffraction limit. The near-field characterization of plasmon resonances is thus a challenge for classic optical instruments. Particularly, the near-field phase is an essential parameter in certain applications such as in coherent control applications⁸⁰ or in molecular spectroscopy based on plasmon-resonant nanoparticles. In the latter, the interference between molecule and plasmon near fields can significantly alter the spectral line shape of the molecules (similar to Fano resonances known from quantum physics)^{16,46}, giving rise to dramatic resonant effects that enhance the sensitivity and contrast of the spectral information.

There exist a variety of microscopy methods to map the near-field distribution of plasmonic nanostructures. The microscopy methods that probe the near fields in the far field are two-photon induced luminescence (TPL) microscopy^{55,60,69,81-85}, electron energy loss spectroscopy (EELS)⁸⁶ and two-photon photoemission electron microscopy (PEEM)⁸⁷⁻⁹⁰. TPL microscopy is based on interband transitions induced by a two-photon absorption process and a subsequent photoluminescence signal from a recombination process. Because the TPL signal is sensitive to the local electromagnetic field enhancement, TPL microscopy provides maps of their local field distribution⁶⁰ that can also be spectrally resolved⁸². In EELS, a highly-focused and monochromatic electron

3.1 Introduction

beam can excite plasmons in the metal nanostructures and thus loses energy.. The energy distribution of the transmitted electrons reflects the excitation of the different plasmon modes supported by the metal nanostructures^{86,91-93}. By analyzing the energy distribution, spectral information of the plasmon modes can be obtained^{91,93}. By raster scanning the electron beam across the metal nanostructures and detecting at a fixed energy, EELS also provides maps of the plasmon modes^{91,94-96}. In PEEM, the photoemission process is enhanced by the increase of the local electric fields⁹⁰. Imaging of the emitted electrons provides maps of the optical near field with the resolution of emission electron microscopy⁹⁰.

Near-field microscopy uses local probes to map the near fields of plasmonic nanostructures. The probes are brought very close to the sample surface into the vicinity of the near fields, where they locally convert the near fields into propagating fields. Common types of near-field microscopy techniques are photon scanning tunneling microscopy (PSTM)⁹⁷⁻¹⁰¹, aperture scanning near-field optical microscopy (aperture SNOM)¹⁰²⁻¹⁰⁷ and scattering-type scanning near-field optical microscopy (s-SNOM)^{52,72,79,108-117}. Each of these techniques employs a special kind of probe, which are summarized in Figure 15. A more detailed explanation will be given in the following.

In photon scanning tunneling microscopy (PSTM), the sample is usually illuminated from below in total internal reflection (Figure 15a). The local probe is a tapered dielectric optical fiber with a sharp tip apex. When brought close to the sample surface, the probe frustrates the total internal reflection and the near fields on the sample surface are coupled into the fiber. Because of the strong exponential decay of the near fields, the sharp tip apex allows for the mapping of the near fields with subwavelength resolution^{98,101}. PSTM has been applied for the near-field mapping of metal particles and for studying the interparticle coupling^{97,98}. PSTM has also been used for local field mapping in microcavities¹¹⁸, in waveguide structures¹⁰⁷ and SPPs in metal stripes¹¹⁹.

Aperture SNOM is similar to PSTM, but here the local probe is a tapered, dielectric fiber with an additional thin metal coating, yielding a small metal aperture at the fiber tip¹⁰²⁻¹⁰⁷ (Figure 15b). When the aperture probe is brought close to the sample surface, a small part of the near fields couples to the probe through the metal aperture. Here, the size of the metal aperture defines the lateral resolution for near-field mapping. At visible and

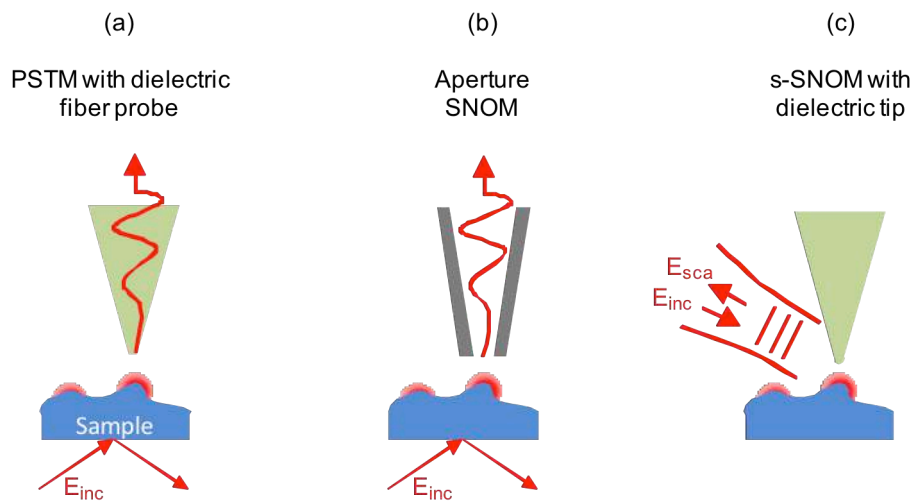


Figure 15: Techniques for the near-field mapping of plasmonic nanostructures.

near-infrared wavelengths, aperture probes have been applied to study the SPP propagation on planar metal films and on metal slabs¹²⁰⁻¹²⁴. However, aperture probes are difficult to use at mid-infrared wavelengths. This is because of a cut-off effect that is experienced in the metal coated fibers for diameters smaller than the wavelengths. For example, at a wavelength of $\lambda = 10 \mu\text{m}$, the transmission through a 100 nm diameter aperture is reduced to the very small part of 10^{-25} of the incident intensity¹²⁵.

In scattering-type SNOM (s-SNOM), light is focused on the sample either from below or from the side and excites local plasmon modes on the sample (Figure 15c). When brought near the sample surface, the near-field probe scatters the near fields on the sample surface. Because they are scattering probes, dielectric tips do not suffer from the low light throughput of aperture tips. Therefore, dielectric tips can be employed for the detection of near fields at optical^{52,79,108,115} and infrared frequencies¹¹⁷. The dielectric tips of commercial atomic force microscope (AFM) cantilevers are a common choice for the near-field probe^{79,108,115}. These can have a very sharp tip apex radius, e.g. below 10 nm is possible, which opens the way to achievable resolutions in near-field mapping in the range of 10 to 20 nm (refs. ^{108,115}). Until now, a detailed model for the image contrast formation is still an open question. Nevertheless, s-SNOM employing dielectric tips has been successfully applied for mapping the oscillation modes in plasmonic

3.1 Introduction

nanostructures^{79,108,115}. Despite these achievements, the s-SNOM technique for near-field mapping is confronted with several challenges. First, it is suspected that the presence of the probe might perturb the local near-field distribution on the sample surface^{60,112}. Such a perturbation can be minimized by employing dielectric tips such as Si tips because they are very weak scatterers^{115,126}. Secondly, the tip-scattered near fields are often masked by a strong parasitic background signal from bulk scattering of the sample and the tip^{79,127}. Because of the nonlinear decay of the near fields from the sample surface, the tip-scattered near fields can be extracted by higher-harmonic lock-in detection techniques^{52,72,79,108,111-117,127}. Note that also metal-coated tips have been employed to map the oscillation modes of plasmon particles^{108,111,114} and infrared antennas^{38,72,117,128}. However, these tips have a large conductivity even at optical frequencies and thus can induce resonance shifts, multipole excitation and damping in the oscillation modes of plasmonic nanostructures¹²⁶, which might yield distorted near-field maps of the sample.

In this chapter, we present transmission-mode s-SNOM¹⁰⁹ for the near-field mapping of plasmonic nanostructures at mid-infrared frequencies. In transmission-mode, the sample is illuminated from below through a transparent substrate. In this way, a homogenous sample illumination is provided, thus preventing retardation effects inherent to conventional side-illumination schemes^{52,79}. Furthermore, the transmission mode also avoids a direct excitation of the probing tip because the polarization of the incident beam is perpendicular to the tip's long axis. Chapter 3.2 gives a technical description of the transmission-mode setup. In chapter 3.3 we present a detailed analysis of the background in the optical images when employing dielectric tips. We will then show that this background can be satisfactorily removed, allowing for reproducible and quantitative mapping of the near field distribution, especially of the near-field phase. Finally, we apply this procedure to obtain the near fields in a variety of IR nanoantennas, thus showing the general applicability of the background subtraction method.

3.2. Description of the Transmission-mode s-SNOM setup

3.2.1. Near-field probing and interferometric detection

The transmission-mode s-SNOM microscope is based on a modified, commercial atomic force microscope (AFM) from the company JPK Instruments AG (www.jpk.com). We use commercial AFM cantilevers with dielectric tips of type PPP-FM and type PPP-RT-NCHR from Nanosensors (www.nanosensors.com). The AFM is operated in tapping mode where the AFM cantilever is oscillated at a frequency Ω close to its resonance frequency, which is typically located at around 300 kHz. The vibration of the cantilever is optically monitored with a readout laser and a four-quadrant detector¹²⁹. Imaging is performed by raster-scanning the tip in close proximity to the sample surface.

The detection of the near fields with dielectric scattering probes is illustrated in Figure 16. Here, a plasmonic antenna is illuminated from below through the transparent substrate with an incident field E_{inc} . The polarization of the field E_{inc} is chosen to be parallel to the long axis of the plasmonic antenna in order to excite the longitudinal plasmon modes in the antenna. The dielectric tip scatters the near fields of the plasmon modes (marked by the red field lines) according to

$$E_{\text{nf}} = \sigma_{\text{nf}} E_{\text{inc}} , \quad (24)$$

where σ_{nf} is the scattering coefficient of the system consisting of the antenna on the substrate and the tip. Because of a global sample illumination, parasitic scattering from the tip shaft and nearby objects on the sample surface contributes to a background signal, which is denoted here as E_{bkg} with

$$E_{\text{bkg}} = \sigma_{\text{bkg}} E_{\text{inc}} , \quad (25)$$

3.2 Description of the Transmission-mode s-SNOM setup

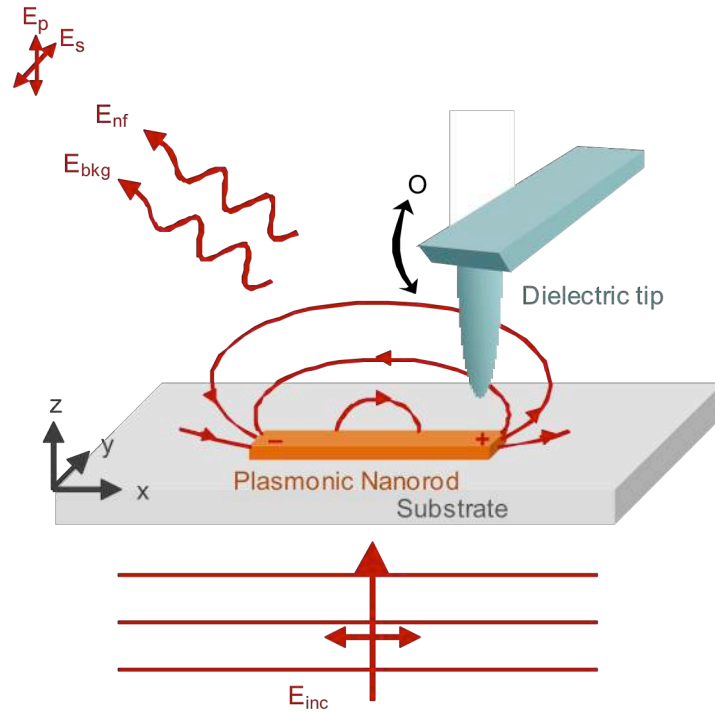


Figure 16: Mapping the near-field distribution of a plasmonic nanorod with dielectric scattering probes in transmission-mode s-SNOM.

where σ_{bkg} is the scattering coefficient describing the parasitic scattering. The tip-scattered light is collected with a parabolic mirror. Because the collecting mirror is diffraction limited, the tip-scattered light E_{tip} yields undistinguishable the sum of the near-field scattering E_{nf} and the background scattering E_{bkg} :

$$E_{\text{tip}} = E_{\text{nf}} + E_{\text{bkg}} \quad (26)$$

The tip-scattered light E_{tip} contains s- and p-polarized components, as indicated by E_s and E_p in Figure 16. In order to resolve the amplitude and phase of the tip-scattered light, a Mach-Zehnder interferometer is situated around the AFM. In the following, a detailed description of the setup will be given.

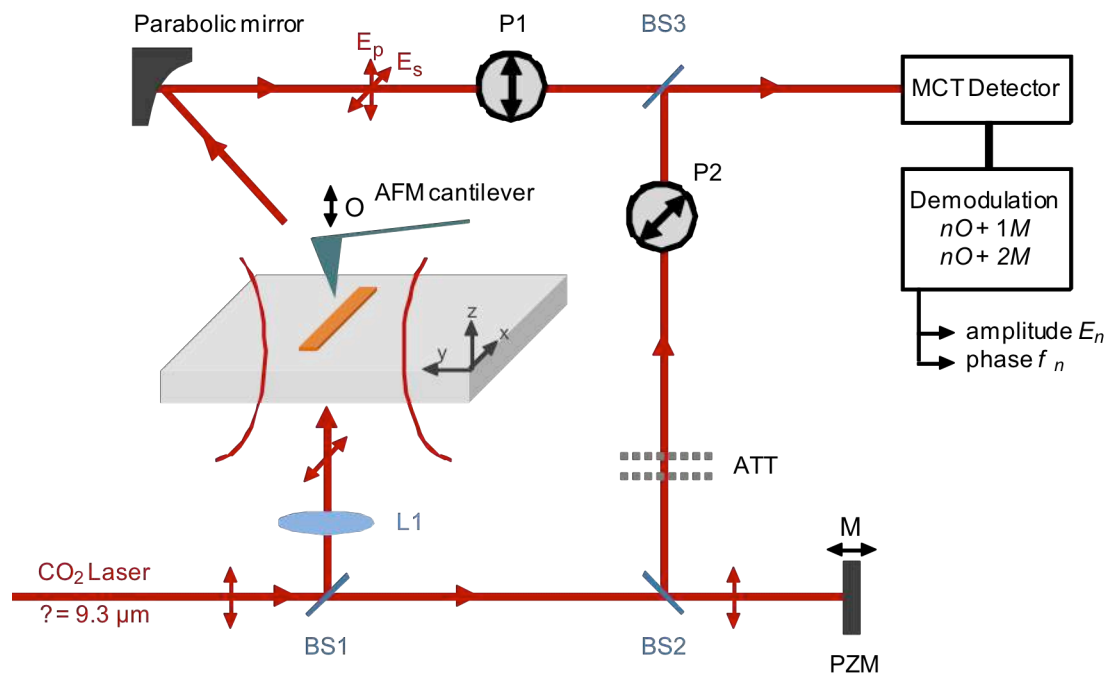


Figure 17: Setup of the transmission-mode s-SNOM with pseudoheterodyne detection. Used components: beam splitters BS1,BS2,BS3; lens L1; Attenuators ATT; Piezo-actuated mirror PZM; optional polarizers P1,P2.

Figure 17 shows the scheme of the Mach-Zehnder interferometer. The bottom part of this scheme shows the generation of the illuminating beam and the reference beam. For the sample illumination, a frequency-tunable CO₂ laser filled with the standard isotope gas (C12O16) is used. In this thesis, the CO₂ laser is operated in the wavelength range between 9.3 μm and 9.6 μm, where maximum power output is obtained. The vertical-polarized beam of the CO₂ laser is split by the ZnSe window BS1. The reflected beam is used for the illumination of the sample. Here, the lens LS1 with a low numerical aperture of $NA \approx 0.1$ provides a weakly focused beam that illuminates the sample surface with a spot size of about 50 μm diameter, allowing for a homogeneous illumination of even large structures. The transmitted beam from BS1 is used as the reference beam. The reference beam is reflected from a piezo-actuated mirror PZM, which can be vibrated at a frequency M , thus allowing for a modulation of the phase of the reference beam. The reference beam is then attenuated with free-standing metal grids ATT (www.lasnix.com) in order not to saturate the detector. The upper part of the scheme shown in Figure 17

shows the detection of the tip-scattered light. The tip-scattered light E_{tip} is collected above the sample with a parabolic mirror ($NA \approx 0.5$) under an angle of 60° to the surface normal. The collimated beam from the parabolic mirror is detected interferometrically by superimposing it with the reference beam at the ZnSe window BS3. Because the reference beam is polarized vertically, an interference with only the p-component E_p of the tip-scattered light is obtained. The combined beam is detected with a Mercury Cadmium Telluride (MCT) detector of type KMPV 11-0.2-J1 from the company Kolmar Technologies. The electric signal of the detector is high-pass filtered ($f_c = 8$ kHz, 4th order) in order to remove the contributions from static interferences. Then, the electric signal is amplified with a voltage amplifier with a setting of 10 dB or 20 dB.

In chapter 4 and 6, polarization-resolved measurements of the tip-scattered fields is required. To this purpose, the Mach-Zehnder interferometer shown in Figure 17 can be modified by inserting the polarizers P1 and P2 of model LP01 (www.lasnix.com). The polarizer P1 can be rotated freely. If aligned vertically or horizontally, the p-component E_p or the s-component E_s of the tip-scattered light is selected, respectively. The polarizer P2 is fixed to an angle of 45° , thus ensuring an equal interference with both p- and s-component of the tip-scattered light.

3.2.2. Signal detection

The detector signal is analyzed with a pseudoheterodyne detection scheme. In this detection scheme, the PZM mirror is vibrated at a frequency M , which yields a modulation of the phase of the reference beam. The electric field of the reference beam is described by

$$E_{\text{ref}} = e^{i\gamma \sin(Mt)} E_{\text{inc}}, \quad (27)$$

where γ is the amplitude and M the frequency of the phase modulation. Typical frequencies for M are in the range of 100 Hz to 1000 Hz. The detector signal is analyzed

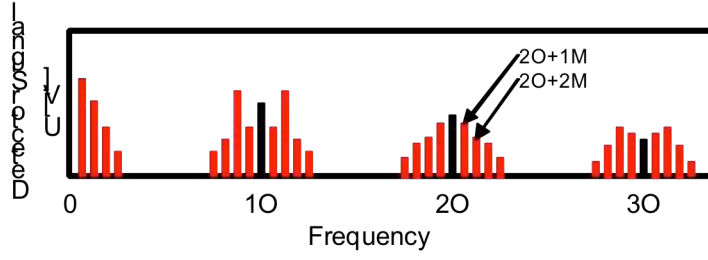


Figure 18: Frequency spectrum of the MCT detector signal when employing pseudoheterodyne interferometric detection with vibration of the tip at frequency Ω and phase modulation of the reference wave at frequency M .

with a high-speed data acquisition card and demodulated at frequencies $n\Omega + 1M$ and $n\Omega + 2M$. In the following, we describe how the tip-scattered near field is extracted from the tip-scattered light applying a pseudoheterodyne detection scheme.

In the transmission-mode s-SNOM shown in Figure 17, the MCT detector detects the coherent superposition of the reference beam E_{ref} with the scattered near fields E_{nf} and the background scattering E_{bkg} . Because the MCT detector is sensitive to the light intensity, these three contributions get mixed and the electric signal U of the MCT detector is given by

$$U \propto I_d = E_d E_d^* = (E_{\text{nf}} + E_{\text{bkg}} + E_{\text{ref}})(E_{\text{nf}} + E_{\text{bkg}} + E_{\text{ref}})^*, \quad (28)$$

where $(\dots)^*$ marks the complex conjugate. Because of the tip-oscillation at a frequency Ω and a nonlinear distance dependence of E_{nf} and E_{bkg} , the contributions E_{nf} and E_{bkg} yield higher harmonic content appearing at $n\Omega$ with $n = 1, 2, \dots$. As a result of the mixing with E_{ref} , side bands appear at frequencies $n\Omega + mM$ where m is an integer number and M is the frequency of the phase modulation of the reference beam. Thus the electric signal U of the detector yields a rich frequency spectrum, which is sketched in Figure 18. We mark the center frequencies $n\Omega$ in black color and the side bands $n\Omega + mM$ with red color.

The scattered near field E_{nf} and the background scattering E_{bkg} can be written in form of a Fourier series¹³⁰:

$$E_{\text{nf}} = \sum_{n=0}^{\infty} \sigma_{\text{nf},n} \cos(n\Omega t) E_{\text{inc}} , \quad (29)$$

$$E_{\text{bkg}} = \sum_{n=0}^{\infty} \sigma_{\text{bkg},n} \cos(n\Omega t) E_{\text{inc}} , \quad (30)$$

where $\sigma_{\text{nf},n}$, $\sigma_{\text{bkg},n}$ are the complex-valued Fourier expansion coefficients of the scattering coefficients σ_{nf} , σ_{bkg} defined in eqs. (24),(25) and Ω is the frequency of the tip oscillation. The terms in eq. (28) containing E_{nf} and E_{bkg} generate harmonics at $n\Omega$ in the detector signal U (black lines in Figure 18). The interference of the reference beam E_{ref} with the E_{nf} and E_{bkg} is reflected in eq. (28) by the products $E_{\text{nf}}E_{\text{ref}}^*$, $E_{\text{bkg}}E_{\text{ref}}^*$ and the corresponding complex conjugates. Only these terms contribute to the side bands at frequencies $f_{n,M} = n\Omega + mM$ in the frequency spectrum of the detector signal U (red lines in Figure 18). Note that the tip-scattered light E_{tip} yields the sum of the scattered near field E_{nf} and scattered background E_{bkg} according to $E_{\text{tip}} = E_{\text{nf}} + E_{\text{bkg}}$ (eq. (26)). Thus demodulating at $f_{n,M}$ yields the n-th Fourier coefficient of the tip-scattered light $\sigma_{\tau,n} = \sigma_{\text{nf},n} + \sigma_{\text{bkg},n}$.

In order to show how the amplitude and phase of the scattered near fields are obtained, we write

$$\begin{aligned} \sigma_{\text{nf},n} &= s_n e^{i\varphi_n} \\ \sigma_{\text{bkg},n} &= s_{\text{bkg},n} e^{i\varphi_{\text{bkg},n}} \\ \sigma_{\tau,n} &= \sigma_{\text{nf},n} + \sigma_{\text{bkg},n} = A_n e^{i\Phi_n} \end{aligned} \quad (31)$$

It can be shown that the n-th Fourier coefficient of tip-scattered light $\sigma_{\tau,n}$ can be extracted by analyzing the detector signal at the first and the second side band $U_{n,1} = U(f = n\Omega + 1M)$ and $U_{n,2} = U(f = n\Omega + 2M)$, respectively. For illustration, these are marked for $n = 2$ with black arrows in Figure 18. We also assume that the amplitude γ of the phase modulation in eq. (27) is set to $\gamma = 2.63$. Then, the tip-scattered light harmonics ($\sigma_{\text{nf},n} + \sigma_{\text{bkg},n}$) are obtained according to

$$\sigma_{\tau,n} = \sigma_{\text{nf},n} + \sigma_{\text{bkg},n} = 2.16k(U_{n,1} + iU_{n,2}), \quad (32)$$

where k is a complex-valued constant that depends on the adjustment of the interferometer. For details on this result, please refer to refs. ^{130,131}. In above equation, the background scattering $\sigma_{\text{bkg},n}$ can be suppressed when selecting a sufficiently high demodulation order n . This is because the near fields show a strong decay away from the surface. The tip, vibrating very close to the surface, thus strongly modulates the near field scattering E_{nf} , yielding significant values even in high harmonics $\sigma_{\text{nf},n}$. In contrast, most of the energy of the background scattering is located in the DC term and in low harmonics $\sigma_{\text{bkg},n}$ (ref. ¹³⁰). Therefore, for sufficiently high n , we can assume that $\sigma_{\tau,n} \approx \sigma_{\text{nf},n}$ and we can write the amplitude s_n and phase φ_n of the Fourier coefficient $\sigma_{\text{nf},n}$ of the scattered near fields as ¹³⁰

$$\begin{aligned} s_n &= 2.16k \sqrt{U_{n,1}^2 + U_{n,2}^2}, \\ \varphi_n &= \arctan\left(2.16k \frac{U_{n,2}}{U_{n,1}}\right). \end{aligned} \quad (33)$$

This is the measured signal in the transmission-mode s-SNOM with pseudoheterodyne detection. However, as we will see later in chapter 3.3, full background suppression at high n is not always possible and eq. (33) is not valid. In this case, the scattered background $\sigma_{\text{bkg},n}$ in $\sigma_{\tau,n} = \sigma_{\text{nf},n} + \sigma_{\text{bkg},n}$ cannot be neglected, and we thus describe the recorded signals by the amplitude A_n and phase Φ_n of $\sigma_{\tau,n}$:

$$\begin{aligned} A_n &= 2.16k \sqrt{U_{n,1}^2 + U_{n,2}^2}, \\ \Phi_n &= \arctan\left(2.16k \frac{U_{n,2}}{U_{n,1}}\right). \end{aligned} \quad (34)$$

3.3. Near-field mapping of metal IR nano-antennas and analysis of the image contrast

In a first experiment, we test the transmission mode s-SNOM by imaging well-defined gold nanorods on a Si substrate designed for fundamental dipolar resonance at mid-infrared frequencies. The rods were fabricated by electron-beam lithography and analyzed by far-field extinction spectroscopy by K. Crozier and coworkers in a previous work². The rods measure 1550 nm x 230 nm x 60 nm and were fabricated in arrays with an interrod spacing of 10 μm . A 5 nm chrome layer between the Au and Si serves as an adhesion layer. Far-field extinction spectroscopy was applied to characterize the nanorods in the mid-infrared spectral range. Figure 19 shows the far-field extinction spectrum for an array of these nanorods, revealing a fundamental dipolar resonance at $\lambda = 9.60 \mu\text{m}$. We note that because of the presence of the Si substrate, this resonance occurs at around $L \approx \lambda/6$ instead for the expected $L \approx \lambda/2$ for a nanorod in vacuum (see chapter 1.5.3).

Near-field imaging of the gold nanorods was performed with the CO₂ laser operating at a wavelength of 9.6 μm . The rods were illuminated from below with the polarization of the incident light being parallel to the rod's long axis. For background reduction, signal demodulation needs to be done at $n = 3$ because at $n = 4$, the signal is below the noise level. Because we do not know whether the background is fully suppressed for $n = 3$, we denote the demodulated signals by the amplitude A_3 and phase Φ_3 of the tip-scattered light $\sigma_{\tau,n}$ according to eq. (34). Figure 20 shows the topography and infrared near-field images of three individual nanorods recorded at their dipolar resonance wavelength. Due to the characteristics of our s-SNOM setup (i.e. the polarization of the reference beam is parallel to the tip), we expect the z-component of the near fields to be probed^{79,109,117} (see chapter 3.2). The expected dipolar pattern exhibits large near-field amplitude $|E_z|$ at the rod extremities and a 180° phase jump at the rod center (see the calculated near-field pattern in Figure 20a). In the experimental images, however (Figure 20b-d), the near-field maps of the rods show pronounced differences. The rods c and d exhibit significant near-field amplitude A_3 at the rod extremities, whereas the rod b exhibits a more intense near field at the left hand side. Furthermore, the near-field phase jump, which is

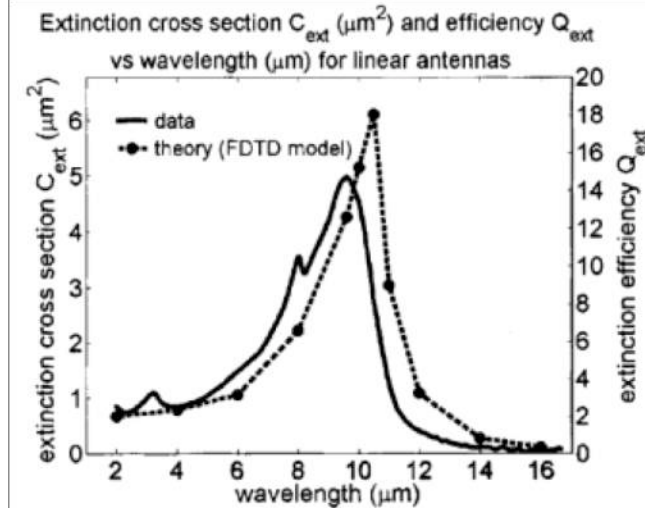


Figure 19: Experimental and FDTD-calculated extinction cross section σ_{ext} of 1.55 μm long gold nanorods in top of a Si substrate [taken from ref.²].

accompanied by a minimum in the amplitude image, appears at different positions for the three rods. The variation of the near field images allows us to conclude that we do not obtain exact maps of the dipolar near-field oscillation.

To analyze the differences in the near-field contrast of the three rods, we recorded approach curves (Figure 20e) at three different positions along the third rod (Figure 20d), which are marked by L, C, R in the topography image. At the two positions L and R we find a steep increase of the signal amplitude A_3 at tip-sample distances $z < 300 \text{ nm}$, which is a typical behavior for near-field signals¹³². At position C, no significant changes in the amplitude and phase signals are observed at small z , thus indicating that no near-fields are detected. At distances $z > 300 \text{ nm}$ (i.e. beyond the near-field zone of the antennas) the three approach curves exhibit significant optical signals. This reveals the presence of a residual background contribution $s_{\text{bkg},3}(z)$ and $\varphi_{\text{bkg},3}(z)$ in the detected s-SNOM signals A_3 and Φ_3 which is constant across the sample. Therefore, we can conclude that background contributions are not fully suppressed by signal demodulation at the higher harmonic $n = 3$ of the tip oscillation frequency Ω .

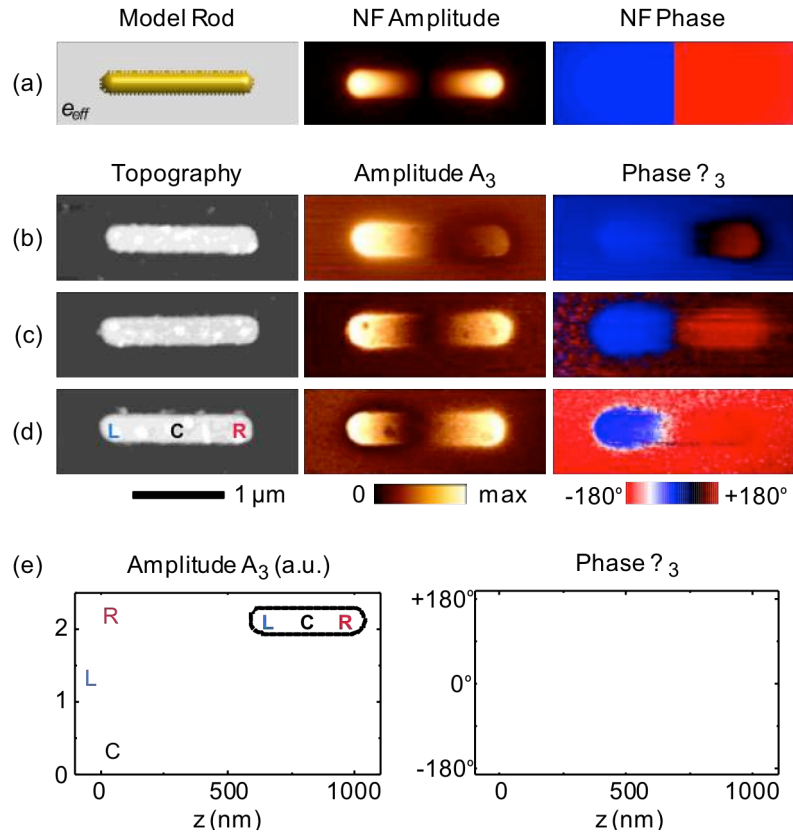


Figure 20: (a) Calculated z -component of the near fields of a resonant model rod. (b–d) Near-field modes of three individual nanorod antennas recorded at their fundamental dipolar resonance of $\lambda = 9.6 \mu\text{m}$ wavelength. The amplitude, A_3 , and phase, Φ_3 , signals are shown as recorded. The polarization of the incident light is chosen parallel to the rod axis. In the phase images, the left rod end was normalized to 0° . The differences in the near-field images are due to the presence of residual background. (e) Approach curves showing the amplitude and phase signal as a function of distance, z , between the oscillating tip and the antenna surface. The approach curves were taken at the positions L, C, and R of the third nanorod (d).

3.3.1. Procedure for the removal of residual background in near-field images

We now demonstrate that by subtracting the residual background contribution from s-SNOM images we can obtain reliable near-field maps of optical antenna structures. By a complex-valued subtraction, the background-free near-field amplitude $s_3(x, y)$ and phase $\varphi_3(x, y)$ can be obtained through

$$s_3(x, y) \cdot e^{i\varphi_3(x, y)} = A_3(x, y) \cdot e^{i\Phi_3(x, y)} - s_{\text{bkg},3}(z = 0) \cdot e^{i\varphi_{\text{bkg},3}(z=0)}, \quad (35)$$

where $A_3(x, y)$ and $\Phi_3(x, y)$ are the demodulated signals measured at the pixel position (x, y) . $s_{\text{bkg},3}(z = 0)$ and $\varphi_{\text{bkg},3}(z = 0)$ are the residual background amplitude and phase obtained in the absence of near fields from approach curve C in Figure 20e. The absence of a near-field increase for the approach curve taken at the center of the rod is in agreement with the assumption that the z-component of the rods' near field is probed (the calculated z-component at the rod center is zero). We note that such mathematical near-field extraction in s-SNOM experiments^{109,133} requires detection schemes where (i) amplitude and phase is mapped and (ii) where the demodulated detector signals are a linear, complex-valued sum of near-field and background contributions. Both requirements are fulfilled, for example, in heterodyne, pseudoheterodyne or phase shifting interferometric detection techniques^{109,130,133-135}.

In Figure 21b-d, we show the background-free near-field images of the three rods from Figure 20b-d. After the subtraction of residual background is applied, the optical images are uniform for the three rods. We observe high near-field amplitude values at the rod extremities in all cases now, whereas the rod center and the substrate show zero near-field amplitude. The phase-jump occurs at the exact center of the rod and measures 180° . Comparing the experimental background-free images with the numerical calculations, we obtain an excellent agreement with the calculated z-component of the near fields on top of the antenna (Figure 20a).

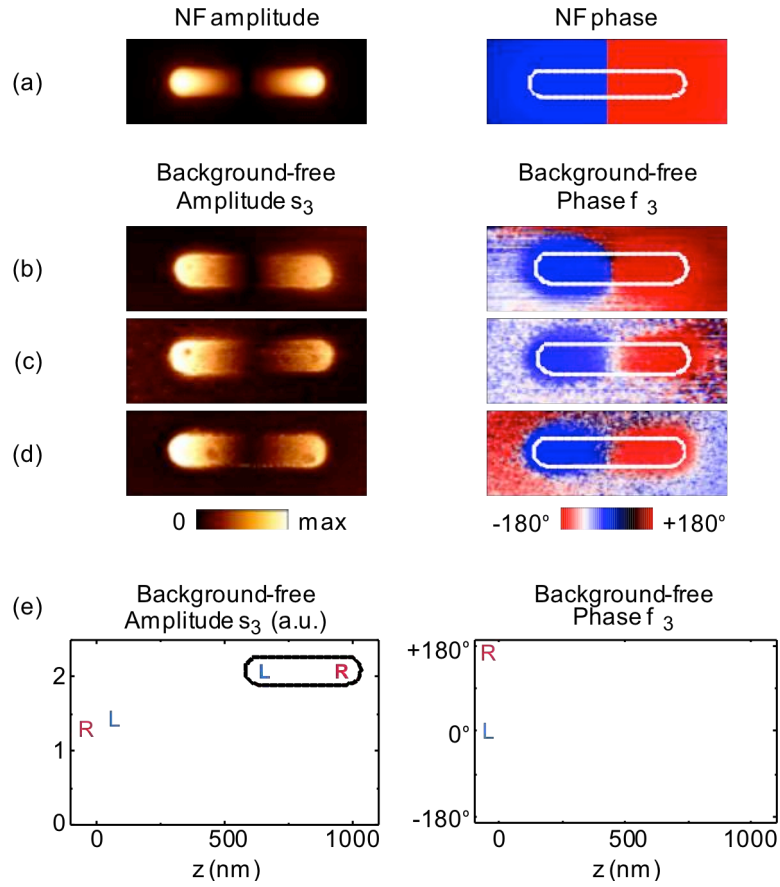


Figure 21: (a) Calculated z -component of the near fields of a resonant model rod. (b–d) Background-free amplitude and phase images of three nanorods. These images are obtained from Figure 20 after a complex-valued subtraction of residual background. The near-field patterns are exactly reproduced for the three antennas, showing the expected pattern for the fundamental dipolar oscillation mode. (e) Background-free approach curves at positions L and R on the third nanorod, obtained by complex-valued subtraction of residual background.

Complex-valued subtraction of the background contribution also yields background-free approach curves $s_3(z)$ and $\varphi_3(z)$ (Figure 21e). The approach curves at positions L and R in this case were obtained by complex-valued subtraction of curve C:

$$s_3(z) \cdot e^{i\varphi_3(z)} = A_3(z) \cdot e^{i\Phi_3(z)} - s_{\text{bkg},3}(z) \cdot e^{i\varphi_{\text{bkg},3}(z)}. \quad (36)$$

$A_3(z)$ and $\Phi_3(z)$ are the s-SNOM signals recorded for the approach curves at positions L and R, whereas the residual background $s_{\text{bkg},3}(z)$ and $\varphi_{\text{bkg},3}(z)$ is given by the

approach curve taken at the rod center C, a position chosen because there the z -component of the near field is zero (see black curves in Figure 20e). As expected, we observe an increase of the amplitude signal $s_3(z)$ when the tip approaches the antenna positions L and R (decreasing z). Most importantly, the phase signal $\varphi_3(z)$ is nearly constant during approach. At a fixed illumination frequency close to resonance (as in our experiment), any resonance shift due to tip-sample interaction would induce a significant change of phase. This, however, is not observed in Figure 21e. Thus, we can exclude tip-induced distortions of the antenna modes. Note that for strong near-field coupling between tip and antenna, we would expect spectral shifts of the antenna resonance with decreasing distance z , analogous to near-field coupling of plasmon-resonant nanoparticles^{126,136-141}.

3.3.2. Near-field mapping of extended 2D antenna structures

In Figure 22, we compare the background-free experimental near-field images with numerical calculations (boundary element method, BEM^{12,13}) of a model system consisting of a 1.55 μm -long gold nanorod of 230 nm diameter. The calculations were performed by A. Garcia-Etxarri at J. Aizpurua's group at the Centro de Fisica de Materiales (CSIC-UPV/EHU) and Donostia International Physics Center (DIPC) in San Sebastian. To take into account the experimental situation in which the nanorod is situated on top of a silicon substrate with air above, the model nanorod is embedded in an effective medium of dielectric value $\epsilon_{\text{eff}} = 6.34$ (see chapter 1.5.3). This value is chosen such that the nanorod is resonant at 9.6 μm wavelength. The x - and the z -components of the calculated near-field amplitude and phase are shown in Figure 22b. In comparison with the experimental images of the nanorod (Figure 22a), we find clear evidence that our s-SNOM probes the z -component of the near-field distribution. This behavior can be explained by the polarization of the reference beam, which is chosen parallel to the tip axis (see arrows in Figure 17). The good agreement between experiment and calculation further confirms negligible mode distortion by the probing tip, which makes s-SNOM

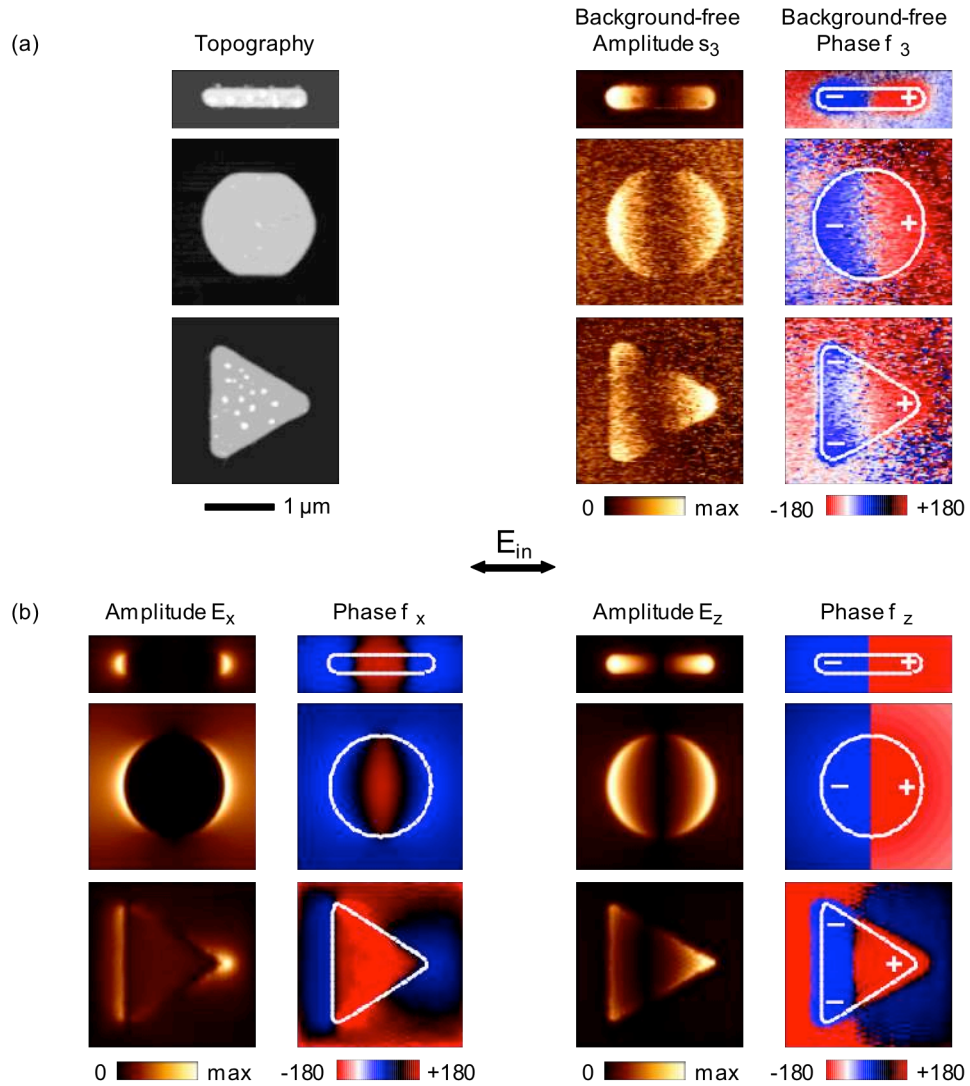


Figure 22: (a) Topography and experimental background-free near-field images of a rod, disk and triangle antenna excited close to their fundamental dipolar resonance at $\lambda = 9.6 \mu\text{m}$ wavelength. (b) Numerically calculated near-field distribution of a model rod, disk, and triangle antenna with the same dimensions as in the experiment. The maps show the x- and z-components of the electric field at a height of 51 nm above the rod surface. The boundary element method (BEM^{12,13}) was applied to model the rod and the disk, assuming an effective medium of $\epsilon_{\text{eff}} = 6.34$ to match the resonance of the experimental antennas and to take account of the Si substrate. The triangle antennas were modeled using the Lanczos pseudospectral method combined with the Lippmann–Schwinger approach¹⁴. The calculation of the triangle accounts explicitly for the presence of the Si substrate.

a powerful tool for characterizing and identifying antenna near-field modes in amplitude and phase.

In Figure 22, we also demonstrate the general applicability of transmission-mode s-SNOM and the residual background subtraction for reliable near-field mapping of extended two-dimensional antenna structures. We image disks (1700 nm diameter x 60 nm height) and equilateral triangles (1560 nm long axis x 60 nm height), which were fabricated on a Si-substrate by e-beam lithography. These infrared antennas exhibit a far-field resonance at a wavelength of about $\lambda = 10.1\mu\text{m}$ (ref. ²). Near-field imaging was performed close to the resonance at $\lambda = 9.6\mu\text{m}$. Residual background contributions were subtracted according to eq. (36) described above. We note that the signal-to-noise ratio is better in the near-field images of the rod. We assign this to the fact that the rod was measured on resonance, whereas the disk and triangle were measured slightly off-resonance. Furthermore, the near-field images of the rod were recorded with a higher pixel resolution and with reduced scanning speed. The background-free near-field images (Figure 22a) show again an excellent agreement with the z-component of the calculated near-field distribution (Figure 22b). For the triangle, we find in both the experimental and the calculated map a higher amplitude signal s_3 at the tip than at the base of the triangle, which can be explained by the strong field concentration at the tip. As for the rod and disk, the near-fields at the tip and base of the triangle oscillate out of phase at about 180° . In contrast to the rods and disks, the phase jump on the triangle - accompanied by a minimum in the near-field amplitude - does not occur exactly in the center of the antenna but is slightly shifted toward the base of the triangle. We note that the experimental verification of such detailed near-field information is possible only by obtaining background-free near-field maps, as described here.

3.3.3. Improved s-SNOM mapping with complete suppression of residual background

In the course of this thesis, we found out that the complete suppression of background contributions can be achieved during the near-field mapping of plasmonic structures. In this case, a post-processing of the s-SNOM images in form of the procedure described in chapter 3.3.1 is not necessary anymore. This finding can be related to slight modifications to the transmission-mode interferometer setup, a better alignment of the s-SNOM setup and to the improved capabilities of the s-SNOM operator. To demonstrate that s-SNOM near-field mapping with a full suppression of residual background contributions is possible, we show the near-field distribution of a complex structure consisting of seven disks arranged in the heptamer configuration (Figure 23). The experimental near-field distribution (z-component) shows the typical dipolar pattern on all seven disks and is in excellent agreement with numerical calculations¹¹.

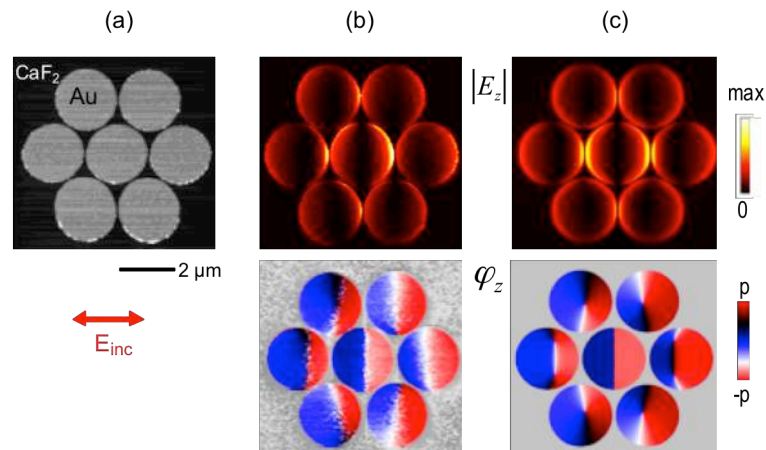


Figure 23: Near-field imaging of a heptamer structure on top of a CaF₂ substrate with transmission-mode s-SNOM, where background contributions are fully suppressed in the experiment and a subsequent removal of residual background is not necessary. (a) Topography. (b) Experimental near-field maps showing the amplitude $|E_z|$ and phase φ_z . Imaging has been performed at a wavelength of 9.3 μm. (c) Numerical calculation of the near-field distribution. For details see ref. ¹¹.

3.4. Conclusions

We demonstrated that transmission-mode s-SNOM employing pseudoheterodyne detection, uncoated silicon tips and complex-valued subtraction of residual background enables reliable near-field mapping of infrared antenna modes in both amplitude and phase. The presented near-field images of infrared-resonant rods, disks and triangles show an excellent agreement with the calculated mode pattern and provide clear evidence that the z-component of the near-field distribution is measured. From the good agreement between experiment and theory, we can exclude mode distortion by the probing tip. This conclusion is further supported by approach curves showing that the near-field phase is independent of the probe-sample distance. Background- and distortion-free experimental near-field images promise reliable and quantitative near-field characterization of complex optical antenna structures, which can be used as hosts in molecular spectroscopy, transmitters in optical communication and nanodevices for energy-transfer.

4. Phase-Resolved Mapping of the Near-Field Vector and Polarization State in Nanoscale Antenna Gaps

We demonstrate that the local near-field vector and polarization state on planar antenna structures and in nanoscale antenna gaps can be determined by scattering-type near-field optical microscopy (s-SNOM). The near-field vector is reconstructed from the amplitude and phase images of the in- and out-of-plane near-field components obtained by polarization-resolved interferometric detection. Experiments with a mid-infrared bowtie aperture antenna yield a vectorial near-field distribution with unprecedented resolution of about 10 nm and in excellent agreement with numerical simulations. Furthermore, we provide first direct experimental evidence that the nanoscale confined and strongly enhanced fields at the antenna gap are linearly polarized. s-SNOM vector-field mapping paves the way to a full near-field characterization of nanophotonic structures in the broad spectral range between visible and terahertz frequencies, which is essential for future development and quality control of metamaterials, optical sensors, and waveguides.

4.1. 3D Polarization state of near fields

The polarization of light is usually described by the orientation of the electric field. For a three-dimensional plane wave with wave vector $\mathbf{k} = (0,0,k)$ we can write the electric field at position $r = (r_1, r_2, r_3)$ as

$$\mathbf{E}(\mathbf{r}) = \begin{pmatrix} a_1 e^{i(kr - \omega t + \delta_1)} \\ a_2 e^{i(kr - \omega t + \delta_2)} \\ 0 \end{pmatrix} \quad (37)$$

where a_1, a_2 are the amplitude and δ_1, δ_2 are the phase values of the individual components^{142,143}. The phase difference $\delta = \delta_1 - \delta_2$ between the components determines the polarization of the plane wave where a phase difference of $\delta = 0^\circ$ or 180° defines linearly polarized light, while $\delta = \pm 90^\circ$ and $a_1 = a_2$ yields circularly polarized light (Figure 24a-c). In comparison to free-space propagating light, optical near fields are usually more complicated. Generally, the local near field at a sample surface is described by a three-dimensional vector $\mathbf{E} = (E_x, E_y, E_z)$, where each near-field component E_j is characterized by both a field amplitude $|E_j|$ and a phase φ_j ^{143,144}. While strong field amplitudes at specific sample locations open new avenues for example in vibrational spectroscopy of single molecules¹⁹⁻²¹, it is the phase distribution that is essential for nanoscale coherent control applications^{80,81,87}. The phase difference $\delta_{ij} = \varphi_j - \varphi_i$ between individual components is thereby a fundamental quantity as it determines the polarization state of the vector near field¹⁴³. For example, a phase difference of $\delta_{ij} = 0^\circ$ or 180° (for all i, j) defines linearly polarized local fields (Figure 24d), while $\delta_{ij} = \pm 90^\circ$ and $|E_i| = |E_j|$ yields circularly polarized near fields. In the most general case, the endpoint of the field vector traces out an ellipse¹⁴³ (Figure 24e). Engineering of the individual phases thus can be applied to control¹⁴⁵ the near field polarization state for novel nanophotonic applications in, e.g., quantum optics¹⁴⁶ or solid state physics^{147,148}. To this end, it is of utmost importance to develop tools that allow for ultrahigh resolution mapping of individual near-field components in both amplitude and phase.

4.1 3D Polarization state of near fields

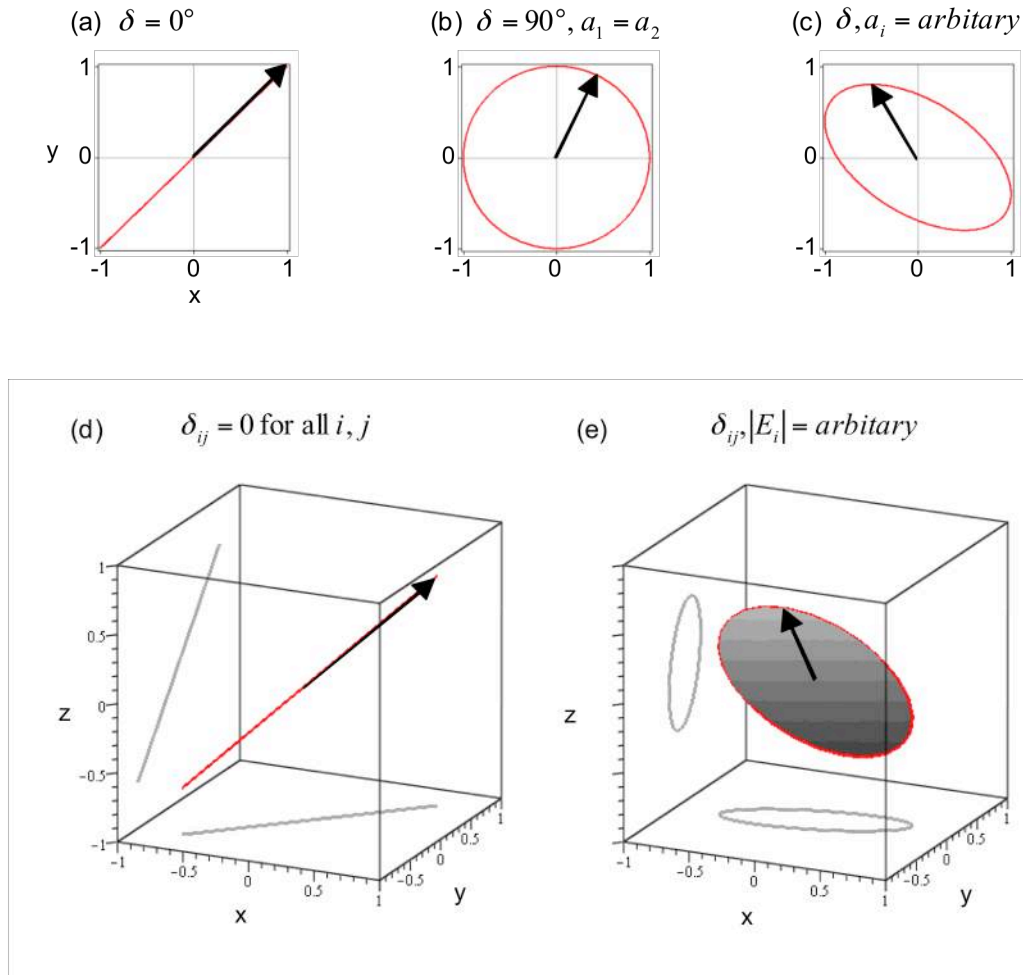


Figure 24: Top: Polarization states of optical far fields where the condition (a) yields linearly polarized, (b) circularly polarized light and (c) describes the general case of elliptically polarized light. **Bottom:** Three-dimensional polarization state of optical near fields where (d) illustrates linearly polarized near fields, (e) elliptically polarized near fields. The red lines designate the trace of the endpoint of the electric field vector over the oscillation period $T = 2\pi/\omega$, the black arrows designate the momentary electric field vector for a given time t .

A variety of methods such as interferometric scanning near-field optical microscopy (SNOM)^{72,79,109,112,113,116,117}, scattering-type SNOM (s-SNOM)^{52,79,108-115}, two-photon induced luminescence (TPL) microscopy^{55,60,81}, electron energy loss spectroscopy (EELS)⁸⁶ and photoemission electron microscopy (PEEM)⁸⁷ enable the mapping of near-fields distributions and thus have provided valuable insights into plasmonic antenna and waveguide structures (see chapter 3.1 for a short introduction on these techniques). Each of these methods relies on an individual physical approach to probe the near fields, however, each of them is confronted with specific limitations. For example, TPL microscopy is based on an incoherent measurement principle and thus does not provide phase information. With aperture SNOM typically the transverse electric near-field components (parallel to the sample surface) are probed while scattering-type SNOM is considered to be mostly sensitive to the vertical near-field component (perpendicular to the sample surface). Indeed, several phase- and polarization-sensitive s-SNOM studies^{79,109,112} report amplitude and phase images of only the out-of-plane near-field component. A recent study¹¹³, however, shows that amplitude and phase of both components can be measured with elongated tips, but the vector field was not reconstructed because of the unknown scattering characteristic of the tip. Vector field microscopy based on polarization-resolved intensity detection of light scattered from metal particle and aperture tips has been reported recently¹⁴⁹. Because of non-interferometric detection, however, essential phase information is lost with such a technique, and thus the polarization state could not be fully characterized.

In this chapter, we demonstrate nanoscale resolved imaging of near-field vector components with the use of our transmission-mode s-SNOM presented in chapter 3.2, employing a dielectric tip as scattering probe. By analyzing the tip-scattered light with a linear polarizer, we map the amplitude *and* phase of the in-plane (transverse) and out-of-plane (vertical) component of nanoscale confined fields at the gap of an infrared antenna. After characterizing the scattering tensor of the tip, we succeed to reconstruct for the first time the local polarization state of antenna near fields. Our results provide direct experimental evidence that the gap fields are linearly polarized.

4.2. Polarization- and phase-resolved s-SNOM mapping

We demonstrate polarization- and phase-resolved near-field mapping with an inverse bowtie antenna (bowtie aperture)^{22,150} which was designed to exhibit a dipolar resonance in the mid-infrared region at a wavelength of about 9 μm (Figure 25a). The topography of the antenna is depicted in Figure 25b, showing the two triangular holes that were milled by focused ion beam (FIB) into a 40 nm thick Au film evaporated on a Si substrate. The gap of the inverse bowtie antenna has a width of approximately 80 nm. The bowtie antenna was fabricated by J. Alkorta at the Centre of Studies and Technical Research of Gipuzkoa (CEIT) and TECNUN (University of Navarra, San Sebastian).

Distortion-free imaging of the antenna near fields was performed with our transmission-mode s-SNOM^{109,110} (chapter 3.2), employing the sharp dielectric tip of conventional silicon cantilevers (Nanosensors, PPP-RT-NCHR). The antenna is illuminated from below at a wavelength of $\lambda = 9.3 \mu\text{m}$. Note that in contrast to normal bowtie antennas, the polarization of the incident field has to be chosen perpendicular to the long axis for resonant excitation (Babinet's principle^{144,151}), i.e., parallel to the x-axis (see Figure 25a). The tip-scattered light is analyzed by passing it through the polarizer P1 and detected with an interferometer. The polarization of the reference arm of the interferometer is fixed to $+45^\circ$ in all experiments by means of the polarizer P2 (see schematic of the transmission-mode s-SNOM in Figure 17 on page 58). Suppression of background light is achieved by vertical tip oscillation (about 100 nm amplitude) at the cantilever's mechanical resonance frequency $\Omega = 300 \text{ kHz}$ and demodulation of the detector signal at higher harmonics 3Ω . A pseudoheterodyne interferometric detection technique¹³⁰ (www.neaspec.com) yields the near-field optical amplitude $|E|$ and phase φ simultaneously^{109,110}. Note that for better reading and consistency with the related publication¹⁵², in this chapter we use the symbols $|E|$ and φ in order to refer to the amplitude s_3 and phase φ_3 of the Fourier coefficient $\sigma_{\text{nf},3}$ of the scattered near fields as defined in eq. (33).

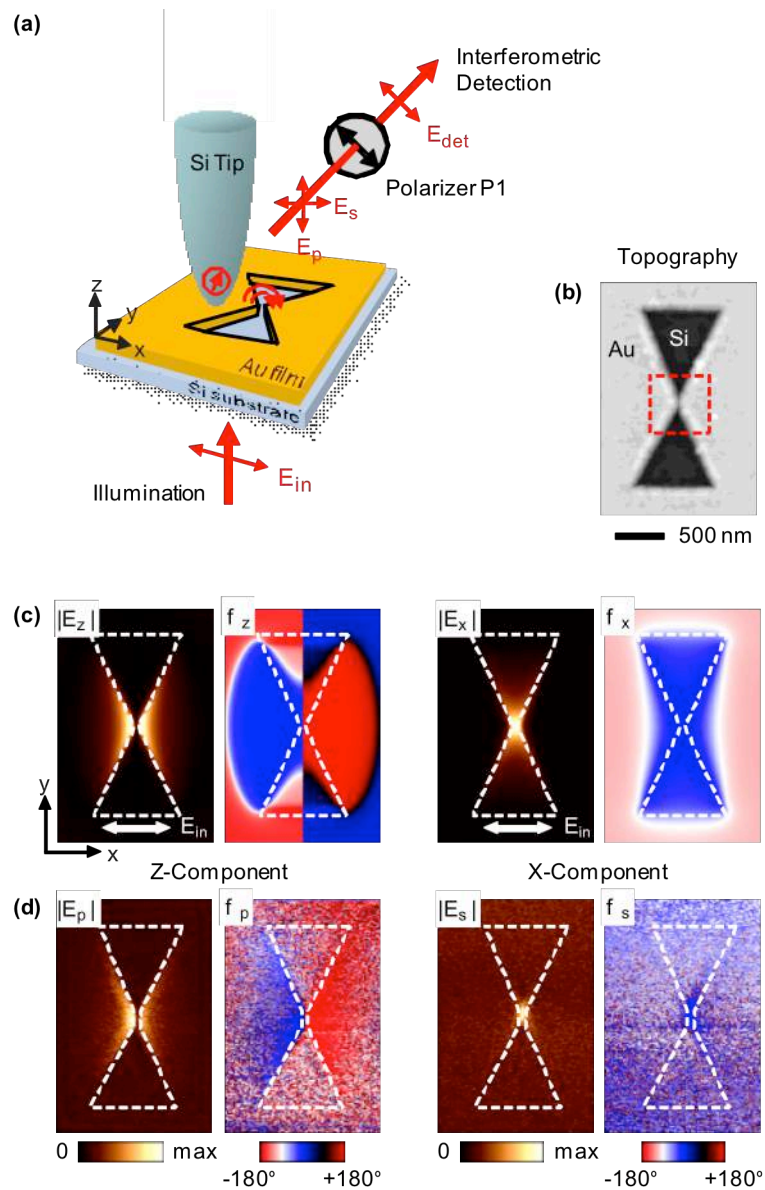


Figure 25: Near-field vector mapping of an inverse bowtie antenna. **(a)** Sketch of the experimental setup showing a silicon tip scattering the local fields of an inverse bowtie antenna. **(b)** Topography image of the inverse bowtie antenna (1600 nm length \times 800 nm base \times 40 nm thickness). **(c)** Numerically calculated near-field distribution of the inverse bowtie antenna, showing amplitude and phase of the z- and the x-component of the electric field 30 nm above the Au surface at $\lambda = 9.3 \mu\text{m}$. **(d)** Experimental near-field images (raw data) of the inverse bowtie antenna recorded at $\lambda = 9.3 \mu\text{m}$. Vertical polarizer setting detects the p-polarized light and yields the near-field amplitude $|E_p|$ and phase φ_p . Likewise, a horizontal polarizer setting detects the s-polarized light and yields the near-field amplitude $|E_s|$ and phase φ_s . The phases φ_s and φ_p were arbitrarily set to 0° at the gap center. The phase difference between s- and p-polarization was determined by line scans across the gap where both polarizations were measured with a constant reference phase (Figure 27b).

In Figure 25d we demonstrate that polarization- and phase-resolved s-SNOM enables the mapping of amplitude and phase distribution of individual near-field components. We show the experimental near-field images of the bowtie antenna obtained for a vertical and horizontal orientation of the polarizer, corresponding to the detection of the p- and s-polarized tip-scattered light, respectively. Detecting the p-component, we observe high-amplitude signals $|E_p|$ on top of the metal film near the rim and particularly at the two edges forming the gap. Inside the gap no amplitude signal is observed but instead a phase jump of exactly 180° (as already observed with IR gap antennas¹⁰⁹). By rotating the polarizer to a horizontal orientation, we select the s-component of the tip-scattered light. We can immediately see that the amplitude image $|E_s|$ exhibits a completely different pattern (right-hand side of Figure 25d), featuring a highly localized, intense spot inside the gap and a spatially constant phase. To analyze the near-field contrast in our images, we performed FDTD calculations (www.lumerical.com, FDTD solutions) of the fields of a bowtie aperture antenna on top of a Si substrate. Figure 25c shows the amplitude and phase of the near field components E_z and E_x calculated at a height of 30 nm. The experimental images ($|E_p|$, φ_p) and ($|E_s|$, φ_s) are in excellent agreement with the z- and x-components of the calculated near-field distribution, respectively. We conclude that by selecting the p-polarized scattered field (vertical polarizer setting), the signal amplitude $|E_p|$ yields the out-of-plane field $|E_z|$. The signal phase φ_p yields φ_z . Analogously, we map $|E_x|$ and φ_x by a horizontal polarizer setting (s-polarized). Remarkably, the spot size observed in the s-polarized image is about 50 nm (FWHM), providing direct experimental evidence that gap antennas generate in-plane fields of extreme subwavelength scale confinement ($\lambda/200$).

For further insights into the nature of the gap fields, we imaged the gap region at higher spatial resolution and with different polarizer angles β . The topography image of the gap region is shown in Figure 26a. The high-resolution near-field images in Figure 26c taken at the polarizer angles of $\beta = 90^\circ$ and 0° (corresponding to the detection of p- and s-polarizer light, respectively) clearly reproduce our results from Figure 25. Rotating the polarizer clockwise from 90° toward 0° , interestingly, we observe asymmetric near-field patterns. While the amplitude signals at the right side of the gap become increasing extinguished, the localized spot on the left rim of the gap continuously moves toward the gap center. This observation can be understood with a sketch of our experimental configuration (Figure 26b), showing a cross section of the gap with electric field lines

and the polarization-resolved near-field detection scheme. Clearly, the amplitude images taken at arbitrary polarizer angles β highlight the antenna regions where the near fields point in the direction of β . We note that the experimental images show a much stronger field confinement at the gap center which can be explained by the fact that the tip follows the surface topography. Our results unambiguously show the capability of s-SNOM with standard Si tips to map the vectorial nature of nanoscale antenna fields.

4.3. Reconstruction of the vectorial near-field distribution and polarization state

From our experimental results in Figure 25 we can conclude that the transfer of the antenna near field $\mathbf{E} = (E_x, E_y, E_z)$ into the s-SNOM signal (E_s, E_p) can be described in Cartesian coordinates by a diagonal tensor $\boldsymbol{\sigma}$:

$$\begin{pmatrix} E_s \\ E_p \end{pmatrix} \propto \begin{pmatrix} \sigma_s & 0 \\ 0 & \sigma_p \end{pmatrix} \begin{pmatrix} |E_x| e^{i\varphi_x} \\ |E_z| e^{i\varphi_z} \end{pmatrix}. \quad (38)$$

The tensor $\boldsymbol{\sigma}$ essentially describes the scattering characteristics of the probing tip. E_s and E_p are the complex-valued signals that are measured when selecting the s- and p-polarized components of the tip-scattered light with the use of the polarizer P. $E_{x,z}$ are the local antenna near fields in x- and in z-directions expressed by their amplitudes $|E_{x,z}|$ and phases $\varphi_{x,z}$. We note that generally the tensor $\boldsymbol{\sigma}$ connects the three-dimensional near-field vector (E_x, E_y, E_z) with the two-dimensional far-field vector (E_s, E_p) . Due to the symmetry of the bowtie antenna, however, we can neglect the y-component of the electric field. Numerical calculations confirm that $E_y \ll E_{x,z}$. We test eq. (38) by a numerical simulation of the experimental image series shown in Figure 26d. We calculate the recorded near-field amplitude and phase images, E_{det} and φ_{det} ,

4.3 Reconstruction of the vectorial near-field distribution and polarization state

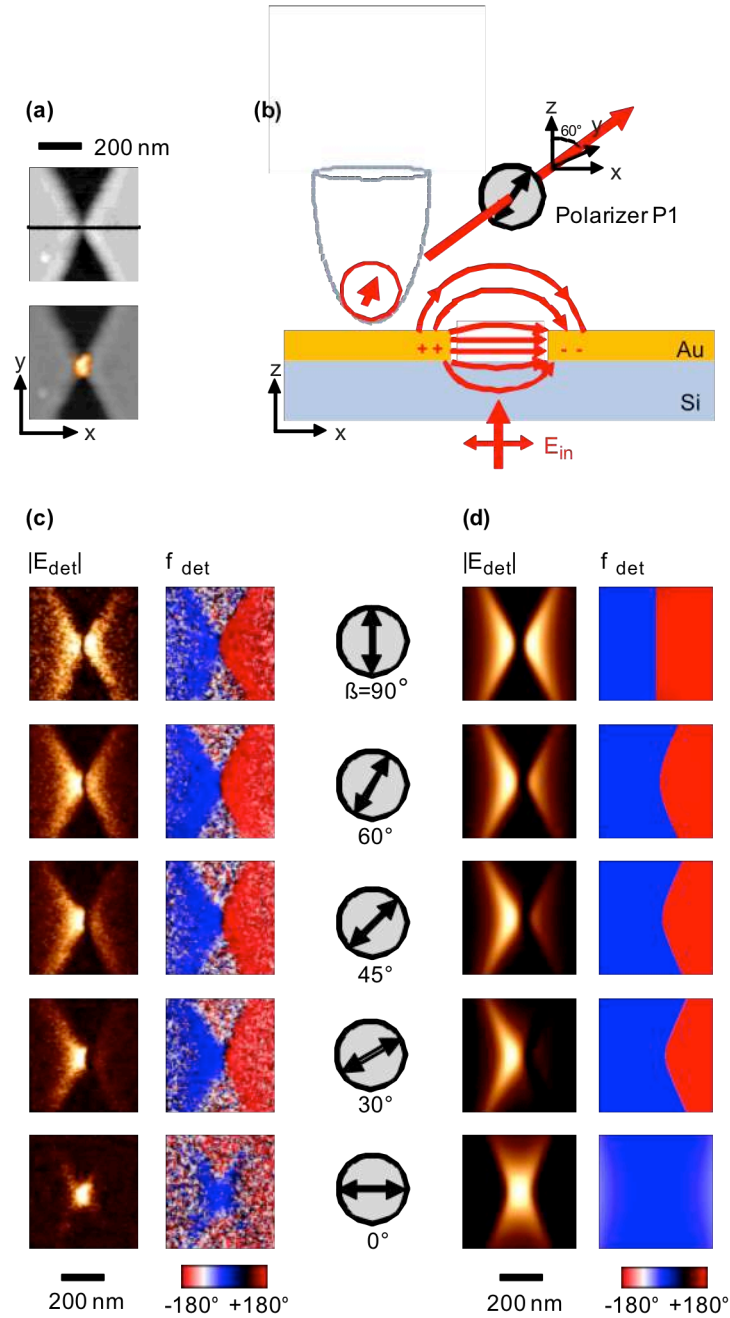


Figure 26: Polarization-resolved near-field study of the gap region. **(a)** Top: Topography image of the gap region marked by the red dashed square in Figure 25b. Bottom: Superposition of the near-field amplitude image $|E_s|$ on top of the topography image. **(b)** Illustration of the experiment, showing the cross section of the gap region. Polarization-resolved near-field detection is performed by analyzing the tip-scattered light with the polarizer P. **(c)** Experimental nearfield images of the gap region, recorded at different polarizer angles β between 90° and 0° . **(d)** Calculated near-field images E_{det} based on eq. (39) for the different polarizer angles β , using the calculated near-field distribution of Figure 25c and relative tensor components $2\sigma_s = \sigma_p$.

according to

$$|E_{\text{det}}|e^{i\varphi_{\text{det}}} \propto \sigma_s |E_x| e^{i\varphi_x} \cdot \cos \beta + \sigma_p |E_z| e^{i\varphi_z} \cdot \sin \beta \quad (39)$$

where $|E_x|$, $|E_z|$, φ_x and φ_z are the calculated near field amplitude and phase of the x - and z -component shown in Figure 25c. We find a good agreement between experiment and calculations when taking $2\sigma_s = \sigma_p$. The result of this calculation is shown in Figure 26d. We explain the anisotropy of tensor σ by the elongated shape of Si tip. Note that the tensor components σ_s and σ_p are found to be real-valued numbers. Thus, no phase shift is introduced by the tensor σ when the near-field components are transferred to the far-field signals E_s and E_p . We explain the real-valued tensor components by the dielectric (non-resonant) material properties of the Si tip.

In the following we demonstrate that knowledge of the tensor σ allows for reconstruction of the vectorial near-field distribution and the polarization state of the gap fields. In Figure 27b we plot amplitude and phase of the x - and z -component of the gap fields across the gap center according to

$$\begin{pmatrix} |E_x| e^{i\varphi_x} \\ |E_z| e^{i\varphi_z} \end{pmatrix} = \frac{1}{\sigma_s^{-1} |E_s(0)|} \cdot \begin{pmatrix} \sigma_s^{-1} |E_s| e^{i\varphi_s} \\ \sigma_p^{-1} |E_p| e^{i\varphi_p} \end{pmatrix} \quad (40)$$

with $2\sigma_s = \sigma_p$. The experimental values for (E_s, φ_s) and (E_p, φ_p) have been extracted from line scans across the antenna gap (along the dashed line in Figure 26a) for the polarizer angles $\beta = 0^\circ$ and $\beta = +90^\circ$. It is important to note that the reference phase in this experiment is constant for both polarizer settings, thus yielding the phase difference between the individual polarizations. We also note that in this experiment the measured signals are not referenced to the incident field. Thus, we measure the ratio between the field components rather than the field enhancement compared to the incident field. For comparison, we show in Figure 27c the numerically calculated near-field components (normalized to $|E_x(0)|$) along the dashed line in Figure 27a, thus taking into account that the tip follows the surface topography. In both experiment and calculations we observe strong in-plane field amplitudes inside the gap ($x = 0$) which exceed the maximum out-of-plane fields by a factor of about 2.5. Remarkably, also the double-peak structure of

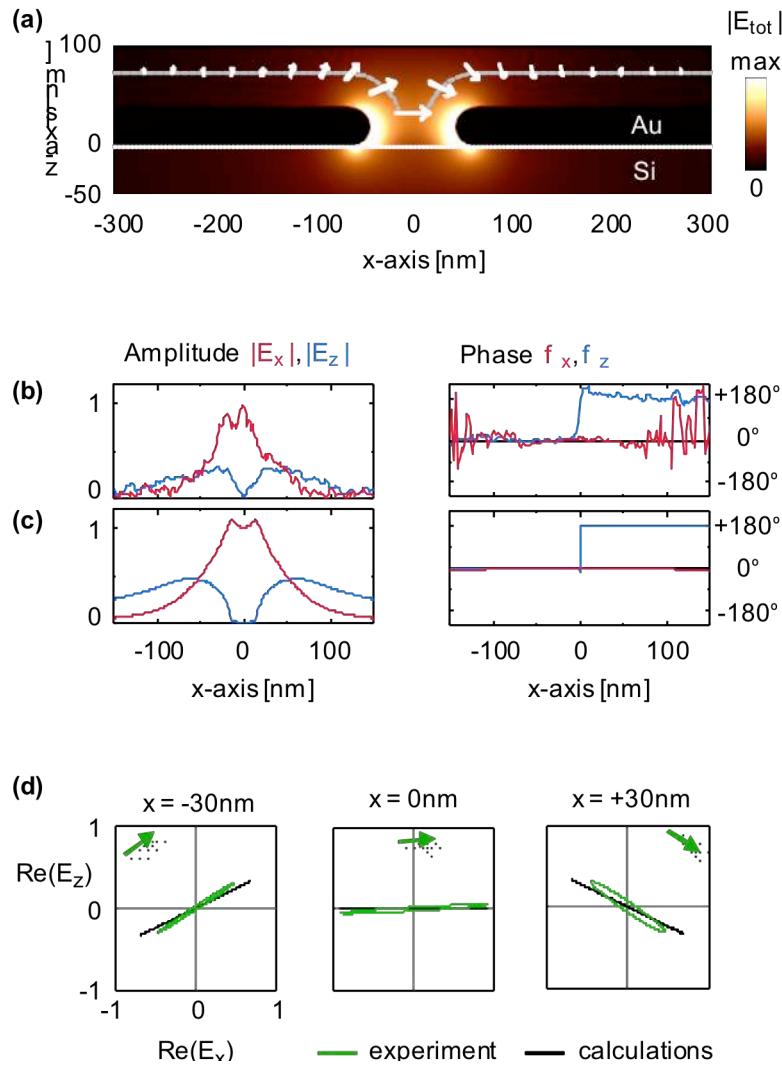


Figure 27: Characterization of the near-field polarization state at the antenna gap. **(a)** Cross section of the antenna gap showing the numerically calculated total electric field $|E_{tot}|$. The direction of the local fields (white arrows) is plotted along the height contour that the tip follows in the experiment (dashed line). **(b)** Experimental amplitude and phase of the in-plane ($|E_x|$, φ_x) and out-of-plane ($|E_z|$, φ_z) near-field components across the antenna gap reconstructed with eq. (40) from experimental line scans (along the black dashed line in Figure 26a). A spatially constant phase shift (equal for both components) has been added to the phase data φ_x and φ_z in order to obtain absolute phase agreement with the numerical calculation. **(c)** Calculated amplitude and phase of the in-plane ($|E_x|$, φ_x) and out-of-plane ($|E_z|$, φ_z) components of the near field along the dashed line shown in (a). The phase φ_x was set to 0° at the gap center. **(d)** Polarization state of the near fields at positions $x = -30$, 0 , and 30 nm obtained from eq. (41). The green line displays the polarization state obtained from the experimental near-field components shown in (b). The black lines display the polarization state obtained from the numerically calculated near-field components shown in (c). The green arrows indicate the instantaneous orientation of the experimental near field at time $t = 0$.

the x component inside the gap can be visualized with a resolution of about 10 nm. It reveals that the infrared fields are not localized in the center of the gap but rather at the two metal edges, as also predicted by the numerical calculations in Figure 27a. The phase measurement (right-hand side of Figure 27b) reveals a phase difference between the x and z components amounting to $\delta_{xz} = \varphi_z - \varphi_x \approx 180^\circ$ for $x > 0$ and $\delta_{xz} \approx 0^\circ$ for $x < 0$.

The polarization state of an optical field can generally be visualized by a parametric plot of the electric field vector $E(t)$ as a function of time t

$$E(t) = Re \left(\begin{array}{l} |E_x| e^{i(-\omega t + \varphi_x)} \\ |E_z| e^{i(-\omega t + \varphi_z)} \end{array} \right), \quad (41)$$

where ω is the angular light frequency¹⁴⁴. In Figure 27d we display the polarization state of the antenna gap fields at the positions $x = -30, 0$ and $+30$ nm using the experimental and numerically calculated near-field amplitude and phase values taken from Figure 26b,c. The experimental plots (green curves) yield strongly elliptical (nearly linear) trajectories, providing direct evidence of linearly polarized near fields. This finding is confirmed by plots of the numerically calculated electric field vector (black lines), which show a perfect linear polarization state of the gap fields. We note that the slight discrepancy between experiment and calculation is due to experimental uncertainties in the phase measurement. Furthermore, we can measure the local field direction. While inside the gap ($x = 0$ nm) the fields are horizontally oriented, we find a field orientation of about $\pm 30^\circ$ at positions $x = \pm 30$ nm relative to the sample surface.

We note that all three components of antenna vector fields could be measured by a rotation of the sample and of the polarization of the incident light. Because of the transmission-mode setup, the antenna illumination and thus the near-field distribution are unaffected by such rotation. This is an essential advantage compared to s-SNOM with side illumination^{79,112,117} where the antenna illumination is dependent on the sample orientation. However, in the case of structures with two non-negligible in-plane components, a mixture of in- and out-of-plane components will be measured with the present experimental setup (detection of the tip-scattered light at an angle of 30° relative

to the sample surface). Thus a more sophisticated image analysis or a modification of the present setup is required, allowing for the separation of the individual near-field components. For example, mixing of the components could be avoided by detection of the tip-scattered light at small angles relative to the sample surface.

4.4. Conclusions

In conclusion, we succeeded to map the in- and out-of-plane components of the vector field of an IR antenna by employing standard dielectric atomic force microscopy tips as scattering-type near-field probes. In contrast to nanoparticle tips¹⁴⁹ – with typical diameters of about 100 nm – we are able to access and probe the fields inside narrow antenna gaps with nanometer resolution. Because generally the phase can vary considerably across nanoantennas¹⁰⁹, the separated acquisition of near-field amplitude *and* phase is a requirement for a full and reliable characterization of the polarization state of local near fields. Phase-resolved vector-field mapping thus paves the way to a complete characterization of nanophotonic structures, analogous to a vector analyzer at radio frequencies, which will play an important role for future engineering of metamaterials, optical sensors and waveguides operating at visible, infrared, and terahertz frequencies.

5. Bridging the Gap: Controlling the Near-field Oscillations of Loaded Plasmonic Nanoantennas

Optical and infrared antennas^{2,16,27,55,69,70} enable a variety of cutting-edge applications ranging from nanoscale photodetectors¹⁷ to highly sensitive biosensors²¹. All these applications critically rely on the optical near-field interaction between the antenna and its 'load' (biomolecules or semiconductors). However, it is largely unexplored how antenna loading affects the near-field response. Here, we use scattering-type near-field microscopy to monitor the evolution of the near-field oscillations of infrared gap antennas progressively loaded with metallic bridges of varying size. Our results provide direct experimental evidence that the local near-field amplitude and phase can be controlled by antenna loading, in excellent agreement with numerical calculations. Modeling the antenna loads as nanocapacitors and nanoinductors^{9,73,76}, we show that the change of near-field patterns induced by the load can be understood within the framework of circuit theory. Targeted antenna loading provides an excellent means for engineering complex antenna configurations in coherent control applications⁸⁰, adaptive nanooptics⁸⁷ and metamaterials¹⁵³.

5.1. Introduction

In chapter 1.5.4, we described the structure of an efficient optical antenna that consists of two adjacent metallic segments (i.e. nanorods) separated by a nanoscopic gap (gap antenna). With this structure, the near-field coupling across the gap can generate extremely strong and localized fields, which are essential for applications such as single-molecule surface-enhanced Raman spectroscopy (SERS)²¹ or extreme-ultraviolet (EUV) generation⁷¹. However, the antenna response is very sensitive to small environmental changes at the gap¹³⁸⁻¹⁴⁰. Thus, the presence of molecules or semiconductors in the gap (as usually is the case in spectroscopy or detector applications) can dramatically affect the antenna's far-field optical response with the possibility of degrading the antenna performance. On the other hand, we can take advantage of this effect for versatile tuning of the antenna response. In chapter 2.3, we discussed briefly the work of Alù et al.^{9,73} which described the possibility of tuning the response of optical antennas by antenna loading, a concept adapted from radio frequency (RF) technology. Following the RF design rules, they theoretically demonstrated that the scattering response and resonance frequency of optical antennas can be tuned by loading the antenna gap with either metals or dielectrics acting as inductors or capacitors, respectively. In this chapter, we present an experimental study of how loading of antenna gaps affects the *near-field* response using scattering-type scanning near-field optical microscopy (s-SNOM)²⁴. We provide experimental evidence that the local near-field amplitude and phase response can be controlled by antenna loading.

5.2. Experimental near-field maps of loaded gap antennas

Our experiments were performed with antennas based on gold nanorods designed for fundamental dipolar resonance at mid-infrared frequencies. The rods (1,550 x 230 x 60 nm) were fabricated on a silicon substrate by electron-beam lithography and show a far-field resonance at a wavelength of $\lambda = 9.6 \mu\text{m}$ (spectrum was shown in Figure 19 on page 64). The fabrication had been performed by K. Crozier et al. in a previous work². The topography of such a rod is shown in Figure 28a. To study how the progressive loading of an antenna gap affects the near-field distribution, we used focused ion beam (FIB) milling to prepare gaps of different shapes and sizes at the centre of the rods. By introducing a complete cut at the center of the nanorod, we fabricated gaps of 80 nm width that isolate both nanorod segments (see topography image in Figure 28d). In order to fabricate loaded gap antennas, we only partially cut the nanorod center, leaving a small metal bridge inside the gap that still connects the two nanorod segments. The topography images in Figure 28b,c show two nanorods with a small metal bridge of different diameters inside the gap. We used our transmission-mode s-SNOM which was described in chapter 3.2 to record amplitude and phase images of the nanorods (see schema in Figure 16). The s-SNOM was operated at the resonance wavelength of the unmodified nanorod (see topography image in Figure 28a), at $\lambda = 9.6 \mu\text{m}$. A residual background contribution in the optical images shown in Figure 28 has been removed using the procedure described in chapter 3.3.1.

In a first experiment with well established dipole antennas² (Figure 28a) we demonstrate that transmission-mode s-SNOM equipped with dielectric tips allows for reliable mapping of antenna near-field modes. Figure 28a shows the infrared near-field amplitude and phase images of a continuous (unmodified) nanorod. The images reveal strong-amplitude signals at the rod extremities and a phase jump of about 180° at the rod centre, providing direct experimental evidence of an anti-phase field oscillation as expected for the dipolar near-field mode. To analyze the image contrast, we perform numerical calculations of the x- and z-components of the near-field distribution of a 1,550-nm-long nanorod in resonance at a wavelength of $9.6 \mu\text{m}$ (see chapter 3.3.2 for further

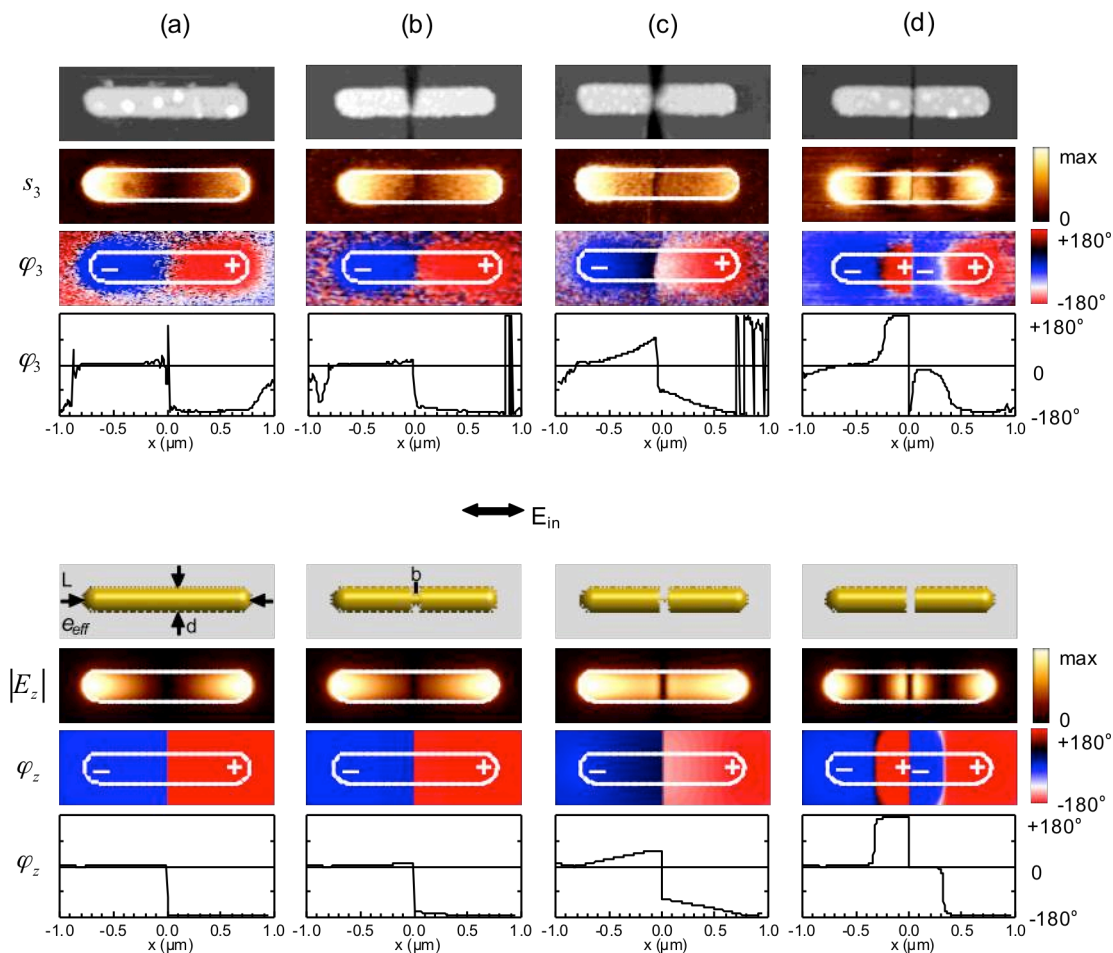


Figure 28: Near-field images of progressively loaded nanoantennas at a wavelength $\lambda = 9.6 \mu\text{m}$. **(a)** Continuous rod antenna **(b)** Low-impedance loaded antenna where a thick metal bridge connects the two antenna segments. **(c)** High-impedance loaded antenna where a tiny metal bridge connects the two antenna segments. **(d)** Fully-cut antenna where the two antenna segments are completely separated. Top: Experimental results showing topography and near-field amplitude s_3 and phase φ_3 images. Bottom: Theoretical near-field distribution of a model system, a 1550 nm long Au rod with $d = 230$ nm diameter and an 80 nm gap in its center, embedded in an effective medium of dielectric value $\epsilon_{\text{eff}} = 6.34$. The gap is bridged by gold disks of 80 nm length with diameter **(a)** $b = 230$ nm, **(b)** $b = 80$ nm, **(c)** $b = 40$ nm (amplitude image) and $b = 30$ nm (phase image), **(d)** $b = 0$ nm. The near-field images show the z-component of the electric field in amplitude E_z and phase φ_z in a height of 50 nm above the rod surface. In all phase images, the phase is set to 0° at the left antenna extremity.

information). Comparison with the experimental data clearly shows that the amplitude and phase of the z-component, $|E_z|$ and φ_z , are probed¹¹⁷ (Fig. Figure 28a, bottom).

In Figure 28d we study a nanorod that was fully cut in its centre, representing an unloaded gap antenna. The topography image clearly reveals the two closely spaced segments separated by a central gap of about 80 nm. The near-field images show that both antenna segments oscillate in a dipolar-like mode, featuring high amplitude signals at the antenna extremities and near the gap, as well as a phase jump of 180° near the centre of each segment and inside the gap. This is in good agreement with numerical calculations assuming an 80-nm gap in the rod centre (Figure 28d, bottom).

The near-field patterns of the gap antennas are completely changed when a metal bridge (representing the load) connects the two antenna segments (Figure 28b). Near the gap, in contrast to the fully-cut rod (Figure 28d), no significant near fields are observed. The topography clearly reveals the deep, wedge-like cut through the rod center and also shows the metal bridge at the lower rim of the rod. Obviously, the small metal bridge (about 10% of the total cross section of the nanorod, estimated from the topography) suffices to restore the fundamental dipolar near-field mode of the continuous rod (Figure 28a). We attribute this effect to a current flow through the bridge that prevents charge pile up at the gap. A highly interesting near-field distribution is observed in Figure 28c where a much thinner metal bridge connects the nanorod segments. The bridge cross section is estimated from the topography to be about 2% of the total rod cross section, thus being significantly reduced compared to Figure 28b. The near-field images show striking differences to both the continuous and fully-cut rods. We observe a significant amplitude signal along the total length of each segment and a considerable phase gradient of about 80° .

To further illustrate this interesting behavior, we monitored the near-field oscillations of the antennas in space and time. Owing to the simultaneous acquisition of amplitude $s_3(x, y)$ and phase $\varphi_3(x, y)$ signals, we can represent the near field at a sample position (x, y) and at time t by

$$f(x, y, t) = \text{Re}[s_3(x, y)e^{i\varphi_3(x, y) - i2\pi t/T}], \quad (42)$$

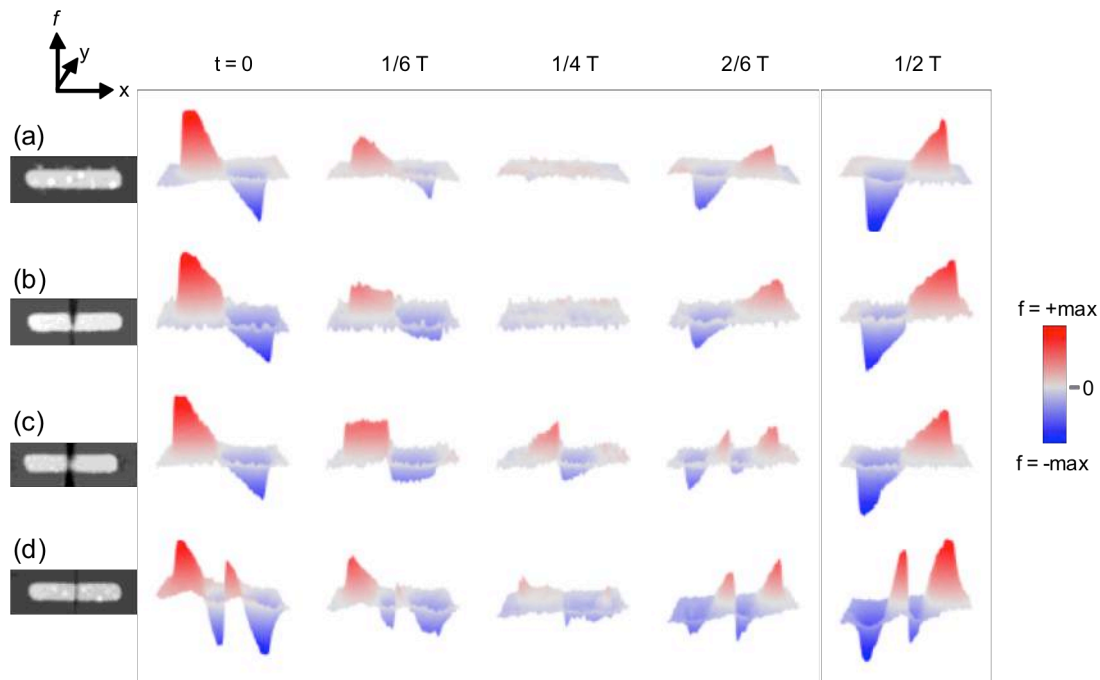


Figure 29: Time evolution of the antenna's near-field distribution f calculated with the experimental data from Figure 28. (a) Continuous rod antenna. (b) Low-impedance (inductive) loaded antenna (thick metal bridge). (c) High-impedance (inductive) loaded antenna (tiny metal bridge). (d) fully-cut antenna. T denotes the oscillation period.

where T is the oscillation period. A series of snapshots of f for all four antennas is shown in Figure 29. For the continuous rod (Figure 29a, obtained from data in Figure 28a) the snapshots clearly show the time evolution of a single dipolar oscillation, whereas the result for the fully-cut rod (Figure 29d) reveals two closely spaced dipolar-like modes evolving simultaneously in time. In the case where the tiny metal bridge connects the antenna segments (Figure 29c), however, we observe a significant time delay between the near fields at the gap and the antenna extremities.

Please note that it can be assumed that the FIB-modified nanorods were measured off-resonance. Nevertheless, the near-field spectrum of typical metal nanorods exhibits significant amplitude values at wavelengths well above the fundamental dipolar resonance which can be attributed to the lightning rod effect (long-wavelength tail, see

chapter 1.5.2). Therefore, it can be expected that near-field imaging at long wavelengths still yields sufficiently strong signals.

5.3. Numerical study of gap antennas with different bridge sizes

To analyze the near-field behavior of the metal-loaded antennas (Fig. 2b,c), we calculate the z -component of the near-field amplitude $|E_z|$ and phase φ_z , assuming an 80-nm gap in between the antenna segments, loaded with 80-nm-long cylindrical gold bridges of diameters between $b = 0$ nm and $b = 230$ nm. These calculations were performed by A. Garcia-Etxarri at J. Aizpurua's group at the Centro de Fisica de Materiales (CSIC-UPV/EHU) and Donostia International Physics Center (DIPC) in San Sebastian. The results are shown in Figure 30 and reveal that by progressive antenna loading (increasing bridge diameter b) the near-field pattern of the fully cut rod ($b = 0$) evolves towards the fundamental dipolar mode of the continuous rod. Comparing experiment and theory, we can assign to each s-SNOM image a calculated near-field pattern. For the antenna in Figure 28b we obtain good agreement for a bridge diameter $b = 80$ nm, which corresponds to 12% of the rod's cross section. This is consistent with the bridge size estimated from the topography image. The s-SNOM images in Figure 28c match well with calculated near-field patterns for b between 30 to 40 nm ($\sim 2\%$ of the rod cross-sectional area), thus confirming that indeed a tiny metallic bridge is connecting the two segments in our experiment. It is interesting to note that the variation of the single parameter b is sufficient to reproduce all the experimentally observed near-field patterns (Figure 28a–d).

To provide further theoretical insights, we calculate the extinction spectra of the gap antennas for bridge diameters between 0 nm and 100 nm, which are summarized in the contour plot of Figure 31. These calculations were performed by A. Garcia-Etxarri at J. Aizpurua's group at the Centro de Fisica de Materiales (CSIC-UPV/EHU) and

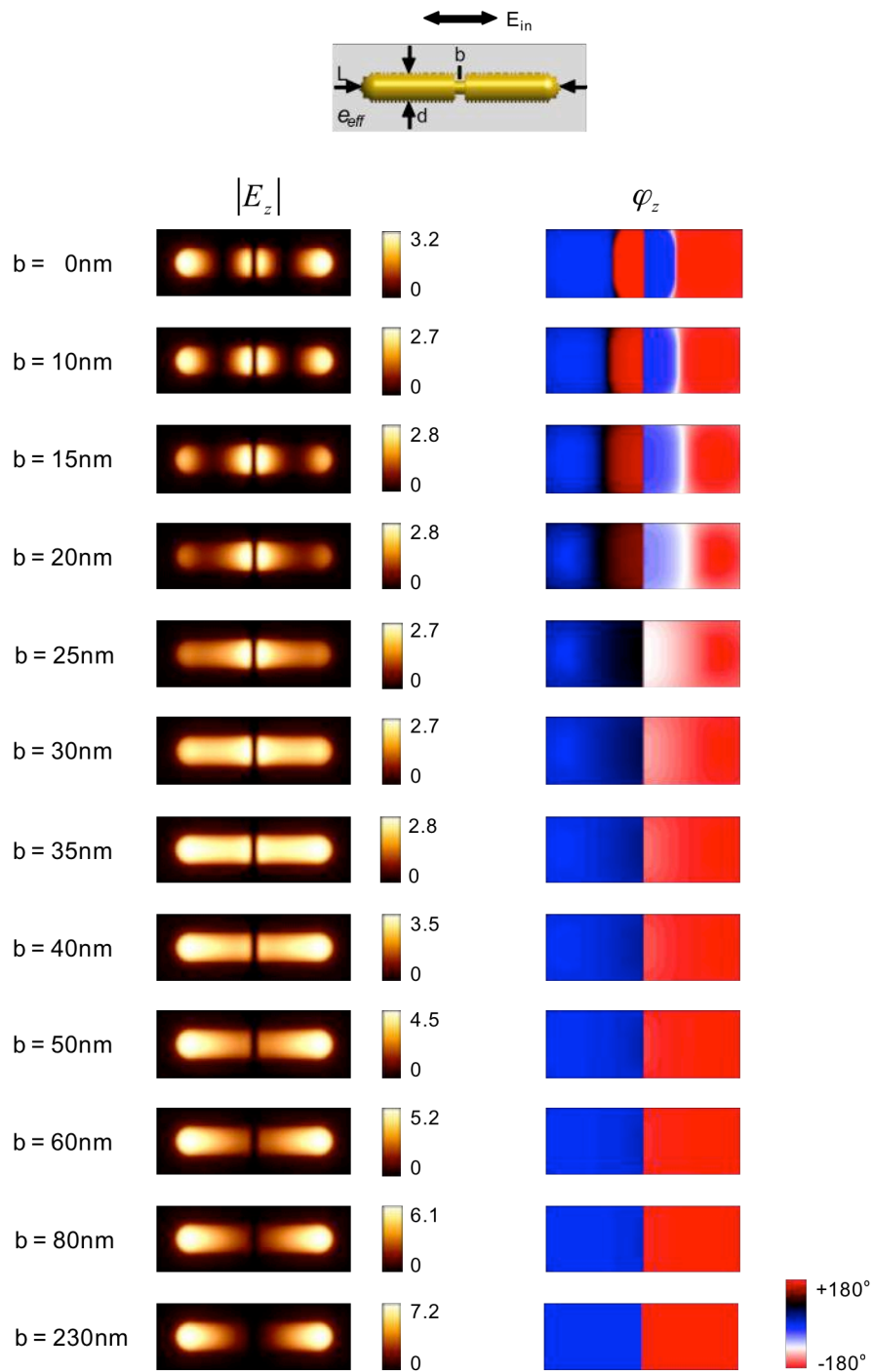


Figure 30: Near-field distribution of two Au nanorod segments of 230 nm diameter and separated by an 80 nm gap. The gap is progressively loaded with 80 nm long Au disks of a diameter b between 0 nm and 230 nm (antenna length $L = 1550$ nm, diameter $d = 230$ nm, effective medium $\epsilon_{eff} = 6.34$). Amplitude $|E_z|$ and phase φ_z of the z-component of the electric field are shown (normalized to the incident field).

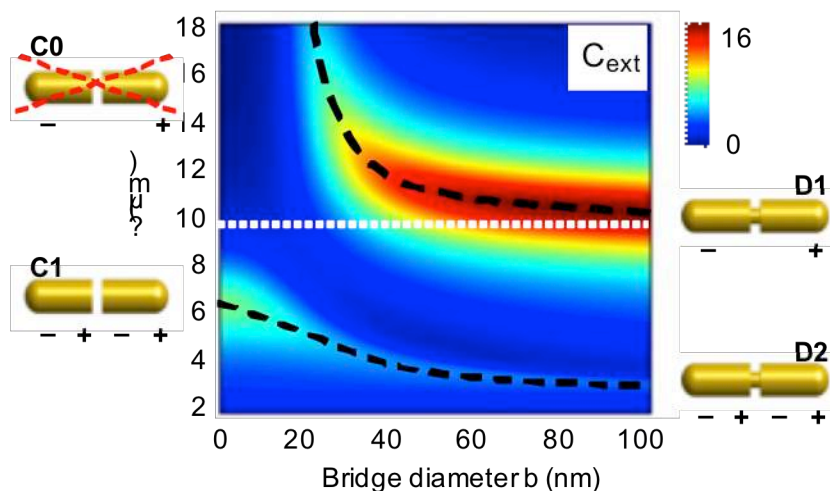


Figure 31: Extinction cross section calculated for the antennas considered in Figure 28 as a function of the bridge diameter b , normalized to the projected area of the antenna. The dashed black lines trace the extinction resonances. The first-order and the second-order mode of the continuous rod are marked by D1 and D2, respectively. For antennas with $b = 0$ (isolating gap), C1 is the first-order mode. The zero-order mode C0 is unphysical because it would have finite charge on each antenna segment⁶.

Donostia International Physics Center (DIPC) in San Sebastian. For large bridge diameter b , we observe a first-order dipolar mode (D1) of the antenna at around $\lambda \approx 10 \mu\text{m}$ (according to the experimental and theoretical near-field distributions shown in Figure 28b) and a weaker second-order dipolar mode (D2) at $\lambda = 3.5 \mu\text{m}$. With decreasing bridge diameter b , we observe a slight red shift of both modes. Reaching small bridge diameters $b < 50 \text{ nm}$, the behavior changes significantly. The first-order mode (D1) experiences a divergent red-shift at $b \approx 20 \text{ nm}$ while being increasingly damped. This can be explained by the restriction of the charge flow across the gap that is necessary to build up a mode structure compatible with D1 (for information on the mode structure see Figure 5 on page 21). Thus, in the limit of very small bridge diameters, the first-order mode (D1) cannot be excited anymore. The second-order mode (D2), in contrast, is enhanced with decreasing b and turns into the first-order mode of the coupled nanorods (C1), owing to the compatible structure of both modes. Considering now the antenna response at the fixed wavelength $\lambda = 9.6 \mu\text{m}$, we clearly observe a transition from the first-order dipolar mode (D1) of a continuous rod (large b) towards the mode of

the coupled nanorods (C1) when b is decreasing. At a given bridge diameter of 30 nm (corresponding to our experimental situation where a tiny bridge connects the antenna gap, Figure 28c) the antenna response at $\lambda = 9.6 \mu\text{m}$ wavelength lies in between the two branches coming from D1 and D2. Thus, the near-field distribution of the antenna comprises contributions of both branches, yielding the strong phase shift on each antenna segment, an effect that we clearly identify in both the experimental and calculated near-field images.

5.4. Modeling the antenna loading with circuit theory

In the radio frequency (RF) range, circuit theory is an essential tool for the efficient design of antenna devices. Adopting RF concepts, we now show how the behavior of our loaded infrared antennas can be explained within the framework of optical circuit theory, which has been recently introduced by Engheta *et al.*^{9,73,76} (see chapter 2.3). We can describe the impedance of the antenna load Z_{load} as a parallel circuit composed of the inductive impedance of the metallic bridge Z_{bridge} and the capacitive impedance of the effective medium filling the gap Z_{gap} , given by

$$\frac{1}{Z_{\text{load}}} = \frac{1}{Z_{\text{bridge}}} + \frac{1}{Z_{\text{gap}}} \quad (43)$$

with

$$Z_{\text{bridge}} = \frac{ig}{\omega \varepsilon_{\text{Au}} \pi \left(\frac{b}{2}\right)^2}, \quad (44)$$

$$Z_{\text{gap}} = \frac{ig}{\omega \varepsilon_{\text{eff}} \pi \left[\left(\frac{d}{2}\right)^2 - \left(\frac{b}{2}\right)^2 \right]}. \quad (45)$$

5.4 Modeling the antenna loading with circuit theory

Here, g is the gap width (80nm), ω the infrared frequency, ϵ_{Au} the dielectric value of gold and ϵ_{eff} the dielectric value of the effective medium filling the gap of our model antennas considered in Figure 28 and Figure 31.

In Figure 32a we display a contour plot that shows the value of the load reactance X_{load} (given by $Z_{\text{load}} = R_{\text{load}} - iX_{\text{load}}$) as a function of bridge diameter b and wavelength λ , highlighting regions of inductive (blue) and capacitive (red) behavior. Comparing the evolution of the antenna modes (Figure 31) with the behavior of X_{load} (Figure 32a), we find an interesting connection: The first-order mode D1 strongly shifts to longer wavelengths when X_{load} increases (more inductive, displayed in darker blue). The region of capacitive X_{load} , however, does not support the D1 mode. The intensity of the D2 mode in contrast strongly increases when the load becomes mainly capacitive.

We can describe the load-induced spectral shifts of the antenna modes by modeling our infrared dipole antennas as a series combination of the load impedance Z_{load} ^{9,73} and the dipole intrinsic impedance $Z_A = R_A + iX_A$ (Figure 32b). We evaluate the dipole intrinsic impedance Z_A using eqs. (18), (19) in chapter 2.2. To this end, we assume a wave vector $k = 2\pi/(\lambda/n_{\text{eff}})$ using the wavelength λ/n_{eff} in the effective medium $n_{\text{eff}} = \sqrt{\epsilon_{\text{eff}}} = 2.52$ and assuming a wave impedance of the effective medium of $\eta = \sqrt{\mu_0/\epsilon_{\text{eff}}\epsilon_0} = 150 \Omega$. In this equivalent circuit consisting of the antenna and its load, the antenna resonance occurs when the load reactance cancels the dipole intrinsic reactance, $X_{\text{load}} = -X_A$. Evaluating this condition, we obtain the resonance wavelength as function of the bridge size b . The result is shown in Figure 32a by dashed lines. For large b , the circuit resonance appears at about $9.3 \mu\text{m}$ wavelength, which is in good agreement with the resonance wavelength obtained from the extinction spectrum (Figure 31). With decreasing b , still in the inductive region, we find that the circuit resonance is red-shifted owing to an increase of the load reactance X_{load} (darker blue). Below the critical bridge size b_c – which we define as the turning point where the load changes from inductive to capacitive nature – the circuit resonance suffers an abrupt change, shifting to shorter wavelengths owing to the change of sign of X_{load} , and correspondingly of X_A . Comparing the evolution of the circuit resonances (dashed lines in Figure 32a) with the spectral behavior of the antenna modes (dashed lines in Figure 31), we find a remarkable agreement considering the simplicity of the model based on classical antenna theory. We

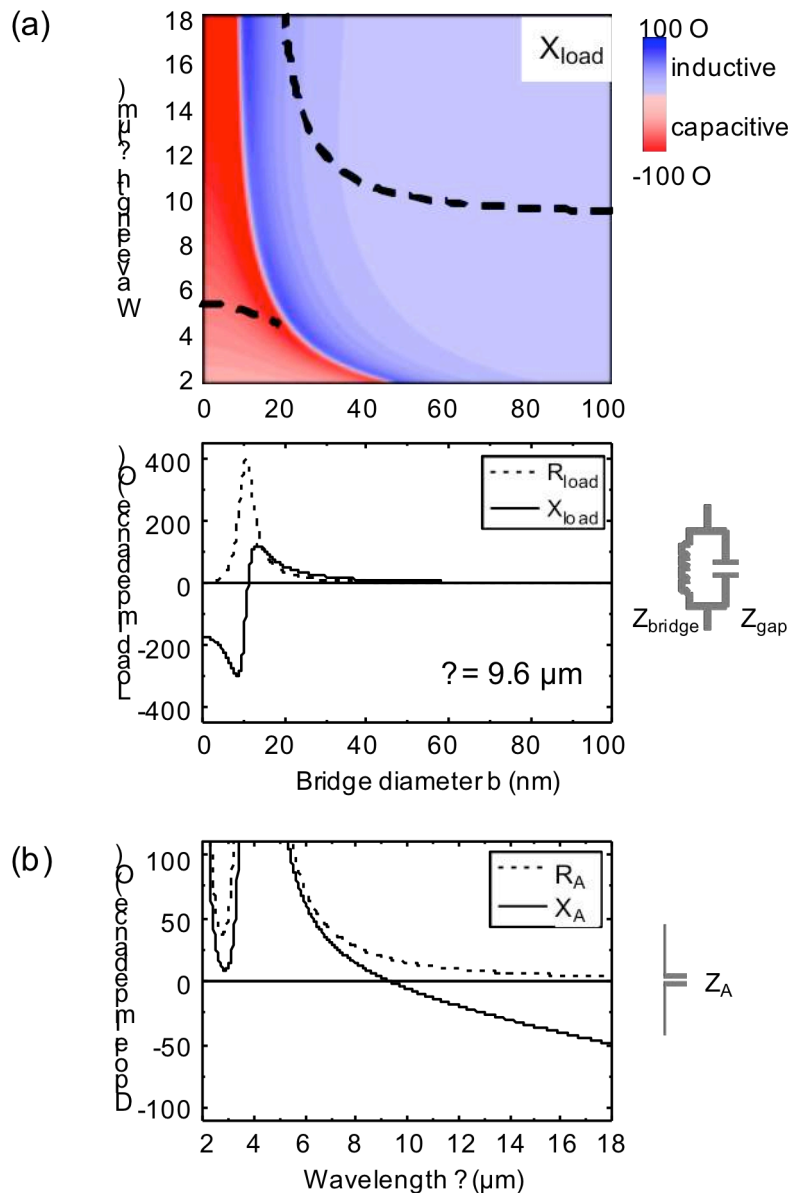


Figure 32: (a) Top: Contour plot displaying the load reactance X_{load} as a function of b and wavelength λ . Regions of capacitive reactance (negative X_{load}) are shown in red, regions of inductive reactance (positive X_{load}) in blue. The black dashed lines trace the first-order antenna resonances calculated by means of circuit theory. Bottom: Load resistance R_{load} and load reactance X_{load} displayed as a function of b , calculated for $\lambda = 9.6 \mu\text{m}$. (b) Intrinsic resistance R_A and reactance X_A of a cylindrical dipole antenna as a function of wavelength. The calculation is based on standard equations of antenna theory¹ and assumes a 1550 nm long antenna of 230 nm diameter embedded in an effective medium with $\epsilon_{\text{eff}} = 6.34$.

expect an even better agreement by taking into account plasmonic effects⁷ that are already present at infrared frequencies^{16,57}.

Finally, we address how the role of the load impedance affects the near-field distribution of the antennas. At $\lambda = 9.6 \mu\text{m}$ the dipole intrinsic impedance amounts to $Z_A = (17 + 2i) \Omega$ (read out from Figure 32b). For large bridge diameters ($b > 80 \text{ nm}$) we find that the load impedance Z_{load} is considerably smaller than Z_A , thus facilitating current flow through the load. Consequently, accumulation of charges at the gap is very low, yielding negligible near fields in its vicinity (Figure 28b). Below the critical bridge size b_c , the load impedance is of capacitive nature. Therefore, charges are piled up at the gap, which generate strong near fields, as observed both in experiment and calculations (Figure 28d). Interestingly, the deviation of the near-field patterns from dipolar-like modes (Figure 28c) occurs close to the critical bridge size (see also Figure 30), thus confirming that the change of the near-field distribution is a consequence of the transition from inductive to capacitive load impedance.

5.5. Conclusions

In conclusion, the near-field images of gap antennas presented here provide direct experimental evidence that the local near-field amplitude and phase distribution can be controlled by antenna loading. This opens the door for designing near-field patterns without the need to change antenna length, which could be highly valuable for the development of compact and integrated nanophotonic devices.

6. Nanofocusing of Mid-Infrared Energy with Tapered Transmission Lines

Mid-infrared radiation allows to analyze a wide range of different material properties including chemical composition and structure of matter^{154,155}. Infrared spectroscopy is thus an essential analytical tool in many sciences and technologies. The diffraction limit, however, challenges the study of individual molecules and nanostructures, as well as the development of highly-integrated mid-infrared optical devices¹⁵⁶. Here we experimentally demonstrate mid-infrared nanofocusing by propagating a mid-infrared surface wave along a tapered two-wire transmission line. The tapering yields a compression of the electromagnetic energy carried by the surface wave. Employing vector near-field microscopy^{157,158}, we directly visualize the evolution of the energy compression into a nanoscale confined infrared spot of 60 nm diameter ($\lambda/150$) at the taper apex. Our work opens avenues for the development of not yet existing chemical and biological sensing tools based on infrared surface waves, including miniaturized spectrometers and lab-on-a-chip integrated (bio)sensors.

6.1. Introduction

An efficient route to circumventing the diffraction limit of conventional optical elements is based on the use of plasmonic antennas and waveguides^{27,55,109,159,160}. These elements allow for the focusing, guiding and controlling of light on the nanometer scale and have therefore opened the door to optical imaging with nanoscale resolution²⁷, single-molecule Raman spectroscopy²¹ and the development of metamaterials¹⁶¹ and compact optical circuits⁷⁷. As we have described in the introduction in chapter 1, one of the most common types of plasmonic antennas used for nanofocusing light are metal nanoparticles and nanorods. Tuned to be in resonance with the illuminating light wave, they convert propagating free-space radiation into highly concentrated near fields (hot spots) at the rod extremities or in nanoscale gaps between them^{21,27,55,136,157,159,160}. Alternatively, nanofocusing of light can be achieved by the compression of surface plasmon polaritons (SPPs) propagating along tapered metal nanowires¹⁶²⁻¹⁶⁷ or slot waveguides¹⁶⁸⁻¹⁷⁰. In contrast to antenna focusing, a propagating surface wave (rather than a free-space propagating wave) is focused. For example, in case of the tapered nanowire, the SPP mode would be efficiently excited at the broad end of the tapered metal wire, e.g. by a grating coupler^{164,165}. When the SPP mode propagates along the wire, the SPP fields are more and more localized at the wire surface as the wire width steadily decreases, leading to a strong energy concentration on the nanoscale¹⁷¹. A nanofocus (hot spot) is then created in a very small volume at the tip of the tapered wire. Applied in near-field microscopy¹⁷² and tip-enhanced Raman spectroscopy¹⁶⁶, this mechanism offers an improved signal-to-background ratio, because the SPP excitation and the nanofocus at the taper apex are spatially separated. Waveguide focusing will also be an essential building block in future integrated plasmonic circuits^{18,166}, where SPPs are the carriers of optical energy.

For the development of nanoscale-resolving infrared (IR) and terahertz (THz) probes and ultra-sensitive miniaturized spectrometers, however, one faces the problem that the surface waves are weakly guided in this spectral range because of the large negative dielectric permittivity of metals¹⁷³ (see Figure 2 on page 11). An improved guiding of SPPs at THz frequencies can be achieved by patterning metal surfaces, supporting

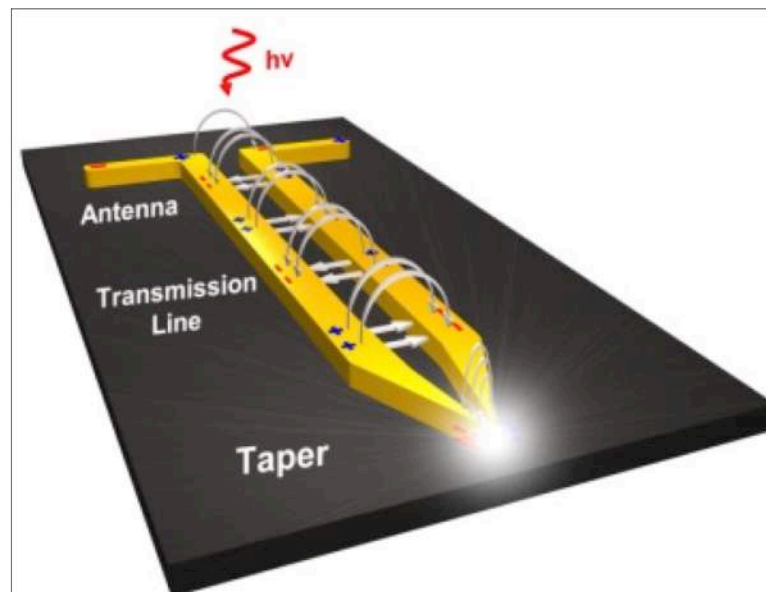


Figure 33: Concept of infrared nanofocusing with a tapered transmission line.

surfaces waves called spoof SPPs¹⁷⁴. The patterning (i.e. perforating) of the metal surface changes strongly the dispersion relation of the surface mode, yielding a dispersion relation similar to that of SPPs. Particularly, the bending of the SPP dispersion can be mimicked at far lower frequencies, yielding a strong coupling to the surface even at THz frequencies. Also the surface of tapered metal wires can be patterned, allowing for the concentration of THz radiation with spoof SPPs¹⁷⁵. However, nanoscale dimensions are difficult to achieve. A different route with which to focus radiation is based on slot waveguides^{176,177} where the electromagnetic energy is bound between two metal surfaces. It was predicted that tapered coaxial waveguides which are terminated by funnel-type adiabatic tapers allow for a nanoconcentration of THz radiation¹⁷⁶. There, the smallest achievable focus size is limited by the skin depth effect in metal (around 30 to 60 nm). A similar concept has recently been demonstrated experimentally with tapered, two parallel metal plates¹⁷⁸, achieving a subwavelength THz focus of $\sim 10 \mu\text{m}$.

In the mid-infrared spectral range - being in the transition range between strong plasmonic and nearly ideal metallic behavior - surface wave guiding is a widely unexplored terrain from both fundamental and applied perspectives. Recently, it has been demonstrated that mid-infrared energy can be guided with two-wire transmission

lines^{179,180}. This concept is adapted from radio frequency technology, where two-wire transmission lines have been used in the past to carry radio frequency (RF) signals in television and radio applications (see Chapter 2.1).

In this chapter, we predict and experimentally verify mid-infrared nanofocusing with tapered transmission lines by using compression of mid-infrared surface waves, as illustrated in Figure 33. We propose and realize a novel design including tapering of both the gap and the metal wires. Such architecture is essential for providing a nanofocus at a sharply pointed extremity that can be used as a scanning probe tip or local sensing device. To verify experimentally the extraordinarily strong lateral confinement of the surface wave, we applied polarization- and phase-resolved scattering-type near-field optical microscopy (s-SNOM) which we have recently developed to measure the vectorial field distribution of nanoscale optical fields (chapter 4).

6.2. Verification of energy transport in two-wire transmission lines

In this work, the transmission line consists of two parallel metal wires. A dipole antenna is attached to the non-tapered end of the two-wire transmission line. Infrared illumination with polarization parallel to the antenna can therefore launch a surface wave on the transmission line. This coupling mechanism is well known from radio frequency technology (chapter 2.2) and has been studied theoretically in the optical regime⁵ (chapter 2.3). The launching of a surface wave and its propagation along mid-IR transmission lines have been demonstrated recently¹⁸⁰. In Figure 34a–c, we first verified and characterized mid-infrared energy transport in untapered two-wire transmission lines to serve as a reference for the following nanofocusing experiments. To that end, we fabricated a transmission line consisting of two flat Au wires of 200 nm width and 40 nm height, separated by a 300 nm gap. The length of the wires is 15 μm , a 2 μm long dipole antenna is attached to the left end for the excitation of the mid-IR surface mode. The structures were fabricated by high-resolution electron-beam lithography and metal lift-

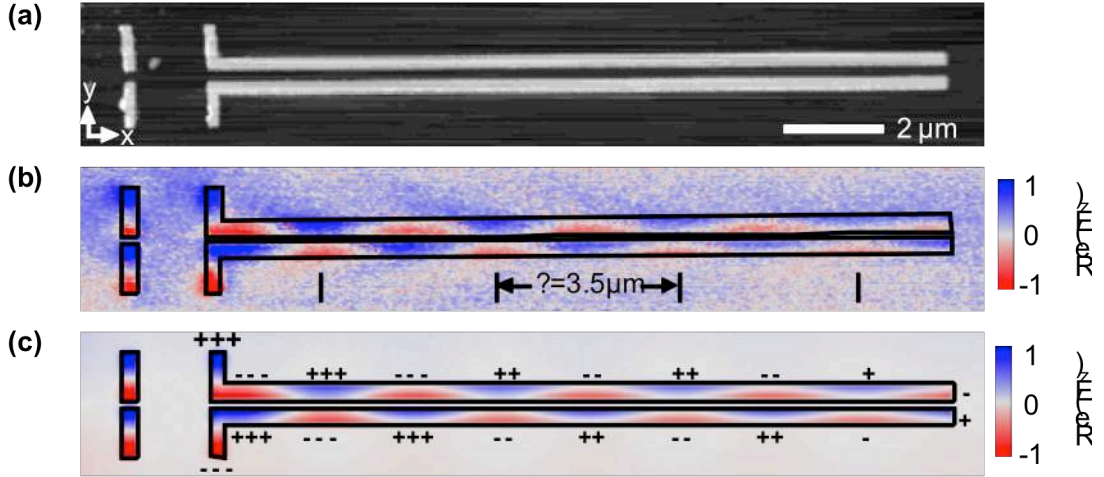


Figure 34: Energy transport in two-wire transmission lines. (a) Topography image of an antenna-coupled two-wire transmission line. Its calculated mode profile is shown in Figure 35b, case (A). (b) Experimental near-field image taken at $\lambda = 9.3 \mu\text{m}$, showing $\text{Re}(E_z) = |E_z|\cos(\varphi_z)$. (c) Numerically calculated near-field image showing $\text{Re}(E_z) = |E_z|\cos(\varphi_z)$.

off on double-side-polished silicon substrates. A bilayer polymethyl methacrylate (with 495,000 molecular weight at the bottom and 950,000 molecular weight at the top) was used as electron-sensitive polymer. A 40 nm Au film was thermally evaporated in high vacuum on top of a 3nm thick Ti layer, e-beam evaporated for adhesion purposes. Design of the structures was done by P. Alonso-Gonzalez from the nanooptics group at CIC nanoGUNE Consolider. The structures were fabricated in a collaboration with the nanodevices group at CIC nanoGUNE Consolider. We then imaged the transmission line with our s-SNOM at a wavelength of $\lambda = 9.3 \mu\text{m}$. To visualize the field distribution and the mode structure of the surface wave, we show in Figure 34b the real part of the vertical near-field component, $\text{Re}(E_z) = |E_z|\cos(\varphi_z)$, where $|E_z|$ is the near-field amplitude and φ_z the phase. We observe two dipolar-like modes on the antenna segments with strong fields at the antenna ends and at the gap, as expected for a mid-IR gap antenna¹⁰⁹. The fields extend along the two wires, periodically changing their polarity. This provides direct experimental evidence of a propagating surface wave. We find a decreasing field strength with increasing distance x from the antenna (source), indicating propagation losses. From the oscillation period and the field decay we determine an effective wavelength $\lambda_{\text{eff}} = 3.5 \mu\text{m}$ and a propagation length $L \approx 8 \mu\text{m}$

(defined as the $1/e$ decay of the field amplitude). The experimental image is in excellent qualitative agreement with numerical simulations of the near-field distribution (Figure 34c) when we assume for the Si substrate a refractive index of $n_{\text{Si}} = 3.07$. Our results show that indeed mid-IR energy can be transported in our transmission lines of subwavelength-scale width $W = \lambda/13$.

6.3. Numerical study of the surface mode properties

Basic insights about the field confinement and propagation of mid-infrared energy ($\lambda = 9.3 \mu\text{m}$) in two-wire transmission lines were obtained by a numerical study using a finite-element mode solver (Figure 35a–c). We considered infinitely long transmission lines of total width $W = 2w + g$, consisting of two parallel gold wires (width, w ; height, 40 nm) on a silicon substrate, separated by an isolating gap of width g (Figure 35a). In Figure 35b, the antisymmetric mode solutions (cross section of the near-field distribution) for three different transmission lines (A–C) are shown. We find that the near fields associated with these modes are strongly confined on the scale of the transmission-line width W , even for the extremely narrow transmission line C with $W = 90 \text{ nm}$ ($\lambda/100$). We analyze the propagation properties of the modes in Figure 35c, showing the effective wavelength λ_{eff} and the propagation length L when both the wire and gap widths (w and g) are reduced, following the cases A–C. With decreasing width W , both the wavelength and the propagation length decrease, which can be attributed to the increasing amount of energy propagating inside the metal (skin depth effect)¹⁷⁶. Interestingly, even for extremely small widths W (lines B and C), the propagation length is still of the order of one wavelength λ_{eff} . This indicates the potential to compress the mid-IR mode by propagating it along a tapered transmission line. Note that the extreme confinement of the surface mode in case C ($W = \lambda/100$) is not accompanied by a strong reduction in the effective wavelength λ_{eff} (Figure 35c). This finding differs from the

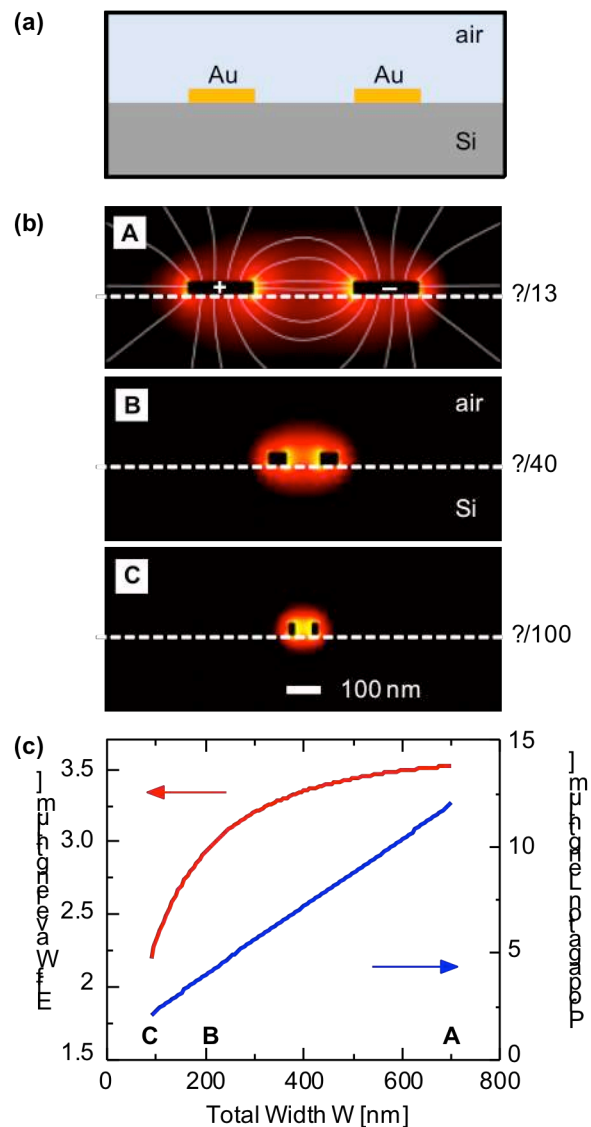


Figure 35: Propagation properties in two-wire transmission lines. **(a)** Schematics showing the cross section of the two-wire transmission line, consisting of two 40 nm thick parallel gold wires of width w , which are separated by a nanoscale gap of width g . **(b)** Numerically calculated mode profiles (logarithmic scale) for transmission lines with (A) $w = 200$ nm and $g = 300$ nm, (B) $w = 56$ nm, $g = 100$ nm, and (C) $w = 20$ nm and $g = 50$ nm. **(c)** Wavelength λ_{eff} and propagation length L as a function of the total transmission-line width $W = 2w + g$, while the wire width w and gap width g are decreased simultaneously from $w = 200$ nm to 20 nm and $g = 300$ nm to 50 nm, respectively.

plasmon compression in tapered metal nanowires at visible frequencies, where the energy accumulation and field enhancement is associated with a significant reduction of the plasmon wavelength¹⁶⁴.

6.4. Nanofocusing of mid-infrared energy with tapered two-wire transmission lines

In Figure 36, we demonstrate experimentally our concept of mid-infrared nanofocusing with a tapered transmission line. The transmission line shown in Figure 36a consists of two Au wires (200 nm wide, 6 μm long) that are separated by a 300 nm air gap. The right end of the transmission line is tapered on a length of 1 μm , with the Au wire width and the gap width being linearly reduced to 20 nm and 50 nm, respectively. This tapering corresponds to a decrease of the total width W of the transmission line from 700 nm (mode profile A in Figure 35) to 90 nm (mode profile C in Figure 35). We visualize the propagating mode by imaging the vertical near-field component, analogously to Figure 34b. It is clearly seen that the field distribution on the transmission lines narrows with decreasing width W , while the asymmetric mode structure (opposite charges on the two wires) is fully retained (Figure 36b). Remarkably, even close to the taper apex no fields are observed outside the line, providing experimental evidence of strong field confinement and the absence of leakage fields. In order to visualize the energy compression, we show in Figure 36c the intensity of the vertical near-field component, $|E_z|^2$. A continuous intensity enhancement can be observed along the taper as well as intensity modulations along the parallel wires. We attribute the latter to back reflections from the tapered part of the transmission line, in analogy to a non-terminated transmission line at radiofrequencies (see Figure 9 on page 35). At the taper apex, at $x = 6 \mu\text{m}$ distance from the dipole antenna, two extremely confined peaks are observed. The intensity at the peak position is significantly enhanced, by a factor of 30 when compared to the intensity measured at $x = 6 \mu\text{m}$ on the untapered line (Figure 34b). Our

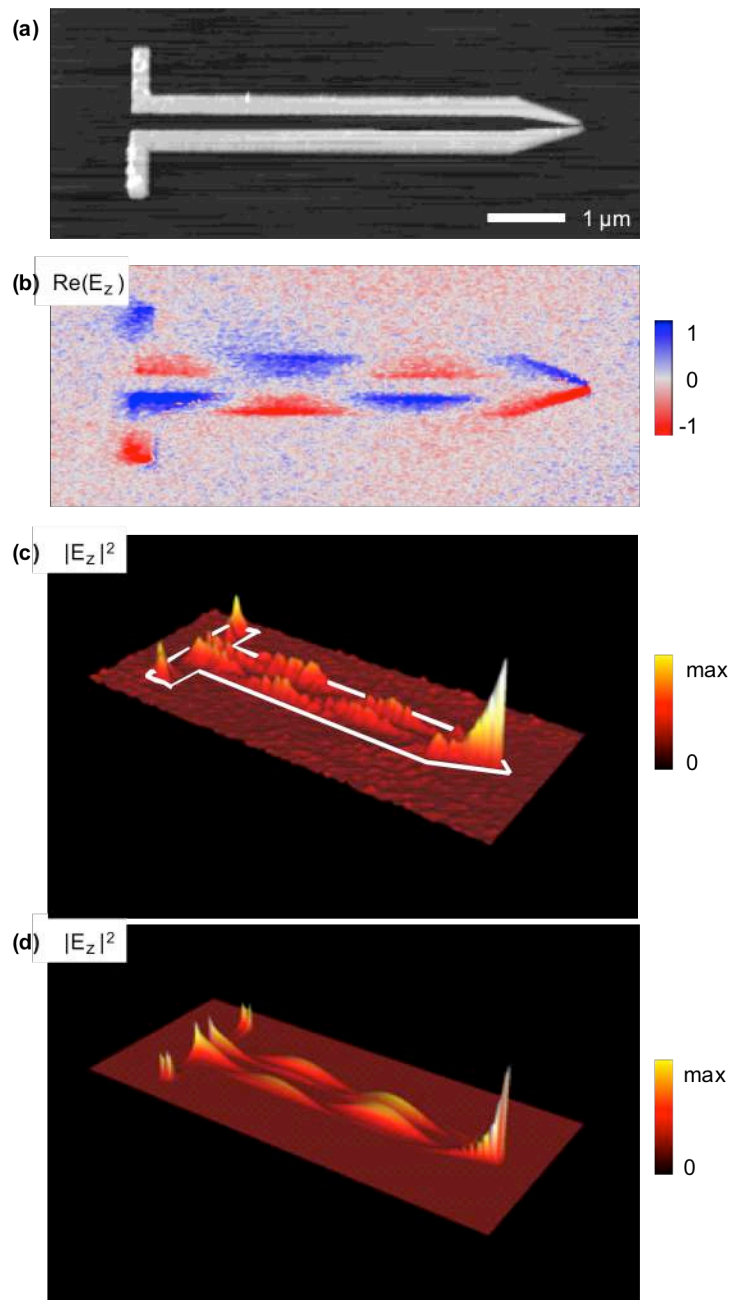


Figure 36: Nanofocusing of infrared energy with a tapered two-wire transmission line. **(a)** Topography image of the transmission line. **(b)** Experimental near-field image showing $\text{Re}(E_z) = |E_z|\cos(\varphi_z)$. **(c)** Experimental near-field image showing the intensity of the vertical field component, $|E_z|^2$. **(d)** Numerically calculated near-field image showing the intensity of the vertical field component, $|E_z|^2$.

near-field images are confirmed by a numerical simulation (Figure 36d) assuming a 5.3 μm long transmission line and provides first experimental evidence that mid-infrared energy can be compressed along a tapered transmission line.

To study the vectorial field distribution of the mid-infrared nanofocus, we recorded high-resolution images of both the vertical and horizontal near-field components of the taper region (Figure 37a). The image of the vertical (out-of-plane) near-field component $|E_z|^2$ reveals two intensity maxima (bright spots) at the taper apex. These maxima appear exactly at the wire tips, as we prove by the superposition of the topography and near-field image (Figure 37b). The existence of two maxima can be explained by the mode profile (Figure 35b), showing that the vertical near-field component essentially appears on top of the metal wires. Note that the difference in the peak intensities can be assigned to the slight asymmetric shape of the taper apex. Mapping the horizontal (in-plane) near-field component $|E_y|^2$, we find a single intensity peak inside the gap, located at the taper apex, as predicted by numerical calculations (Figure 37c). From the line profile across the peak (Figure 37d, extracted at the position indicated by the white arrows in Figure 37a), we measure an intriguingly small spot size, amounting to about 60 nm ($\lambda/150$). The high-resolution near-field images provide first direct experimental evidence that mid-infrared energy can be nanofocused using tapered transmission lines. Remarkably, mid-infrared energy can be nanofocused to a spot size comparable to what has been achieved by plasmon compression in the visible range.

Note that in this experiment the entire transmission-line structure is illuminated. To exclude the possibility that the near-field focus at the taper apex is generated by a local antenna or lightning-rod effect, we compare the tapered transmission line with an isolated taper (Figure 38). This experiment clearly shows that the isolated taper (Figure 38, right) does not generate strong fields at the taper apex. It is only when a propagating transmission-line mode is fed into the taper (Figure 38, left) that strong fields are observed at the taper apex.

Figure 37: Vectorial field distribution of the nanofocus. **(a)** High-resolution experimental near-field images of the taper apex, showing the intensity of the vertical and transverse near-field components, $|E_z|^2$ and $|E_y|^2$. **(b)** Superposition of near-field intensity and topography. **(c)** Numerically calculated near-field image showing the intensity of the horizontal field component, $|E_y|^2$. **(d)** Line profile through the nanofocus at the taper apex, experimental data (red circles) and calculated data (black line) extracted at the position indicated by the white arrows in (a) and (c), respectively.

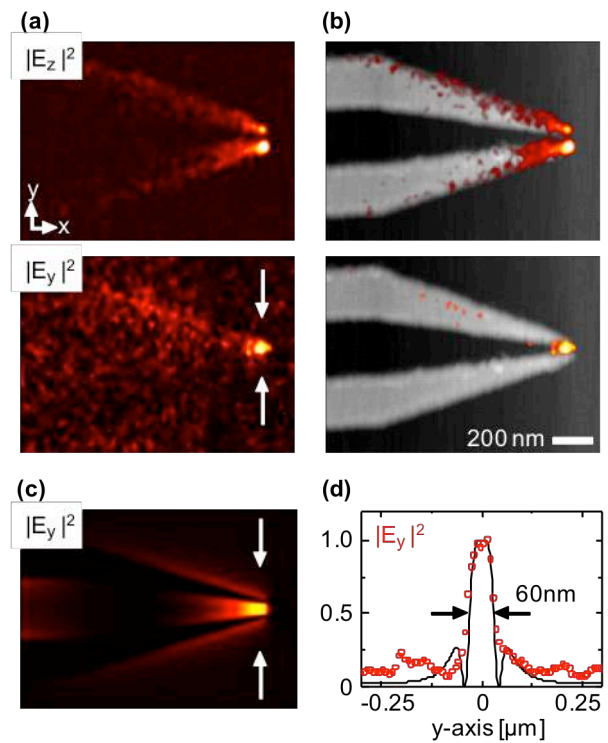
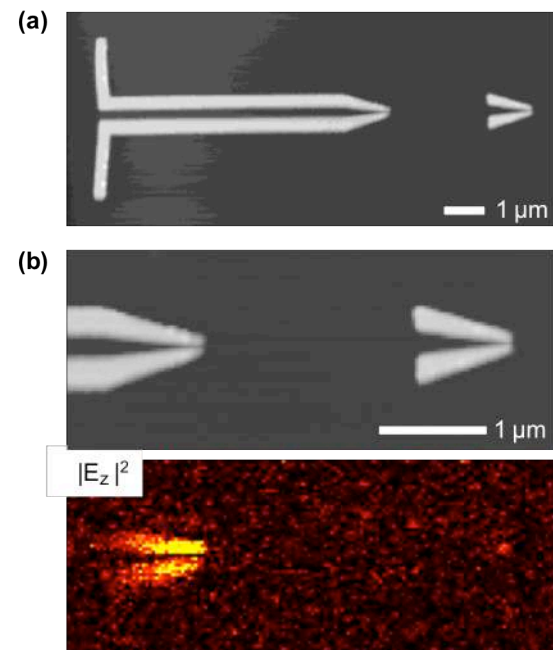


Figure 38: Control experiment comparing a tapered transmission line with an isolated taper. **(a)** s-SNOM topography image **(b)** Topography and near field image ($\lambda = 11.2 \mu\text{m}$) showing the intensity of the vertical field component, $|E_z|^2$.



6.5. Conclusions

We have experimentally demonstrated our concept of nanofocusing of mid-infrared radiation with tapered transmission lines. To this end, we first verified that a mid-IR surface wave propagates on a two-wire transmission line of only 700 nm width. With the tapered two-wire transmission line structure, our near-field images and calculations revealed that the surface wave is compressed by propagating it into the transmission-line taper. We achieved a focus spot of only 60 nm diameter at the taper apex, corresponding to the extreme sub-wavelength scale dimension of $\lambda / 150$ at $\lambda = 9.3 \mu\text{m}$ wavelength. Nanofocusing of mid-infrared energy with transmission lines opens new avenues for nanoscale imaging and sensing. It enables the development of integrated mid-infrared circuits and devices based on energy transport mediated by surface waves, which will be critical for example in future infrared-spectroscopic lap-on-a-chip applications. We also stress that both the gap and metal wire widths are tapered, providing an infrared nanofocus at a sharply pointed transmission-line apex. Such a structure could be realized on scanning probe tips, allowing for simultaneous high-resolution imaging of sample topography and infrared properties. Furthermore, the near-field images demonstrate the potential of our imaging technique (vector-field nanoscopy¹⁵⁷) to verify novel fundamental predictions and technological concepts in nanophotonics, plasmonics and metamaterials research. Offering wavelength-independent resolution, it can be used at visible, infrared and terahertz frequencies.

7. List of publications

This thesis is based on the following publications

1. M. Schnell, A. Garcia-Etxarri, A.J. Huber, K. Crozier, J. Aizpurua, and R. Hillenbrand, “Controlling the near-field oscillations of loaded plasmonic nanoantennas”.
Nature Photon. 3, 287 (2009)
(chapter 5 of this thesis)
2. M. Schnell, A. Garcia-Etxarri, A.J. Huber, K. Crozier, A. Borisov, J. Aizpurua, and R. Hillenbrand, “Amplitude- and phase-resolved near-field mapping of infrared antenna modes by transmission-mode scattering-type near-field microscopy”.
J. Phys. Chem. C 114, 7341 (2010)
(chapter 3.3 of this thesis)
3. M. Schnell, A. Garcia-Etxarri, J. Alkorta, J. Aizpurua, and R. Hillenbrand, “Phase-Resolved Mapping of the Near-Field Vector and Polarization State in Nanoscale Antenna Gaps”.
Nano Lett. 20, 3524 (2010)
(chapter 4 of this thesis)
4. M. Schnell, P. Alonso-González, F. Casanova, L. Arzubiaga, L. E. Hueso, A. Chuvilin, and R. Hillenbrand, “Nanofocusing of Mid-Infrared Energy with Tapered Transmission Lines”.
Nature Photon. 5, 283 (2011)
(chapter 6 of this thesis)

Other publications

- o F. Huth, M. Schnell, J. Wittborn, N. Ocelic, and R. Hillenbrand, “Infrared-spectroscopic nano-imaging with a thermal source”.
Nature Mater. 10, 352 (2011)
- o P. Alonso-González, M. Schnell, P. Sarriugarte, H. Sobhani, C. Wu, N. Arju, A. Khanikaev, F. Golmar, P. Albella, L. Arzubiaga, F. Casanova, L. Hueso, P. Nordlander, G. Shvets, and R. Hillenbrand, “Real-space mapping of Fano interference in plasmonic metamolecules”.
Nano Lett. 11, 3922 (2011)
- o M. Ameen, A. Garcia-Etxarri, M. Schnell, R. Hillenbrand and J. Aizpurua, “Infrared phononic nanoantennas: Localized surface phonon polaritons in SiC disks”.
Chinese Science Bulletin 55, 2625 (2010)

8. Acknowledgements

I would like to express my gratitude to my advisor Dr. Rainer Hillenbrand for the opportunity to work in the exciting field of nano-optics. I am thankful for his guidance during my PhD studies. For his support in the lab when he personally showed me how to use the microscope. For teaching me how to write papers. Particularly, I highly value the liberty he granted me in conducting the research projects, allowing me to take part in the decision which way to go. Thank you for your unconditional confidence. I am also thankful for the many conferences and scientific meetings I was allowed to attend, which gave me the valuable opportunity to meet other groups working in the field of nano-optics and to establish international contacts.

To Javier Aizpurua (CSIC-UPV/EHU – DIPC, Donostia - San Sebastián), I want to say thank you because I enjoyed very much working with him during my first steps in science. The teamwork between his group and Rainer's group was beautiful and encouraging, and also yielded some great scientific work. Javi is not only a collaborator, I consider him also a co-advisor of my PhD thesis. This is because he was there to guide me and give advices whenever I was in doubt, just as if I were one of his own students. I feel very grateful for that.

I would like to thank Prof. Txema Pitarke for the opportunity to work and carry out my experiments at CIC nanoGUNE Consolider (Donostia - San Sebastian). I also want to thank the administration of CIC nanoGUNE Consolider for their assistance. I would also like to thank Prof. Wolfgang Baumeister for the opportunity to conduct my work during the first year of my PhD studies in his department at the Max-Planck-Institute of Biochemistry (Martinsried, near München).

To the Nanooptics group, Nanodevices group and the Advanced Electron Microscopy Laboratory at CIC nanoGUNE Consolider for the fruitful collaborations. Dear Andrey Chuvilin, Federico Golmar, Felix Casanova, Libe Arzubiaga, Luis Hueso, Pablo Albella,

Pablo Alonso and Paulo Sarriugarte, thank you for your effort to push forward our common projects.

I would like to say hello to my colleagues in the Nanooptics Group: Carlos, Dmitry, Jianing, Johannes, Florian, Pablo Alonso, Pablo Albella, Paulo, Roman Sasha, and its former members: Eneko, Xabier, Scott. I also want to greet all of the people that do their daily work at CIC nanoGUNE Consolider. Thank you for contributing to the nice atmosphere at work and also after work.

I also remember the people I met and worked with at the Max-Planck-Institut for Biochemistry in Martinsried near München. My greetings go to Dr. Fritz Keilmann and Dr. Reinhard Guckenberger for sharing their expertise on SNOM and related things with me and for their support. I also like to mention the MPIB workshop because of their readily support concerning the experimental setup. A special salute goes to my former colleagues Andy, Mirijam, Thomas and all the rest of the Baumeister department. Thank you all for making my one year at the MPIB such a nice stay!

I acknowledge the financial support of my PhD studies from the “Programa de Formación de Personal Investigador” promoted by the Department of Education, Universities and Research of the Basque Government. I also acknowledge the financing from CIC nanoGUNE Consolider during the first two years of my PhD studies.

While this chapter is coming to a close, I would like to mention three more people. I would like to thank Aitzol Garcia-Etxarri (CSIC-UPV/EHU – DIPC), because it was a pleasure working with him within our several collaborations. I also would like to thank Alexander Rigort (MPIB) for teaching me how to use the FIB microscope.

I want to thank my father Michael and my mother Renate for their support, love and care. Natural science is a beautiful topic and I am thankful that they tried to show me that. I also want to thank them for making it possible that I could go to the university and study Physics.

I want to thank Vanessa's family, her parents Jose Manuel and Emilia, her sister Ainhoa, her uncles and aunts and cousins, her grandmothers, for their hospitality and for offering me a home in the Basque country.

The final acknowledgement is dedicated to my girlfriend Vanessa. She has been at my side every minute, day and night, in München and San Sebastián. I can consider myself a fortunate guy to have her as my girlfriend. This is because her company and the love I have been receiving do not have a comparison. Thank you. In love.

Martin

Donostia – San Sebastián, January 2012

9. Bibliography

- 1 Balanis, C.A., *Antenna Theory*. (John Wiley & Sons, Inc., Hoboken, New Jersey, 2005).
- 2 Crozier, K.B., Sundaramurthy, A., Kino, G.S., & Quate, C.F. Optical antennas:
Resonators for local field enhancement. *J. Appl. Phys.* **94**, 4632-4642 (2003).
- 3 Kelly, K.L., Coronado, E., Zhao, L.L., & Schatz, G.C. The Optical Properties of Metal
Nanoparticles: The Influence of Size, Shape, and Dielectric Environment. *The Journal of*
4 *Physical Chemistry B* **107**, 668-677 (2002).
- 5 Johnson, P.B. & Christy, R.W. Optical Constants of the Noble Metals. *Phys. Rev. B* **6**,
4370 (1972).
- 6 Huang, J.-S., Feichtner, T., Biagioni, P., & Hecht, B. Impedance Matching and Emission
Properties of Nanoantennas in an Optical Nanocircuit. *Nano Lett.* **9**, 1897-1902 (2009).
- 7 Aizpurua, J. *et al.* Optical properties of coupled metallic nanorods for field-enhanced
spectroscopy. *Phys. Rev. B* **71**, 235420 (2005).
- 8 Novotny, L. Effective Wavelength Scaling for Optical Antennas. *Phys. Rev. Lett.* **98**,
266802 (2007).
- 9 Schmitt, R., *Electromagnetics Explained: a handbook for wireless/RF, EMC, and high-*
speed electronics. (Newnes, Elsevier Science, Woburn, MA, USA, 2002).
- 10 Alu, A. & Engheta, N. Tuning the scattering response of optical nanoantennas with
nanocircuit loads. *Nature Photon.* **2**, 307-310 (2008).
- 11 Palik, E.D., *Handbook of Optical Constants of Solids*. (Academic Press, San Diego,
1985).
- 12 Alonso-González, P. *et al.* Real-Space Mapping of Fano Interference in Plasmonic
Metamolecules. *Nano Lett.* **11**, 3922-3926 (2011).
- 13 Garcia de Abajo, F.J. & Howie, A. Relativistic electron energy loss and electron-induced
photon emission in inhomogeneous dielectrics. *Phys. Rev. Lett.* **80**, 5180-5183 (1998).
- 14 Garcia de Abajo, F.J. & Howie, A. Retarded field calculation of electron energy loss in
inhomogeneous dielectrics. *Phys. Rev. B* **65**, 115418 (2002).
- 15 Borisov, A.G. & Shabanov, S.V. Lanczos pseudospectral method for initial-value
problems in electrodynamics and its applications to ionic crystal gratings. *J. Comput.*
Phys. **209**, 643-664 (2005).
- 16 Novotny, L. & Hecht, B., *Principles of Nano-Optics*. (Cambridge University Press,
Cambridge, UK, 2006).
- 17 Neubrech, F. *et al.* Resonant Plasmonic and Vibrational Coupling in a Tailored
Nanoantenna for Infrared Detection. *Phys. Rev. Lett.* **101**, 157403 (2008).
- 18 Tang, L. *et al.* Nanometre-scale germanium photodetector enhanced by a near-infrared
dipole antenna. *Nature Photon.* **2**, 226-229 (2008).
- Barnes, W.L., Dereux, A., & Ebbesen, T.W. Surface plasmon subwavelength optics.
Nature **424**, 824-830 (2003).

19 Nie, S. & Emory, S.R. Probing single molecules and single nanoparticles by surface-
enhanced Raman scattering. *Science* **275**, 1102-1106 (1997).

20 Kneipp, K. *et al.* Single molecule detection using surface-enhanced Raman scattering
(SERS). *Phys. Rev. Lett.* **78**, 1667-1670 (1997).

21 Xu, H., Bjerneld, E.J., Käll, M., & Börjesson, L. Spectroscopy of Single Hemoglobin
Molecules by Surface Enhanced Raman Scattering. *Phys. Rev. Lett.* **83**, 4357-4360
(1999).

22 Wang, L., Uppuluri, S.M., Jin, E.X., & Xu, X.F. Nanolithography using high
transmission nanoscale bowtie apertures. *Nano Lett.* **6**, 361-364 (2006).

23 Sundaramurthy, A. *et al.* Toward nanometer-scale optical photolithography: Utilizing the
near-field of bowtie optical nanoantennas. *Nano Lett.* **6**, 355-360 (2006).

24 Keilmann, F. & Hillenbrand, R. Near-field optical microscopy by elastic light scattering
from a tip. *Philos. Trans. R. Soc. London, Ser. A* **362**, 787-805 (2004).

25 Kalkbrenner, T. *et al.* Optical microscopy via spectral modification of a nanoantenna.
Phys. Rev. Lett. **95**, 200801 (2005).

26 Farahani, J.N., Pohl, D.W., Eisler, H.-J., & Hecht, B. Single quantum dot coupled to a
scanning optical antenna: a tunable superemitter. *Phys. Rev. Lett.* **95**, 017402 (2005).

27 Taminiau, T.H., Stefani, F.D., Segerink, F.B., & Van Hulst, N.F. Optical antennas direct
single-molecule emission. *Nature Photon.* **2**, 234-237 (2008).

28 Hartschuh, A., Sanchez, E.J., Xie, X.S., & Novotny, L. High-resolution near-field
Raman microscopy of single-walled carbon nanotubes. *Phys. Rev. Lett.* **90**, 095503
(2003).

29 Ordal, M.A. *et al.* Optical properties of the metals Al, Co, Cu, Au, Fe, Pb, Ni, Pd, Pt, Ag,
Ti, and W in the infrared and far infrared. *Appl. Opt.* **22**, 1099-1119 (1983).

30 Bennett, H.E. & Bennett, J.M., *Optical properties and electronic structure of metals and
alloys.* (North-Holland, New York, 1966).

31 Giannini, V., Fernandez-Dominguez, A.I., Heck, S.C., & Maier, S.A. Plasmonic
Nanoantennas: Fundamentals and Their Use in Controlling the Radiative Properties of
Nanoemitters. *Chem. Rev.* **111**, 3888-3912 (2011).

32 Zayats, A.V. & Richards, D., *Nano-Optics And Near-Field Optical Microscopy.* (Artech
House, Boston, USA, 2009).

33 Liedberg, B., Nylander, C., & Lunström, I. Surface plasmon resonance for gas detection
and biosensing. *Sensors and Actuators* **4**, 299-304 (1983).

34 Homola, J., Yee, S.S., & Gauglitz, G. Surface plasmon resonance sensors: review. *Sens.
Actuators, B* **54**, 3-15 (1999).

35 Ozbay, E. Plasmonics: Merging Photonics and Electronics at Nanoscale Dimensions.
Science **311**, 189-193 (2006).

36 Saxler, J. *et al.* Time-domain measurements of surface plasmon polaritons in the
terahertz frequency range. *Phys. Rev. B* **69**, 155427 (2004).

37 Williams, C.R. *et al.* Highly confined guiding of terahertz surface plasmon polaritons on
structured metal surfaces. *Nature Photon.* **2**, 175-179 (2008).

38 Jones, A.C. *et al.* Mid-IR Plasmonics: Near-Field Imaging of Coherent Plasmon Modes
of Silver Nanowires. *Nano Lett.* **9**, 2553-2558 (2009).

39 Maier, S.A., *Plasmonics: Fundamentals and Applications.* (Springer, New York, 2007).

40 Curto, A.G. *et al.* Unidirectional Emission of a Quantum Dot Coupled to a Nanoantenna.
Science **329**, 930-933 (2010).

41 Jackson, J.D., *Classical electrodynamics.* (John Wiley & Sons, 1975).

- 42 Lee, K.-S. & El-Sayed, M.A. Dependence of the Enhanced Optical Scattering Efficiency
Relative to That of Absorption for Gold Metal Nanorods on Aspect Ratio, Size, End-Cap
Shape, and Medium Refractive Index. *The Journal of Physical Chemistry B* **109**, 20331-
20338 (2005).
- 43 Link, S. & El-Sayed, M.A. *J. Phys. Chem. B* **103**, 8410-8426 (1999).
- 44 Payne, E.K., Shuford, K.L., Park, S., Schatz, G.C., & Mirkin, C.A. Multipole Plasmon
Resonances in Gold Nanorods. *The Journal of Physical Chemistry B* **110**, 2150-2154
(2006).
- 45 Bryant, G.W., Garcia de Abajo, F.J., & Aizpurua, J. Mapping the Plasmon Resonances
of Metallic Nanoantennas. *Nano Lett.* **8**, 631-636 (2008).
- 46 Aizpurua, J., Taubner, T., de Abajo, F.J., Brehm, M., & Hillenbrand, R. Substrate-
enhanced infrared near-field spectroscopy. *Opt. Express* **16**, 1529-1545 (2008).
- 47 Neubrech, F. *et al.* Resonances of individual metal nanowires in the infrared. *Appl. Phys.*
Lett. **89**, 253104 (2006).
- 48 Neubrech, F. *et al.* Resonances of individual lithographic gold nanowires in the infrared.
Appl. Phys. Lett. **93**, 163105 (2008).
- 49 Mock, J.J., Oldenburg, S.J., Smith, D.R., Schultz, D.A., & Schultz, S. Composite
Plasmon Resonant Nanowires. *Nano Lett.* **2**, 465-469 (2002).
- 50 Schider, G. *et al.* Plasmon dispersion relation of Au and Ag nanowires. *Phys. Rev. B* **68**,
155427 (2003).
- 51 Taminiu, T.H., Stefani, F.D., & van Hulst, N.F. Optical Nanorod Antennas Modeled as
Cavities for Dipolar Emitters: Evolution of Sub- and Super-Radiant Modes. *Nano Lett.*
11, 1020-1024 (2011).
- 52 Dorfmueller, J. *et al.* Fabry-Pérot Resonances in One-Dimensional Plasmonic
Nanostructures. *Nano Lett.* **9**, 2372-2377 (2009).
- 53 Kane, Y. Numerical solution of initial boundary value problems involving maxwell's
equations in isotropic media. *Antennas and Propagation, IEEE Transactions on* **14**, 302-
307 (1966).
- 54 Sonnichsen, C. *et al.* Drastic Reduction of Plasmon Damping in Gold Nanorods. *Phys.*
Rev. Lett. **88**, 077402 (2002).
- 55 Mühlischlegel, P., Eisler, H.-J., Martin, O.J.F., Hecht, B., & Pohl, D.W. Resonant Optical
Antennas. *Science* **308**, 1607-1609 (2005).
- 56 Slovick, B.A., Krenz, P.M., Zummo, G., & Boreman, G.D. Evaporation of uniform
antireflection coatings on hemispherical lenses to enhance infrared antenna gain.
Infrared Physics & Technology **53**, 89-93 (2011).
- 57 Fumeaux, C. *et al.* Measurement of the resonant lengths of infrared dipole antennas.
Infrared Physics & Technology **41**, 271-281 (2000).
- 58 Bean, J.A., Weeks, A., & Boreman, G. Performance Optimization of Antenna-Coupled
Al/AlO_x/Pt Tunnel Diode Infrared Detectors *IEEE J. Quantum Electron.* **47**, 126-135
(2011).
- 59 Yang, W. *et al.* The IR antenna pair coupled sensor element and its potential application
in wavefront sensing. *Infrared Physics & Technology* **51**, 495-504 (2008).
- 60 Ghenuche, P., Cherukulappurath, S., Taminiu, T.H., Van Hulst, N.F., & Quidant, R.
Spectroscopic Mode Mapping of Resonant Plasmon Nanoantennas. *Phys. Rev. Lett.* **101**,
116805 (2008).
- 61 Gersten, J. & Nitzan, A. Electromagnetic theory of enhanced Raman scattering by
molecules adsorbed on rough surfaces. *J. Chem. Phys.* **73**, 3023-3037 (1980).

62 Zuloaga, J. & Nordlander, P. On the Energy Shift between Near-Field and Far-Field
Peak Intensities in Localized Plasmon Systems. *Nano Lett.* **11**, 1280-1283 (2011).

63 Chen, J. *et al.* Plasmonic Nickel Nanoantennas. *Small* **7**, 2341-2347 (2011).

64 Ross, B.M. & Lee, L.P. Comparison of near- and far-field measures for plasmon
resonance of metallic nanoparticles. *Opt. Lett.* **34**, 896-898 (2009).

65 Knight, M.W., Wu, Y., Lassiter, J.B., Nordlander, P., & Halas, N.J. Substrates Matter:
Influence of an Adjacent Dielectric on an Individual Plasmonic Nanoparticle. *Nano Lett.*
9, 2188-2192 (2009).

66 Tam, F., Moran, C., & Halas, N. Geometrical Parameters Controlling Sensitivity of
Nanoshell Plasmon Resonances to Changes in Dielectric Environment. *The Journal of*
Physical Chemistry B **108**, 17290-17294 (2004).

67 Mock, J.J., Smith, D.R., & Schultz, S. Local Refractive Index Dependence of Plasmon
Resonance Spectra from Individual Nanoparticles. *Nano Lett.* **3**, 485-491 (2003).

68 Halas, N.J., Lal, S., Chang, W.-S., Link, S., & Nordlander, P. Plasmons in Strongly
Coupled Metallic Nanostructures. *Chem. Rev.* **111**, 3913-3961 (2011).

69 Schuck, P.J., Fromm, D.P., Sundaramurthy, A., Kino, G.S., & Moerner, W.E. Improving
the mismatch between light and nanoscale objects with gold bowtie nanoantennas. *Phys.*
Rev. Lett. **94**, 017402 (2005).

70 Grober, R.-D., Schoellkopf, R.-J., & Prober, D.-E. Optical antenna: Towards a unity
efficient near-field optical probe. *Appl. Phys. Lett.* **70**, 1354-1356 (1997).

71 Kim, S. *et al.* High-harmonic generation by resonant plasmon field enhancement. *Nature*
453, 757-760 (2008).

72 Yu, N. *et al.* Plasmonic quantum cascade laser antenna. *Appl. Phys. Lett.* **91**, 173113
(2007).

73 Alu, A. & Engheta, N. Input Impedance, Nanocircuit Loading, and Radiation Tuning of
Optical Nanoantennas. *Phys. Rev. Lett.* **101**, 043901 (2008).

74 Straw, R.D., Andress, K., Cebik, L.B., Severns, R., & Witt, F., *The ARRL Antenna Book*,
19 ed. (The American Radio League, Inc., Newington, CT, 2000).

75 Goubau, G. Surface Waves and Their Application to Transmission Lines. *J. Appl. Phys.*
21, 1119-1128 (1950).

76 Engheta, N., Salandrino, A., & Alu, A. Circuit elements at optical frequencies:
Nanoinductors, nanocapacitors, and nanoresistors. *Phys. Rev. Lett.* **95**, 095504 (2005).

77 Engheta, N. Circuits with Light at Nanoscales: Optical Nanocircuits Inspired by
Metamaterials. *Science* **317**, 1698-1702 (2007).

78 Alu, A. & Engheta, N. Wireless at the Nanoscale: Optical Interconnects using Matched
Nanoantennas. *Phys. Rev. Lett.* **104**, 213902 (2010).

79 Esteban, R. *et al.* Direct Near-Field Optical Imaging of Higher Order Plasmonic
Resonances. *Nano Lett.* **8**, 3155-3159 (2008).

80 Stockmann, M.I., Faleev, S.V., & Bergmann, D.J. Coherent control of femtosecond
energy localization in nanosystems. *Phys. Rev. Lett.* **88**, 67402 (2002).

81 Volpe, G., Cherukulappurath, S., Juanola Parramon, R., Molina-Terriza, G., & Quidant,
R. Controlling the Optical Near Field of Nanoantennas with Spatial Phase-Shaped
Beams. *Nano Lett.* **9**, 3608-3611 (2009).

82 Bouhelier, A. *et al.* Surface Plasmon Characteristics of Tunable Photoluminescence in
Single Gold Nanorods. *Phys. Rev. Lett.* **95**, 267405 (2005).

83 Hohenau, A. *et al.* Spectroscopy and nonlinear microscopy of Au nanoparticle arrays:
Experiment and theory. *Phys. Rev. B* **73**, 155404 (2006).

84 Ghenuche, P., Cormack, I.G., Badenes, G., Loza-Alvarez, P., & Quidant, R. Cavity
85 resonances in finite plasmonic chains. *Appl. Phys. Lett.* **90**, 041109 (2007).
86 ten Bloemendal, D. *et al.* Local Field Spectroscopy of Metal Dimers by TPL
87 Microscopy. *Plasmonics* **1**, 41-44 (2006).
88 Nelayah, J. *et al.* Mapping surface plasmons on a single metallic nanoparticle. *Nat Phys*
89 **3**, 348-353 (2007).
90 Aeschlimann, M. *et al.* Adaptive subwavelength control of nano-optical fields. *Nature*
91 **446**, 301-304 (2007).
92 Schmidt, O. *et al.* Time-resolved two photon photoemission electron microscopy.
93 *Applied Physics B: Lasers and Optics* **74**, 223-227 (2002).
94 Swiech, W. *et al.* Recent progress in photoemission microscopy with emphasis on
95 chemical and magnetic sensitivity. *J. Electron. Spectrosc. Relat. Phenom.* **84**, 171-188
96 (1997).
97 Cinchetti, M. *et al.* Photoemission Electron Microscopy as a Tool for the Investigation of
98 Optical Near Fields. *Phys. Rev. Lett.* **95**, 047601 (2005).
99 Guiton, B.S. *et al.* Correlated Optical Measurements and Plasmon Mapping of Silver
100 Nanorods. *Nano Lett.* **11**, 3482-3488 (2011).
101 Nelayah, J. *et al.* Two-Dimensional Quasistatic Stationary Short Range Surface
102 Plasmons in Flat Nanoprisms. *Nano Lett.* **10**, 902-907 (2010).
103 Garcia de Abajo, F.J. & Kociak, M. Probing the Photonic Local Density of States with
104 Electron Energy Loss Spectroscopy. *Phys. Rev. Lett.* **100**, 106804 (2008).
Rossouw, D., Couillard, M., Vickery, J., Kumacheva, E., & Botton, G.A. Multipolar
Plasmonic Resonances in Silver Nanowire Antennas Imaged with a Subnanometer
Electron Probe. *Nano Lett.* **11**, 1499-1504 (2011).
Chu, M.-W. *et al.* Probing Bright and Dark Surface-Plasmon Modes in Individual and
Coupled Noble Metal Nanoparticles Using an Electron Beam. *Nano Lett.* **9**, 399-404
(2008).
Koh, A.L., Fernandez-Dominguez, A.I., McComb, D.W., Maier, S.A., & Yang, J.K.W.
High-Resolution Mapping of Electron-Beam-Excited Plasmon Modes in
Lithographically Defined Gold Nanostructures. *Nano Lett.* **11**, 1323-1330 (2011).
Krenn, J.R. *et al.* Direct Observation of localized surface plasmon coupling. *Phys. Rev. B*
60, 5029-5033 (1999).
Krenn, J.R. *et al.* Squeezing the Optical Near-Field Zone by Plasmon Coupling of
Metallic Nanoparticles. *Phys. Rev. Lett.* **82**, 2590-2593 (1999).
Krenn, J.R., Gotschy, W., Somitsch, D., Leitner, A., & Aussenegg, F.R. Investigation of
localized surface plasmons with the photon scanning tunneling microscope. *Applied*
Physics A: Materials Science & Processing **61**, 541-545 (1995).
Kawata, S., in *Near-Field Optics and Surface Plasmon Polaritons* (Springer Berlin /
Heidelberg, 2001), Vol. 81, pp. 15-27.
Reddick, R., Warmack, R., & Ferrell, T. New form of scanning optical microscope.
Phys. Rev. B **39**, 767-770 (1989).
Pohl, D.W., Denk, S., & Lanz, M. Optical stethoscopy: Image recording with resolution
 $\lambda / 20$. *Appl. Phys. Lett.* **44**, 651-653 (1984).
Betzig, E., Isaacson, M., & Lewis, A. Collection mode near-field scanning optical
microscopy. *Appl. Phys. Lett.* **51**, 2088-2090 (1987).
Betzig, E., Trautmann, J.K., Harris, T.D., Weiner, J.S., & Kostelak, R.L. Breaking the
diffraction barrier: Optical microscopy on a nanometric scale. *Science* **251**, 1468-1470
(1991).

- 105 Flück, E., van Hulst, N.F., Vos, W.L., & Kuipers, L. Near-field optical investigation of
three-dimensional photonic crystals. *Phys. Rev. E* **68**, 015601 (2003).
- 106 Sandtke, M. *et al.* Novel instrument for surface plasmon polariton tracking in space and
time. *Rev. Sci. Instrum.* **79**, 013704 (2008).
- 107 Balistreri, M.L.M., Korterik, J.P., Kuipers, L., & van Hulst, N.F. Local Observations of
Phase Singularities in Optical Fields in Waveguide Structures. *Phys. Rev. Lett.* **85**, 294
(2000).
- 108 Hillenbrand, R. & Keilmann, F. Optical oscillation modes of plasmon particles observed
in direct space by phase-contrast near-field microscopy. *Appl. Phys. B* **73**, 239-243
(2001).
- 109 Schnell, M. *et al.* Controlling the near-field oscillations of loaded plasmonic
nanoantennas. *Nature Photon.* **3**, 287-291 (2009).
- 110 Schnell, M. *et al.* Amplitude- and Phase-Resolved Near-Field Mapping of Infrared
Antenna Modes by Transmission-Mode Scattering-Type Near-Field Microscopy. *The
Journal of Physical Chemistry C* **114**, 7341-7345 (2010).
- 111 Kim, D.-S. *et al.* Real-Space Mapping of the Strongly Coupled Plasmons of Nanoparticle
Dimers. *Nano Lett.* **9**, 3619-3625 (2009).
- 112 Hillenbrand, R., Keilmann, F., Hanarp, P., Sutherland, D.S., & Aizpurua, J. Coherent
imaging of nanoscale plasmon patterns with a carbon nanotube optical probe. *Appl.
Phys. Lett.* **83**, 368-370 (2003).
- 113 Kim, Z.H. & Leone, S.R. Polarization-selective mapping of near-field intensity and
phase around gold nanoparticles using apertureless near-field microscopy. *Opt. Express*
16, 1733-1741 (2008).
- 114 Kim, D.S. & Kim, Z.H. Polarization-Selective Imaging of the Enhanced Local Field at
Gold Nanoparticle Junctions. *J. Korean Phys. Soc.* **52**, 17-20 (2007).
- 115 Rang, M. *et al.* Optical Near-Field Mapping of Plasmonic Nanoprisms. *Nano Lett.* **8**,
3357-3363 (2008).
- 116 Burrelli, M. *et al.* Probing the Magnetic Field of Light at Optical Frequencies. *Science*
326, 550-553 (2009).
- 117 Olmon, R.L., Krenz, P.M., Jones, A.C., Boreman, G.D., & Raschke, M.B. Near-field
imaging of optical antenna modes in the mid-infrared. *Opt. Express* **16**, 20295-20305
(2008).
- 118 Balistreri, M.L.M. *et al.* Visualizing the whispering gallery modes in a cylindrical optical
microcavity. *Opt. Lett.* **24**, 1829-1831 (1999).
- 119 Krenn, J.R. & Weeber, J.C. Surface Plasmon polaritons in metal stripes and wires.
Philos. Trans. R. Soc. London, Ser. A **362**, 739-756 (2004).
- 120 Smolyaninov, I.I., Atia, W., & Davis, C.C. Near-field optical microscopy of two-
dimensional photonic and plasmonic crystals. *Phys. Rev. B* **59**, 2454 (1999).
- 121 Weeber, J.C. *et al.* Near-field observation of surface plasmon polariton propagation on
thin metal stripes. *Phys. Rev. B* **64**, 045411 (2001).
- 122 Weeber, J.-C., Lacroute, Y., & Dereux, A. Optical near-field distributions of surface
plasmon waveguide modes. *Phys. Rev. B* **68**, 115401 (2003).
- 123 Zia, R., Schuller, J.A., Chandran, A., & Brongersma, M.L. Plasmonics: the next chip-
scale technology. *Mater. Today* **9**, 20-27 (2006).
- 124 Offerhaus, H.L. *et al.* Creating Focused Plasmons by Noncollinear Phasematching on
Functional Gratings. *Nano Lett.* **5**, 2144-2148 (2005).
- 125 Knoll, B. & Keilmann, F. Electromagnetic fields in the cutoff regime of tapered metallic
waveguides. *Optics Communications* **162**, 177-181 (1999).

- 126 Garcia-Etxarri, A., Romero, I., García de Abajo, F.J., Hillenbrand, R., & Aizpurua, J. Influence of the tip in near-field imaging of nanoparticle plasmonic modes: Weak and strong coupling regimes. *Physical Review B (Condensed Matter and Materials Physics)* **79**, 125439 (2009).
- 127 Hillenbrand, R., Knoll, B., & Keilmann, F. Pure optical contrast in scattering-type scanning near-field optical microscopy. *Journal of Microscopy* **202**, 77-83 (2001).
- 128 Yu, N.F. *et al.* Bowtie plasmonic quantum cascade laser antenna. *Opt. Express* **15**, 13272-13281 (2007).
- 129 Meyer, E., Hug, H.J., & Bennewitz, R., *Scanning Probe Microscopy*. (Springer, 2004).
- 130 Ocelic, N., Huber, A., & Hillenbrand, R. Pseudoheterodyne detection for background-free near-field spectroscopy. *Appl. Phys. Lett.* **89**, 101124 (2006).
- 131 Ocelic, N., *Quantitative near-field phonon-polariton spectroscopy*. (Verein zur Förderung des Walter Schottky Instituts der Technischen Universität München, München, 2007).
- 132 Hillenbrand, R. & Keilmann, F. Material-specific mapping of metal/semiconductor/dielectric nanosystems at 10 nm resolution by back-scattering near-field optical microscopy. *Appl. Phys. Lett.* **80**, 25 (2002).
- 133 Hillenbrand, R. & Keilmann, F. Complex optical constants on a subwavelength scale. *Phys. Rev. Lett.* **85**, 3029-3032 (2000).
- 134 Deutsch, B., Hillenbrand, R., & Novotny, L. Near-field amplitude and phase recovery using phase-shifting interferometry. *Opt. Express* **16**, 494-501 (2008).
- 135 Deutsch, B., Hillenbrand, R., & Novotny, L. Visualizing the Optical Interaction Tensor of a Gold Nanoparticle Pair. *Nano Lett.* **10**, 652-656 (2010).
- 136 Xu, H., Aizpurua, J., Käll, M., & Apell, P. Electromagnetic contributions to single-molecule sensitivity in surface-enhanced Raman scattering. *Phys. Rev. E* **62**, 4318-4324 (2000).
- 137 Rechberger, W. *et al.* Optical properties of two interacting gold nanoparticles. *Optics Communications* **220**, 137-141 (2003).
- 138 Romero, I., Aizpurua, J., Bryant, G.W., & de Abajo, F.J.G. Plasmons in nearly touching metallic nanoparticles: singular response in the limit of touching dimers. *Opt. Express* **14**, 9988-9999 (2006).
- 139 Atay, T., Song, J.H., & Nurmikko, A.V. Strongly interacting plasmon nanoparticle pairs: From dipole-dipole interaction to conductively coupled regime. *Nano Lett.* **4**, 1627-1631 (2004).
- 140 Lassiter, J.B. *et al.* Close encounters between two nanoshells. *Nano Lett.* **8**, 1212-1218 (2008).
- 141 Nordlander, P., Oubre, C., Prodan, E., Li, K., & Stockman, M.I. Plasmon Hybridization in Nanoparticle Dimers. *Nano Lett.* **4**, 899-903 (2004).
- 142 Lee, K.G. *et al.* On the concept of imaging nanoscale vector fields. *Nature Photon.* **1**, 243-244 (2007).
- 143 Gersen, H., Novotny, L., Kuipers, L., & van Hulst, N.F. On the concept of imaging nanoscale vector fields. *Nat Photon* **1**, 242-242 (2007).
- 144 Born, M. & Wolf, E., *Principles of optics*. (Cambridge University Press, Cambridge, 1999).
- 145 Biagioni, P., Huang, J.S., Duò, L., Finazzi, M., & Hecht, B. Cross Resonant Optical Antenna. *Phys. Rev. Lett.* **102**, 256801 (2009).
- 146 Lounis, B. & Orrit, M. Single-photon sources. *Rep. Prog. Phys.* **68**, 1129 (2005).

- 147 Qiu, Z.Q. & Bader, S.D. Surface magneto-optic Kerr effect (SMOKE). *J. Magn. Magn. Mater.* **200**, 664-678 (1999).
- 148 Stanciu, C.D. *et al.* All-Optical Magnetic Recording with Circularly Polarized Light. *Phys. Rev. Lett.* **99**, 047601 (2007).
- 149 Lee, K.G. *et al.* Vector field microscopic imaging of light. *Nat Photon* **1**, 53-56 (2007).
- 150 Guo, H. *et al.* Optical resonances of bowtie slot antennas and their geometry and material dependence. *Opt. Express* **16**, 7756-7766 (2008).
- 151 Zentgraf, T. *et al.* Babinet's principle for optical frequency metamaterials and nanoantennas. *Phys. Rev. B* **76**, 033407 (2007).
- 152 Schnell, M. *et al.* Nanofocusing of mid-infrared energy with tapered transmission lines. *Nat Photon* **5**, 283-287 (2011).
- 153 Shalaev, V.M. Optical negative-index metamaterials. *Nature Photon.* **1**, 41-48 (2007).
- 154 Gutberlet, A. *et al.* Aggregation-Induced Dissociation of HCl(H₂O)₄ Below 1 K: The Smallest Droplet of Acid. *Science* **324**, 1545-1548 (2009).
- 155 Li, Z.Q. *et al.* Dirac charge dynamics in graphene by infrared spectroscopy. *Nature Phys.* **4**, 532-535 (2008).
- 156 Soref, R. Mid-infrared photonics in silicon and germanium. *Nature Photon.* **4**, 495-497 (2010).
- 157 Schnell, M., Garcia-Etxarri, A., Alkorta, J., Aizpurua, J., & Hillenbrand, R. Phase-Resolved Mapping of the Near-Field Vector and Polarization State in Nanoscale Antenna Gaps. *Nano Lett.* **10**, 3524-3528 (2010).
- 158 Olmon, R.L. *et al.* Determination of Electric-Field, Magnetic-Field, and Electric-Current Distributions of Infrared Optical Antennas: A Near-Field Optical Vector Network Analyzer. *Phys. Rev. Lett.* **105**, 167403 (2010).
- 159 Bharadwaj, P., Deutsch, B., & Novotny, L. Optical Antennas. *Adv. Opt. Photon.* **1**, 438-483 (2009).
- 160 Schuller, J.A. *et al.* Plasmonics for extreme light concentration and manipulation. *Nature Mater.* **9**, 193-204 (2010).
- 161 Soukoulis, C.M., Linden, S., & Wegener, M. Negative Refractive Index at Optical Wavelengths. *Science* **315**, 47-49 (2007).
- 162 Novotny, L. & Hafner, C. Light propagation in a cylindrical waveguide with a complex, metallic, dielectric function. *Phys. Rev. E* **50**, 4094-4106 (1994).
- 163 Keilmann, F. Surface-polariton propagation for scanning near-field optical microscopy application. *Journal of Microscopy* **194**, 567-570 (1999).
- 164 Stockman, M.I. Nanofocusing of optical energy in tapered plasmonic waveguides. *Phys. Rev. Lett.* **93**, 137404 (2004).
- 165 Verhagen, E., Spasenovicacute, M., Polman, A., & Kuipers, L. Nanowire Plasmon Excitation by Adiabatic Mode Transformation. *Phys. Rev. Lett.* **102**, 203904 (2009).
- 166 De Angelis, F. *et al.* Nanoscale chemical mapping using three-dimensional adiabatic compression of surface plasmon polaritons. *Nature Nanotech.* **5**, 67-72 (2010).
- 167 Ropers, C. *et al.* Grating-Coupling of Surface Plasmons onto Metallic Tips: A Nanoconfined Light Source. *Nano Lett.* **7**, 2784-2788 (2007).
- 168 Pile, D.F.P. & Gramotnev, D.K. Adiabatic and nonadiabatic nanofocusing of plasmons by tapered gap plasmon waveguides. *Appl. Phys. Lett.* **89**, 041111 (2006).
- 169 Choi, H., Pile, D.F., Nam, S., Bartal, G., & Zhang, X. Compressing surface plasmons for nano-scale optical focusing. *Opt. Express* **17**, 7519-7524 (2009).
- 170 Vedantam, S. *et al.* A Plasmonic Dimple Lens for Nanoscale Focusing of Light. *Nano Lett.* **9**, 3447-3452 (2009).

- 171 Verhagen, E., Kuipers, L., & Polman, A. Enhanced Nonlinear Optical Effects with a
Tapered Plasmonic Waveguide. *Nano Lett.* **7**, 334-337 (2006).
- 172 Neacsu, C.C. *et al.* Near-Field Localization in Plasmonic Superfocusing: A Nanoemitter
on a Tip. *Nano Lett.* **10**, 592-596 (2010).
- 173 Wang, K. & Mittleman, D.M. Metal wires for terahertz wave guiding. *Nature* **432**, 376-
379 (2004).
- 174 Pendry, J.B., Martin-Moreno, L., & Garcia-Vidal, F.J. Mimicking surface plasmons with
structured surfaces. *Science* **305**, 847-848 (2004).
- 175 Maier, S.A., Andrews, S.R., Martin-Moreno, L., & Garcia-Vidal, F.J. Terahertz Surface
Plasmon-Polariton Propagation and Focusing on Periodically Corrugated Metal Wires.
Phys. Rev. Lett. **97**, 176805 (2006).
- 176 Rusina, A., Durach, M., Nelson, K.A., & Stockman, M.I. Nanoconcentration of terahertz
radiation in plasmonic waveguides. *Opt. Express* **16**, 18576-18589 (2008).
- 177 Akalin, T., Treizebre, A., & Bocquet, B. Single-wire transmission lines at terahertz
frequencies. *IEEE T. Microw. Theory* **54**, 2762-2767 (2006).
- 178 Zhan, H., Mendis, R., & Mittleman, D.M. Superfocusing terahertz waves below
 $\lambda/250$ using plasmonic parallel-plate waveguides. *Opt. Express* **18**, 9643-9650
(2010).
- 179 Mandviwala, T., Lail, B., & Boreman, G. Infrared-frequency coplanar striplines: Design,
fabrication, and measurements. *Microw. Opt. Techn. Let.* **47**, 17-20 (2005).
- 180 Krenz, P.M., Olmon, R.L., Lail, B.A., Raschke, M.B., & Boreman, G.D. Near-field
measurement of infrared coplanar strip transmission line attenuation and propagation
constants. *Opt. Express* **18**, 21678-21686 (2010).